Journal of Materials Chemistry A

ROYAL SOCIETY OF CHEMISTRY

REVIEW

View Article Online
View Journal | View Issue

Cite this: J. Mater. Chem. A, 2021, 9, 5320

Recent advances in transition-metal-sulfide-based bifunctional electrocatalysts for overall water splitting

Min Wang,[a] Li Zhang,[b] Yijia He[c] and Hongwei Zhu *[a]

Hydrogen produced *via* water electrolysis can act as an ideal clean chemical fuel with superb gravimetric energy density and high energy conversion efficiency, solving the problems of conventional fossil fuel exhaustion and environmental contamination. Transition metal sulfides (TMS) have been extensively explored as effective, widely available alternatives to precious metals in overall water splitting. Herein, recent advances, covering preparation methods, intrinsic electrocatalytic performance, and optimization strategies, relating to TMS-based bifunctional electrocatalysts have been summarized systematically and comprehensively. Firstly, a general introduction to the reaction mechanisms and key parameters of the hydrogen evolution reaction (HER) and oxygen evolution reaction (OER) is provided. Next, the physicochemical properties of TMS and typical synthesis methods are introduced to give guidance for fabricating TMS materials with well-defined structures, controllable compositions, and excellent performance. Importantly, the intrinsic activities of TMS-based electrocatalysts and several strategies for improving their bifunctional electrocatalytic performance during water electrolysis are discussed in detail. Finally, perspectives covering the challenges and opportunities related to the further development of TMS-based materials with high activity and long-term durability for overall water splitting are given. The aim herein is to provide guidelines for the design and fabrication of TMS-based bifunctional electrocatalysts with excellent performance and to accelerate their large-scale practical application in water electrolysis.

Received 15th December 2020
Accepted 20th January 2021

DOI: 10.1039/d0ta12152e

rsc.li/materials-a

[a]State Key Lab of New Ceramics and Fine Processing, School of Materials Science and Engineering, Tsinghua University, Beijing 100084, China. E-mail: hongweizhu@tsinghua.edu.cn

[b]Key Laboratory of Photochemical Conversion and Optoelectronic Materials, Technical Institute of Physics and Chemistry, Chinese Academy of Sciences, Beijing 100190, China

[c]China Ship Information Center, Beijing 100192, China

1. Introduction

1.1 Background

The growing consumption of conventional fossil fuels and accompanying environmental contamination are affecting global society on an unprecedented scale.[1] Consequently, there

Min Wang is a PhD candidate at the School of Materials Science and Engineering, Tsinghua University, China. She received her B.S. degree in Materials Science and Engineering from Jilin University in 2016. Her research focuses on advanced nanomaterials related to electrocatalysis for energy conversion.

Hongwei Zhu is a Professor at the School of Materials Science and Engineering, Tsinghua University, China. He received his B.S. degree in Mechanical Engineering (1998) and his PhD degree in Materials Processing Engineering (2003) from Tsinghua University. After post-doctoral studies in Japan and the USA, he began his independent career as a faculty member at Tsinghua University (2008 to present). His current research interests involve low-dimensional materials and materials informatics.

is a quite imminent need to fundamentally adjust the world energy landscape and build clean, low-carbon, safe, and efficient modern energy systems. As an ideal clean chemical fuel with superb gravimetric energy density and energy conversion efficiency, hydrogen energy is expected to be an excellent candidate to replace traditional fossil fuels.[2] Electrochemical water splitting is considered to be one of the most promising hydrogen production technologies, and it can utilize electricity generated *via* renewable energy sources, such as solar energy, wind power, geothermal energy, and bioenergy, to form a closed loop of renewable energy.[3] Unfortunately, the large-scale commercial application of electrochemical water splitting is subject to the following three restrictions: (i) a larger overpotential than the theoretical value (1.23 V) being needed to drive overall water splitting; (ii) the poor stability of electrode materials; and (iii) high cost caused by the scarcity of noble-metal electrocatalysts.[4,5] To date, the benchmark electrocatalysts for the hydrogen evolution reaction (HER) and oxygen evolution reaction (OER) are Pt-group- and Ru/Ir-based noble metal materials with small overpotentials and low Tafel slopes.[6] These noble metals can suffer from dissolution, agglomeration, and poor durability during the water splitting process.[7]

The development of low-cost and widely available alternatives with more excellent activities and stabilities than precious metals is urgently needed for overall water splitting, and this is a crucial step in the development of a hydrogen-based economy. There are three main kinds of electrolyzer used for water electrolysis, categorized by the electrolyte: alkaline electrolyzers (AEs), acidic proton exchange membrane (PEM) electrolyzers, and solid oxide electrolyzers (SOEs).[8] SOEs are still in the laboratory stage, and they are operated at high temperatures (700–800 °C) to reduce the overpotential. Alkaline electrolyzers have the advantages of simple construction, convenient operation, and low cost. In comparison, water electrolysis carried out in acidic electrolyte involves fewer adverse reactions and higher ionic conductivity, but it demands expensive perfluorinated Nafion-based PEMs.[9] As we know, neutral and alkaline electrolytes are favorable for the OER, while acidic electrolytes are beneficial for the HER. Inevitably, this non-negligible mismatch between optimal working environments for the HER and OER has a negative impact on the overall efficiency of water electrolysis systems.[10] In this regard, designing and constructing effective bifunctional electrocatalysts that can be employed for both the HER and OER in the same electrolyte is another vital issue related to commercial electrochemical water splitting.

A variety of Earth-abundant and non-precious transition metal (*e.g.*, Mo, W, Ni, Co, and Fe) based compounds have been explored as bifunctional electrocatalysts for overall water splitting, such as transition metal sulfides, phosphides, nitrides, carbides, oxides, and hydroxides.[3,10–14] Specifically, transition-metal sulfides (TMS) with distinctive structural features, rich active sites, and adjustable electronic properties and components have attracted widespread research attention,[2] *e.g.*, layered MoS_2 and WS_2 and non-layered Ni_3S_2 and Co_3S_4. There are multitudinous excellent reviews on research achievements relating to TMS-based electrocatalysts, however, most of them have an emphasis on either one or a limited number of TMS systems for electrochemical water splitting, such as transition-metal dichalcogenides for the HER,[15,16] Fe-based electrocatalysts for the OER,[17] or Co-based electrocatalysts for overall water splitting.[18] Moreover, the use of nanoarchitectonics in TMS-based electrocatalysts to improve their performance for water splitting[19] and recent advances relating to metal sulfides, from their controlled fabrication to their applications in electrocatalytic, photocatalytic, and photoelectrochemical water splitting, have also been reviewed.[2] However, a targeted review focusing on TMS-based bifunctional electrocatalysts addressing their controllable preparation, intrinsic electrocatalytic activities, and optimization strategies for enhancing their electrocatalytic performance in overall water splitting has not been fully provided to date.

Herein, we focus on recent developments relating to TMS-based bifunctional electrocatalysts, with respect to synthetic methods, intrinsic electrocatalytic activities, and corresponding optimization strategies, aiming to provide a comprehensive overview of the basic information and breakthroughs relating to the use of TMS for electrochemical water splitting. Firstly, the reaction mechanisms for the HER and OER processes together

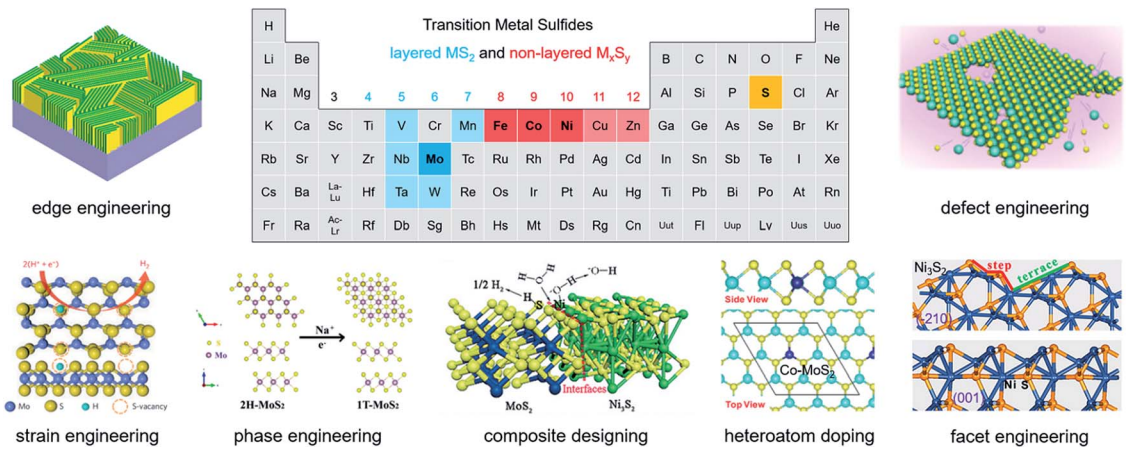

Fig. 1 Possible suitable elements and strategies for improving the electrocatalytic performances of TMS-based bifunctional electrocatalysts; transition metals with deeper colors in the periodic table have been the focus of more studies.

with some significant parameters for evaluating the properties of bifunctional electrocatalysts are introduced. Secondly, the physicochemical properties of TMS and the role of S atoms in electrochemical water splitting are emphatically discussed. Then, typical synthetic methods for TMS are discussed, which exhibit great influence on the electrocatalytic performance. Importantly, the intrinsic activities of TMS-based bifunctional electrocatalysts and several strategies aimed at the optimization of the electrocatalytic performance in overall water splitting are summarized systematically. Possible suitable elements and strategies for improving the electrocatalytic performance of TMS-based bifunctional electrocatalysts are displayed in Fig. 1. Meanwhile, the opportunities and challenges relating to the development of TMS bifunctional electrocatalysts are discussed and an outlook shedding light on directions for further research into TMS is also put forward.

1.2 Fundamentals of overall water splitting

1.2.1 Reaction mechanisms. Electrochemical water splitting involves two half reactions, namely the HER and OER. The electrolyzer typically consists of three parts: a cathode, an anode, and the aqueous electrolyte, and a schematic diagram is shown in Fig. 2a. When a certain voltage is applied to the two electrodes, the water reduction reaction occurs at the cathode to produce H_2 and the water oxidation reaction happens at the anode to produce O_2. The total reaction can be written as follows:

$$2H_2O \rightarrow 2H_2 + O_2 \quad (1)$$

The theoretical thermodynamic potential of overall water splitting is 1.23 V under ideal conditions (25 °C and 1 atm). However, a higher operational potential (E) is always necessary to actually carry out the process. The excess potential is named the overpotential (η), which is mainly used to overcome intrinsic activation hindrance at both the anode (η_a) and cathode (η_c), as well as other inevitable obstacles (η_{other}) due to the electrolyte and contact resistance. Overall:

$$E = 1.23\ \text{V} + \eta_a + \eta_c + \eta_{other} \quad (2)$$

The HER is a two-electron transfer process that happens at the cathode; it is always more active in acidic electrolytes than in alkaline electrolytes because the reduction of protons to H_2 is energetically more favorable.[20] There are two mechanisms involved the HER, namely the Volmer–Heyrovsky and Volmer–Tafel pathways (Fig. 2b), depending on the way in which adsorbed hydrogen is desorbed from the electrocatalyst.[21] In acidic electrolytes, hydronium ions adsorb on the cathode to form hydrogen intermediates (H*) *via* the Volmer reaction ($H_3O^+ + e^- \rightarrow H^* + H_2O$) and then transform into H_2 *via* the Heyrovsky reaction ($H^* + H_3O^+ + e^- \rightarrow H_2 + H_2O$) at low H* coverage or *via* the Tafel reaction ($H^* + H^* \rightarrow H_2$) at high H* coverage. Under alkaline conditions, the HER is more sluggish due to the water dissociation step prior to the formation of H*.[22] A water molecule undergoes a dissociation reaction to generate absorbed H* *via* the Volmer reaction ($H_2O + e^- \rightarrow H^* + OH^-$). The desorption process is carried out *via* the Heyrovsky or Tafel reaction, similar to under acidic conditions.

In the HER process, the free energy of hydrogen adsorption (ΔG_H) calculated *via* density functional theory (DFT) is widely accepted as a descriptor for the interactions between absorbed H* and the electrocatalyst.[23] A large negative ΔG_H value indicates that the adsorption of hydrogen on the electrode is much easier than desorption, so the Heyrovsky or Tafel reaction is the rate-limiting step. Otherwise, a large positive ΔG_H value represents a weak interaction, and the rate-limiting step is the Volmer reaction. Thus, an excellent HER electrocatalyst should possess near-zero ΔG_H, with a balance between the absorption and desorption of hydrogen.

The OER is more sluggish than the HER, and it naturally requires a larger overpotential because it involves a complex four-proton transfer process.[19] Possible mechanisms for the OER at the anode have been proposed, including almost the same intermediates, such as MO and MOH (M: transitional metal, such as Fe, Co, and Ni).[24] The general reaction pathways and widely accepted mechanisms for the OER in alkaline and acidic electrolytes are shown in Fig. 2c. There are two possible pathways for MO intermediates to convert to O_2: combining H_2O under acidic conditions or OH^- under alkaline conditions with an MO intermediate to form an MOOH intermediate, which then transforms into O_2; and directly uniting two MO

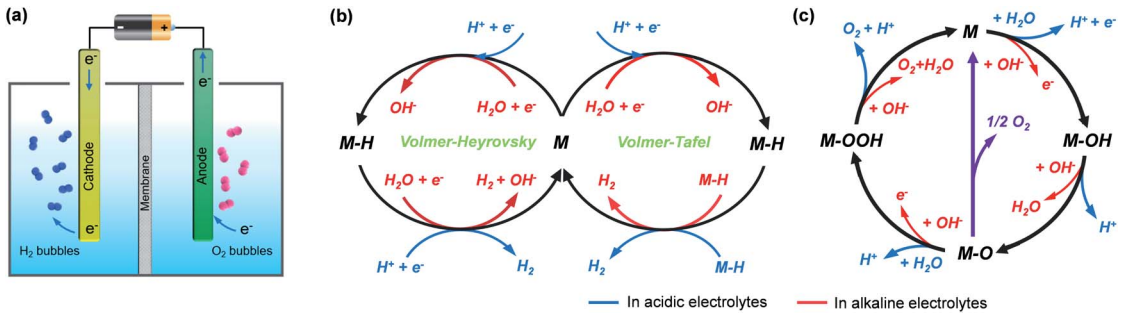

Fig. 2 (a) A schematic illustration of electrochemical water splitting. (b) The general reaction pathways for the HER in alkaline (red lines) and acidic (blue lines) electrolytes. (c) The general reaction pathways for the OER in alkaline (red lines) and acidic (blue lines) electrolytes; the black and purple lines stand for two possible intermediates: M–OOH and M–O, respectively.

intermediates to generate O_2. Therefore, the M–O bonds of MOH, MO, and MOOH intermediates play key roles in determining the electrocatalytic OER activity.[25] Since the reactions in the OER are all thermodynamically uphill, the reaction with the highest energy barrier will be the rate-determining step.[19] The OER rate-determining step can also be determined based on the Tafel slope, and the actual reaction mechanism can be understood further. For example, the Tafel slope is about 120 mV dec^{-1} when the first reaction (from M to MOH) is the rate-determining step, while the Tafel slope is about 40 mV dec^{-1} if the second reaction (from MOH to MO) acts as the rate-determining step.

The thermodynamics in each OER step can be studied *via* DFT calculations. Rossmeisl *et al.* studied four reactions during the OER and obtained the corresponding Gibbs free energies ($\Delta G_i = \Delta G_{product} - \Delta G_{reactant} - eU - k_B T \ln[H^+]$, $i = 1$–4) under an applied potential (U), where k_B is the Boltzmann constant and T is the temperature.[26] The largest Gibbs free energy of these is defined as ΔG^{OER} for the OER.[3] Under standard conditions ($U_{SHE} = 0$), the relationship between the theoretical overpotential (η^{OER}) and ΔG^{OER} is as follows:

$$\eta^{OER} = (\Delta G^{OER}/e) - 1.23\ V \quad (3)$$

The ideal value of ΔG^{OER} is 1.23 eV when $\eta^{OER} = 0$, indicating that the Gibbs free energy in each step is 1.23 eV. However, there is always a gap between ideality and reality due to unsuitable electrocatalyst oxygen bonding forces that can make the OER more sluggish.

1.2.2 Parameters for electrochemical water splitting. There are some important electrochemical water splitting parameters that can be used to evaluate the electrocatalytic performances of materials, such as the overpotential, Tafel slope, exchange current density, turnover frequency, stability, faradaic efficiency, and electrochemically active surface area.

Overpotential (η) is the excess part of the operational potential beyond the equilibrium potential that arises due to an unavoidable intrinsic kinetic barrier.[27] As mentioned above, the equilibrium potentials for electrocatalyzing the HER and OER are 0 V and 1.23 V (*vs.* RHE: reversible hydrogen electrode), respectively. However, applied potentials much higher than the equilibrium potentials are needed to overcome the electrode kinetic barriers in the reaction. Normally, the total activity of an electrocatalyst can be assessed based on polarization curves (after IR compensation) using the geometric current density and overpotential, which are obtained from cyclic voltammetry (CV) or linear sweep voltammetry (LSV) measurements. It is worth noting that different current densities can refer to different overpotential values. Thus, the overpotential at a certain current density (like 10 or 100 mA cm^{-2}) obtained from a polarization curve is one of the most popular descriptors of the total activity.[28] The smaller the overpotential at a certain current density, the better the electrochemical activity of the electrocatalyst.

Tafel slope is a key kinetic parameter in electrochemical water splitting, implying how fast the current density increases with increasing overpotential.[29] A Tafel plot can be obtained *via* transforming the current density from a polarization curve into a logarithmic value with base 10 on the x axis, with the corresponding overpotential on the y axis. In a Tafel plot, there is a linear region that can be well-fitted using the Tafel equation:

$$\eta = a + b \log j \quad (4)$$

where b stands for the Tafel slope, η is the overpotential, j represents the current density, and a is a constant. A smaller Tafel slope always signifies faster charge-transfer kinetics; in other words, increasing the current density leads to a smaller overpotential increase than in a case with a larger Tafel slope. Hence, the Tafel slope can be employed to deduce the possible reaction mechanism, and especially to explain the rate-determining step. When the value of η is equal to zero, the corresponding current density (j) is the exchange current density (j_0) that can reflect the intrinsic bonding/charge transfer interactions between the electrocatalyst and reactant. A high j_0 value is always a good indication of superior inherent electrocatalyst activity under equilibrium conditions. In short, materials with a small η and a larger j_0 value will be efficacious electrocatalysts.

Turnover frequency (TOF) denotes the number of molecules transformed at each active site per unit time, signifying the intrinsic activity of each active site. The TOF can be calculated *via* the following equation:

$$TOF = (jA)/(\alpha Fn) \quad (5)$$

where j represents the current density at a certain overpotential obtained from the LSV curve; A is the surface area of the electrode; α denotes the electron number of the electrocatalyst (electrons mol^{-1}); F is the Faraday constant (96 485.3 C mol^{-1}); and n stands for the molar amount of electrocatalyst. The precise TOF value is difficult to obtain, as it is not possible to accurately determine the number of all accessible active sites involved in the actual reaction. As such, a reasonable approach for calculating the TOF is based merely on either the number of atoms on the surface or the number of easily accessible electrocatalytic sites of the material. Sometimes, the TOF is calculated based on the overall catalytic species existing in the material.[11] Despite the imprecision of TOF values, they still play a meaningful role in evaluating the intrinsic catalytic activities of electrocatalysts with similar elements and structures.

Stability is a considerably important parameter for electrocatalysts for practical applications, reflecting the ability of an electrocatalyst to maintain its activity under long-term testing (generally several or tens of hours). In general, there are two electrochemical techniques used to measure the electrocatalytic stability. One is performing CV measurements for thousands of cycles, followed by LSV measurements; the stability can be examined *via* comparing the LSV curves before and after the cycling CV testing. The other way is to conduct chronoamperometry or chronopotentiometry measurements to show how the potential or current density varies with time; a high retention rate corresponds to good stability. Usually, a current density of 10 mA cm^{-2} is applied as a standard for

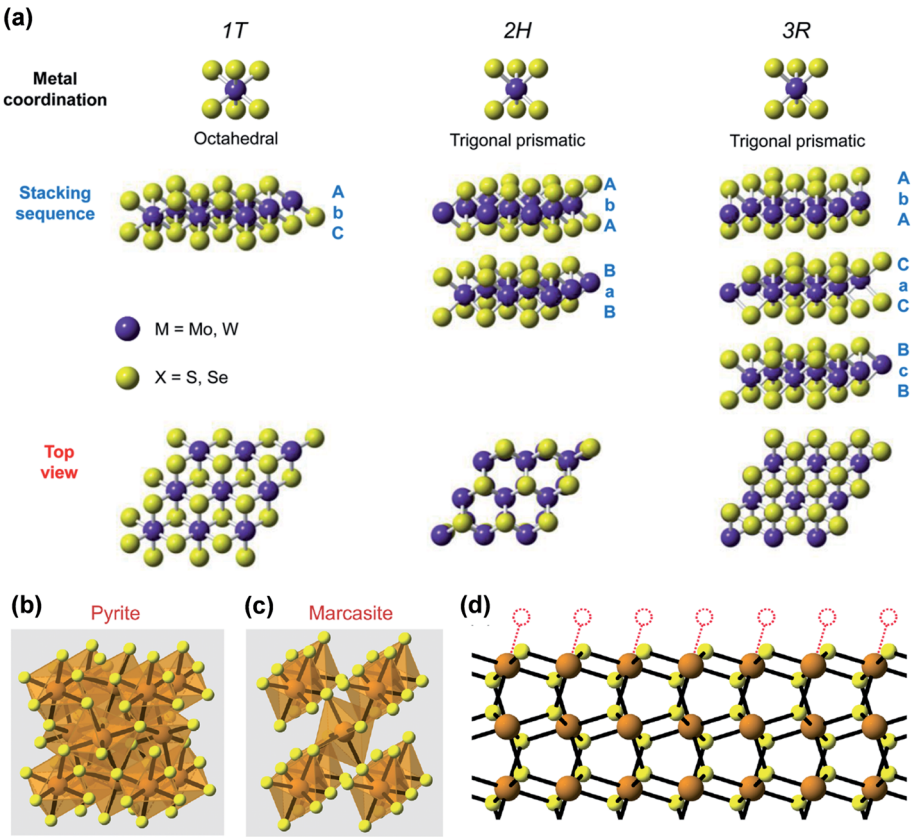

Fig. 3 (a) The different metal coordination modes and stacking sequences of layered TMS structural unit cells. The metal can have either octahedral coordination or trigonal prismatic coordination. Octahedral coordination allows stacking sequences with tetragonal symmetry, like AbC, AbC, *etc.*; trigonal prismatic layers can be stacked in two different ways to form hexagonal symmetry (2H) or rhombohedral symmetry (3R).[34] (b and c) The structures of non-layered TMS in pyrite and marcasite phases, in which transition metal atoms and S atoms are shown in orange and yellow, respectively. (d) A side-view of the stable nonpolar pyrite (100) facet as an example of a low-index surface with under-coordinated transition metal cations.[38]

evaluating the electrocatalytic stability. To illustrate the potential of an electrocatalyst for use in practical applications, stability at a large current density (*e.g.*, 500 mA cm^{-2}) is absolutely needed.

Faradaic efficiency is defined as the efficiency of electron transfer when catalyzing a desired reaction in the electrochemical system, which is quantified as the experimental to theoretical molar ratio of the numbers of gas molecules. The experimental produced gas can be measured *via* the traditional water gas displacement method or gas chromatography, while the theoretical value can be calculated *via* chronoamperometry or chronopotentiometry measurements. A higher faradaic efficiency means less energy loss during the electrochemical reaction.

Electrochemically active surface area (ECSA) is universally utilized to estimate the effective active surface of the working electrode, which is based on the electrochemical double-layer capacitance of the electrocatalytic surface.[30] The electrochemical double-layer capacitance can be measured based on the capacitive current associated with double-layer charging in a non-faradaic region from the scan-rate dependence of CV curves.[31] Typically, the non-faradaic region is a potential window of 0.1 V centered at the open-circuit potential of the system. A plot of the charging current as a function of the scan rate yields a straight line with a slope equal to the electrochemical double-layer capacitance (C_{DL}). The ECSA of an electrocatalyst sample is calculated *via* the following equation:

$$\mathrm{ECSA} = \frac{C_{DL}}{C_s} \quad (6)$$

where C_s is the specific capacitance of the electrocatalyst or the capacitance per unit area of an atomically smooth planar surface of the material, with typical values between 0.015 and 0.110 mF cm^{-2} in H_2SO_4 and 0.022 and 0.130 mF cm^{-2} in NaOH or KOH solution.[30] In addition, the electrochemical capacitance can also be acquired from the frequency-dependent impedance based on electrochemical impedance spectroscopy (EIS) studies in the same non-faradaic region.

2. Physicochemical properties of TMS

2.1 Structures and basic properties

Based on crystal structures, TMS can be mainly divided into two categories: layered MS_2 and non-layered M_xS_y. The sulfides of transition-metals in groups 4–7 (M = Mo, W, Ta, Nb, *etc.*) always

crystallize with a graphite-like layered structure, whereas some sulfides of transition-metals in groups 8–12 (M = Fe, Co, Ni, *etc.*) predominantly adopt non-layered structures. Distinctions between the structures and compositions of these TMS will inevitably bring about differences in their electronic and electrochemical properties.

Typically, each layer of layered MS_2 has a thickness of 0.6–0.7 nm, consisting of a hexagonal layer of transition-metal atoms sandwiched between two layers of sulfur (S) atoms.[32] These layers, with strong intra-layer covalent bonds between atoms, will be stacked vertically together *via* relatively weak out-of-plane *van der Waals* forces. Consequently, layered MS_2 can be exfoliated readily into two-dimensional nanosheets.[33] Depending on the transition-metal coordination of S atoms and the stacking sequence adopted by multiple layers, layered MS_2 can be classified into different phases: 1T, 2H, and 3R, where the digit denotes the number of stacked layers in the crystallographic unit cell and the letter stands for tetragonal, hexagonal, and trigonal lattices, respectively, as shown in Fig. 3a.[34] In layered MS_2, the transition-metal atoms centered in an octahedral configuration or trigonal prismatic configuration will provide four electrons to fill the bonding states of TMS, so the transition-metal atom is in a +4 oxidation state and the S atom is in a −2 state.

The electronic properties of TMS are extremely dependent on the filling of the d orbitals of the transition metal. For example, the semiconductor behavior of natural 2H-MoS_2 can mainly be ascribed to the fully filled d orbitals of the Mo atom, so 2H-MoS_2 is expected to be employed in electronic devices. However, 1T-MoS_2, with partially filled Mo atom d orbitals exhibits metallic properties, which will be more suitable for electrocatalysis.[35] Interestingly, an MS_2 phase transition from 2H to 1T, such as in the cases of MoS_2 and WS_2, could be realized *via* the intercalation of alkali metals, which introduce extra electrons and rearrange the d orbitals of metals.[36,37]

Furthermore, the electrochemical properties of layered TMS also strongly depend on their structures and compositions. The unique stacked structures of layered TMS bring about two distinctive orientations: the basal plane and edge plane, which exhibit anisotropic properties in many aspects. Firstly, the in-plane electrical conductivity of layered MS_2 is about 2200 times higher than the interlayer conductivity.[34] As a consequence, heterogeneous electron transfer along the edge plane of layered TMS is significantly faster than along its basal plane. As such, the electrochemical activity in the edge plane and basal plane of layered TMS is also predicted to be anisotropic. Typically, sites on the basal planes of group-6 TMS are always inert, while the highly active edge sites mainly contribute to the excellent electrocatalytic performance.[39] Taking well-studied MoS_2 as an example, 2H-MoS_2 exhibits hydrogen adsorption free energy of +0.08 eV on its edge sites compared with 2.00 eV on its inert basal plane.[40] Intensive efforts have been made to induce basal plane electrochemical activity. Zheng *et al.* activated and optimized the basal plane of monolayer 2H-MoS_2 for the HER *via* introducing S vacancies and elastic strain.[41] S vacancies could serve as new active sites in the basal plane, as the gap states around the Fermi level would permit hydrogen to bind with exposed Mo atoms directly. What is more, the electrochemical activity of 2H-MoS_2 could be optimized further *via* straining the plane with S-vacancy sites.

In addition, chemical doping with non-metallic or metallic elements is widely considered to be an effective approach for creating active sites in the inert basal plane of MoS_2 and for increasing the intrinsic electrical conductivity; *e.g.*, oxygen (O),[42] nitrogen (N), phosphorus (P),[43] selenium (Se),[44] and zinc (Zn)[45] elements can be used. Additionally, these dopants can also greatly optimize the hydrogen adsorption free energy, accelerate charge transfer, and, finally, enhance the electrocatalytic performance of MoS_2. It is worth mentioning that group-5 TMS can possess active basal-plane sites intrinsically, *e.g.*, in the cases of TaS_2 and NbS_2. Yakobson *et al.* proposed that active sites were concentrated in the basal planes and at the edges of H-TaS_2 simultaneously according to experimental and theoretical results, and the active basal-plane sites could contribute to self-optimizing behavior during the HER.[46]

Non-layered M_xS_y (M = Fe, Co, Ni, *etc.*) generally shares a pyrite structure or marcasite structure when $x = 1$ and $y = 2$, and the conventional unit cells with high similarity are shown in Fig. 3b and c.[38] The pyrite structure belongs to the space group $Pa\bar{3}$, in which the transition-metal atoms are located at face-centered cubic (FCC) sites and bonded octahedrally to adjacent S atoms. Each S atom in the pyrite structure is tetrahedrally coordinated to three transition-metal atoms and one S atom, such that an S_2 dimer will also be formed.[47] The marcasite structure adopts the orthorhombic *Pnnm* space group, where the body-centered transition-metal atoms are also octahedrally bonded to neighboring S atoms. It can be clearly found that the octahedra in the marcasite structure are edge-sharing, while in the pyrite structure they are corner-sharing. Indeed, the intergrowth or epitaxial growth of the marcasite structure in/on the pyrite structure of non-layered M_xS_y can achieved readily due to their structural similarities. Moreover, the electronic structures of pyrite-type non-layered M_xS_y, which predominantly depend on the d-electron count of the transition metal, are diverse, ranging from insulators (such as NiS_2) to semiconductors (such as FeS_2) to metals (such as CoS_2).[48] Interestingly, the values of x and y for each particular M_xS_y structure can be diverse and a series of sulfides can be formed, *e.g.*, NiS, NiS_2, Ni_3S_2, Ni_3S_4, Ni_7S_6, and Ni_9S_8.[49] Typically, the composition of non-layered M_xS_y can also have a great influence on the electronic properties. In nickel sulfides, NiS_2 is an insulator while heazlewoodite Ni_3S_2 shows intrinsic metallic behavior owing to the continuous conductive network, connected *via* Ni–Ni bonds, in its crystal structure.[50]

Differences in the crystal structures and compositions of layered MS_2 and non-layered M_xS_y result in discrepant electronic and electrochemical properties. However, the main strategies for improving the electrocatalytic performance are comprehensive, and they involve enhancing the intrinsic activity of each active site, increasing the number of active sites, and improving the electrical conductivity.[1,51] Edge engineering and defect engineering have been developed to expose or create more active sites, and strain engineering, facet engineering, heteroatom doping, and composite designing have been

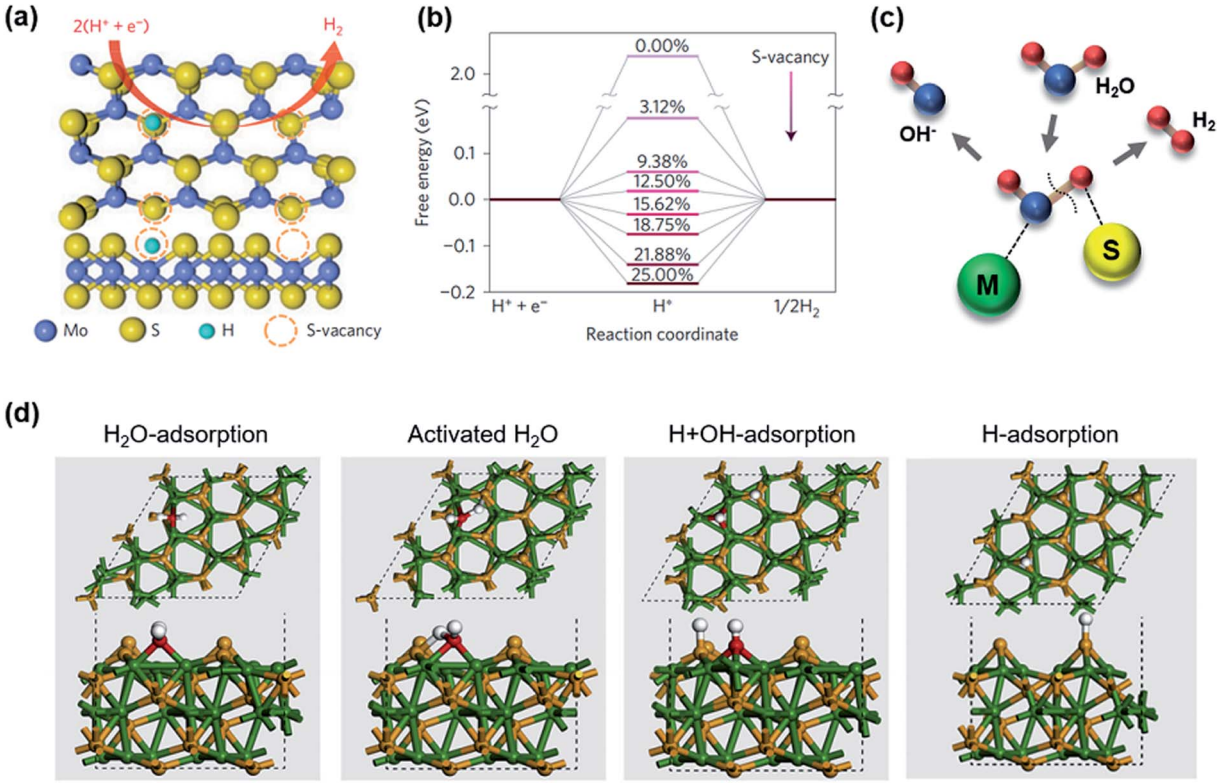

Fig. 4 (a) Schematic illustrations showing top and side views of MoS_2 with S vacancies on the basal plane. (b) A plot of calculated free energy *versus* the reaction coordinate of MoS_2 during the HER over an S vacancy range of 0–25%.[41] (c) A schematic diagram of the HER reaction mechanism of TMS when metal atoms act as the active sites. (d) The obtained structures of H_2O, activated H_2O, OH, and H intermediates during water dissociation and H adsorbed on the Ni_3S_2 (003) surface after relaxation.[50]

explored to accelerate electron transportation in these electrocatalysts during water splitting. Details of these optimization approaches for electrocatalytic performance will be discussed below.

2.2 The role of S atoms in the HER and OER

Revealing the true active sites or species is crucial for developing new electrocatalysts aimed at efficient overall water splitting. Although the main active sites in TMS are always metal atoms, understanding the role of S atoms in TMS is still an important task. Basically speaking, S atoms in TMS can contribute to special structures and abundant species, such as in the 2D layered structures of MS_2 (M: transition metal in group 4–7), and in the nickel sulfides Ni_3S_2, NiS_2, and Ni_3S_4. The roles of S atoms in catalyzing the HER and OER can be divided into two types: a direct role and an indirect role, depending on the contribution of S atoms to the electrocatalytic performance.

In the HER, some exposed S atoms and S vacancies on the edges or on the basal plane of TMS can have a great effect on the electrocatalytic performance; this can be thought of as an embodiment of the direct role of S atoms. Based on experimental and theoretical results, Jaramillo *et al.* identified that the active sites of MoS_2 during the HER could be S atoms on the edges under low H coverage (1/4 ML).[52] What is more, S vacancies on the basal plane of layered 2H-MoS_2 could contribute to enhanced HER activity,[41] which is a powerful method for improving the HER performance (Fig. 4a). On one hand, S vacancies can change the coordination environment of adjacent metal atoms: metal atoms with low coordination will be more active and will possess higher intrinsic electrocatalytic activity. On the other hand, S vacancies can induce more active sites and significantly increase the number of active sites. Therefore, S vacancies can create new active sites on the inert basal plane of 2H-MoS_2, where gap states around the Fermi level can allow hydrogen binding directly with exposed Mo sites. Furthermore, ΔG_H can be finely manipulated *via* changing the number of S vacancies (Fig. 4b).

The indirect role of S atoms in the HER mainly arises through providing a place for hydrogen adhesion and separation when metal atoms act as the active sites (Fig. 4c). When the HER took place on Ni_3S_2 nanoporous thin films with exposed (003) facets, Dong *et al.* came to the following conclusions based on theoretical calculations: H_2O was preferentially adsorbed on Ni sites *via* the Volmer process, and S sites were more suitable for the formation of H_2 in the Tafel stage (Fig. 4d).[50] More straightforward evidences for the indirect role of S atoms has been found in experiments by Staszak-Jirkovsky *et al.*[4] They proposed that TM^{n+} (Co^{2+}/Mo^{4+}) plays a key role in accelerating the sluggish water dissociation process in alkaline solutions, while the recombination of absorbed hydrogen could happen at S sites. Due to the amorphous phases of the catalysts, they

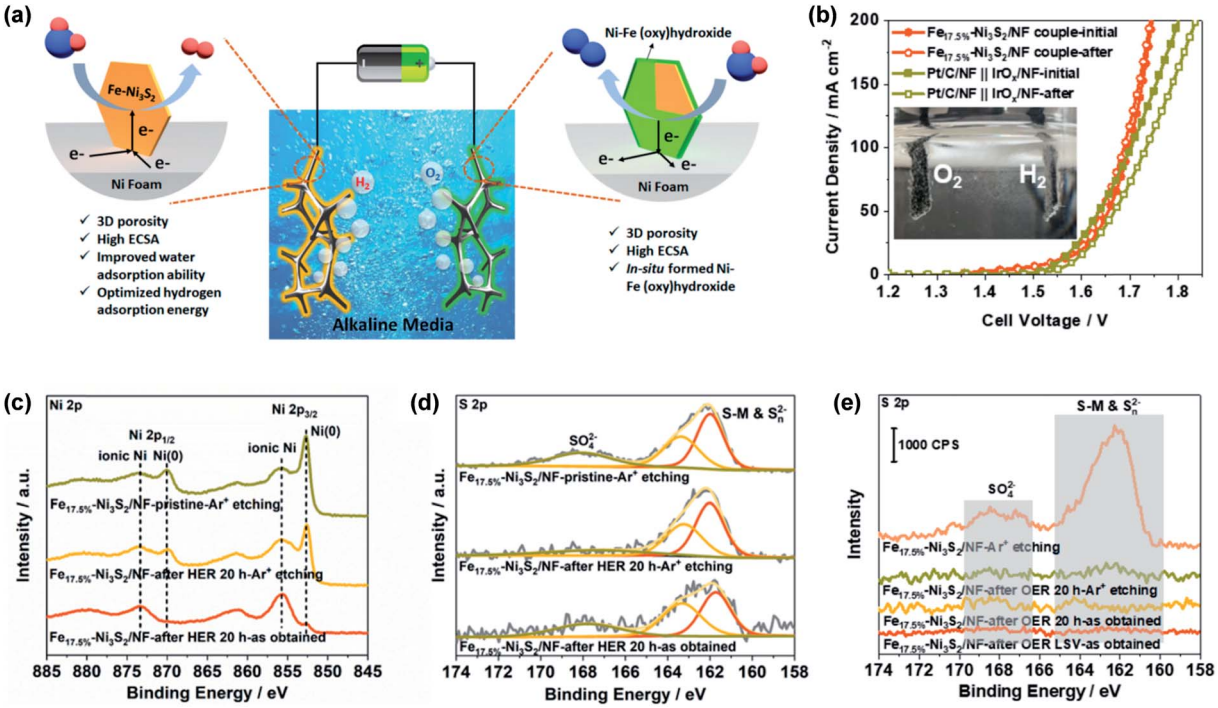

Fig. 5 (a) A schematic diagram of Fe-Ni_3S_2/NF applied to overall water splitting in a two-electrode configuration. (b) The polarization curves of an $Fe_{17.5\%}$-Ni_3S_2/NF couple and Pt/C/NF//IrO_x/NF water electrolyzers in alkaline solution at 5 mV s^{-1}. (c) Ni 2p and (d) S 2p high-resolution XPS spectra of $Fe_{17.5\%}$-Ni_3S_2/NF before and after long-term HER testing. (e) S 2p high-resolution XPS spectra of $Fe_{17.5\%}$-Ni_3S_2/NF before and after long-term OER testing. Ar^+ etching was employed to remove surface materials.[8]

further mimicked $S^{\delta-}$–TM^{n+} building blocks in chalcogels *via* a simple model based on $S^{\delta-}$–C^{n+}–H_2O clusters to verify the indirect promotion of S sites, where C^{n+} represents K^+/Ba^{2+} cations. In this case, S sites were proved to be enhancers of the HER activity of metal sites in alkaline solutions.

The OER is more complex than the HER, involving the formation of many intermediates during the reaction, such as –OH and –OOH intermediates. Subbaraman *et al.* proposed that the increasing OER activities of 3d-M hydr(oxy)oxides (M = Fe, Co, Ni, or Mn) are closely connected with the decreased bond strength of OH_{ad}–M^{n+}, which was mainly ascribed to enhanced repulsion between the metal d-band and coordinated oxygen p-band centers.[53] As we know, electronegative S atoms in TMS would hinder the coordination of –OH with metal atoms due to repulsion between the S 3p orbital and O 2p orbital. However, this 3p–2p repulsion could accelerate the further oxidation of –OOH intermediates, and the formation of –OOH intermediates could also be promoted by the delocalized electrons of S atoms.[3]

There also have been numerous efforts to reveal the true role of the S atoms of TMS in the OER. As a general rule, TMS tend to function as pre-catalysts in the OER because of the conversion of sulfides to transition metal hydr(oxy)oxides during the OER process.[54] Zhang *et al.* confirmed that Ni-Fe (oxy)hydroxides that formed in the near-surface region of Fe-doped Ni_3S_2 on Ni foam (Fe-Ni_3S_2/NF) are the real active materials that actually contribute to the OER activity.[8] In this case, the bifunctional Fe-Ni_3S_2/NF electrode could act both as a catalyst for the HER and also as a pre-catalyst for the *in situ* formation of active-oxidation-state species for electrocatalyzing the OER, which was verified based on high-resolution XPS spectra before and after long-term testing (Fig. 5). No obvious changes appeared in the component types and binding energies of both Ni and S elements, indicating that Fe-Ni_3S_2/NF possesses superior durability in terms of structure and composition during the HER process. Nevertheless, high-resolution S 2p XPS spectra revealed that the signal intensity of S on the surface was obviously reduced after OER testing and even after further Ar^+ etching, suggesting that near-surface sulfides had been transformed to Ni-Fe (oxy)hydroxides in the OER process.

Coincidentally, Mabayoje *et al.* discovered that NiS can transform into amorphous NiO_x during the OER, which was derived from the finding that S anions in NiS were completely depleted in the active form of the electrocatalyst.[55] In the Ni 3p XPS region, they speculated that the number of oxidation states of Ni in amorphous NiO_x induced by Ni vacancies are higher than in crystalline NiO. Furthermore, amorphous NiO_x derived from NiS had a relatively high electrochemically active surface area and exhibited enhanced OER activity. Thus, TMS can serve as pre-catalysts to produce more active transition metal hydr(oxy)oxides for electrocatalyzing the OER.

In conclusion, when TMS are employed as electrocatalysts, the main active sites are always metal atoms, while S atoms play pivotal roles in determining the catalytic activity. In the OER process, S atoms can promote the formation of more active transition metal hydr(oxy)oxides. In the HER process, exposed S atoms can act as active sites under specific conditions,

providing places for hydrogen adhesion and separation when metal atoms are the active sites, while S vacancies can induce more active sites and change the coordination environments of adjacent metal atoms, enhancing the activity. A clear understanding of the roles of the S atoms/vacancies of TMS in water splitting could bring enlightenment for designing novel electrocatalysts. Nevertheless, more systematic research revealing the exact roles of these atoms in actual reactions should be conducted, and it could greatly accelerate the development of TMS for water electrolysis.

3. Typical synthetic methods for TMS

The controllable synthesis of TMS with well-defined shapes, sizes, hierarchical structures, and defect states is the initial step in obtaining high-performance bifunctional electrocatalysts. Up to now, various methods have been developed for preparing high-quality TMS, which can be divided into two types, 'bottom-up' and 'top-down' strategies.[2] A schematic illustration of typical synthetic methods for TMS materials is shown in Fig. 6.

3.1 'Top-down' strategies

Typically, top-down strategies refer to the exfoliation or successive reduction of a bulk starting material to target nanostructures, such as *via* ball milling and sputtering methods. In particular, exfoliation is a simple, low-cost, and promising technique for fabricating high-quality, layered low-dimensional TMS materials; mechanical exfoliation and liquid phase exfoliation are common methods.[56]

Mechanical exfoliation is a clean and easy way to gain pristine TMS of high-quality that are suitable for fundamental studies and potential applications based on the intrinsic thickness-dependent properties of TMS. Typically, bulk TMS materials with layered structures are applied as starting materials, and TMS parts are peeled off using adhesive tape ('sticky' tape) and then transferred onto the target surface.[2] The TMS parts attach to the surface *via van der Waals* forces. Li *et al.* produced single-layer and multilayer MoS_2 nanosheets *via* mechanical exfoliation.[57] However, some challenges still remain in relation to mechanical exfoliation due to the following points: the bulk starting crystals are expensive; a transfer process is essential for further applications; and the as-exfoliated TMS flakes always have random shapes and low yields.

Liquid phase exfoliation is an efficient method for exfoliating TMS in solution; the yields are considerably higher than those obtained *via* mechanical exfoliation, while the product is of lower quality. There are two approaches for exfoliating TMS in the liquid phase. The first one is exfoliation *via* a mechanical method, such as shearing, sonication, stirring, grinding, or bubbling. Exfoliation mechanisms are mainly based on external force induced *via* mechanical effects and interactions with solvent molecules.[58] Coleman *et al.* reported that layered compounds such as MoS_2 and WS_2 could be easily exfoliated into individual layers *via* sonication exfoliation in solution (Fig. 7a and b).[59] This procedure was insensitive to water and air and could be potentially scaled up to obtain large quantities of exfoliated products. Additionally, hybrid dispersions or composites could be made for further film-forming *via* blending these materials with suspensions of other nanomaterials or polymer solutions. Later, Varrla *et al.* proposed the large-scale shear-exfoliation of MoS_2 nanosheets in aqueous surfactant solutions using a kitchen blender (Fig. 7c and d).[60] *Via* optimizing the processing parameters, such as the MoS_2 concentration, mixing time, liquid volume, and rotor speed, high concentrations (0.4 mg mL^{-1}) and high production rates (1.3

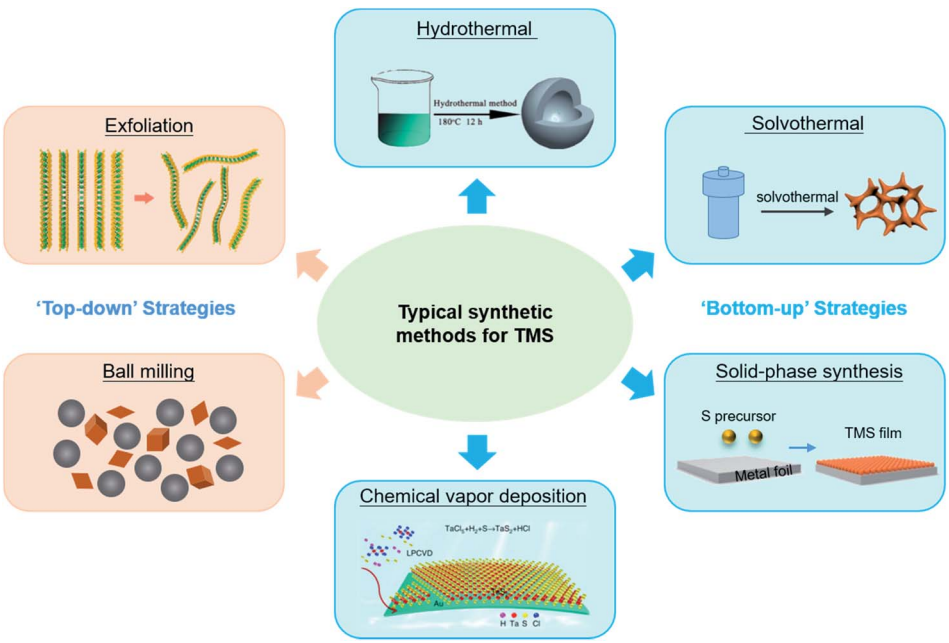

Fig. 6 A schematic illustration of typical synthetic methods for TMS materials.

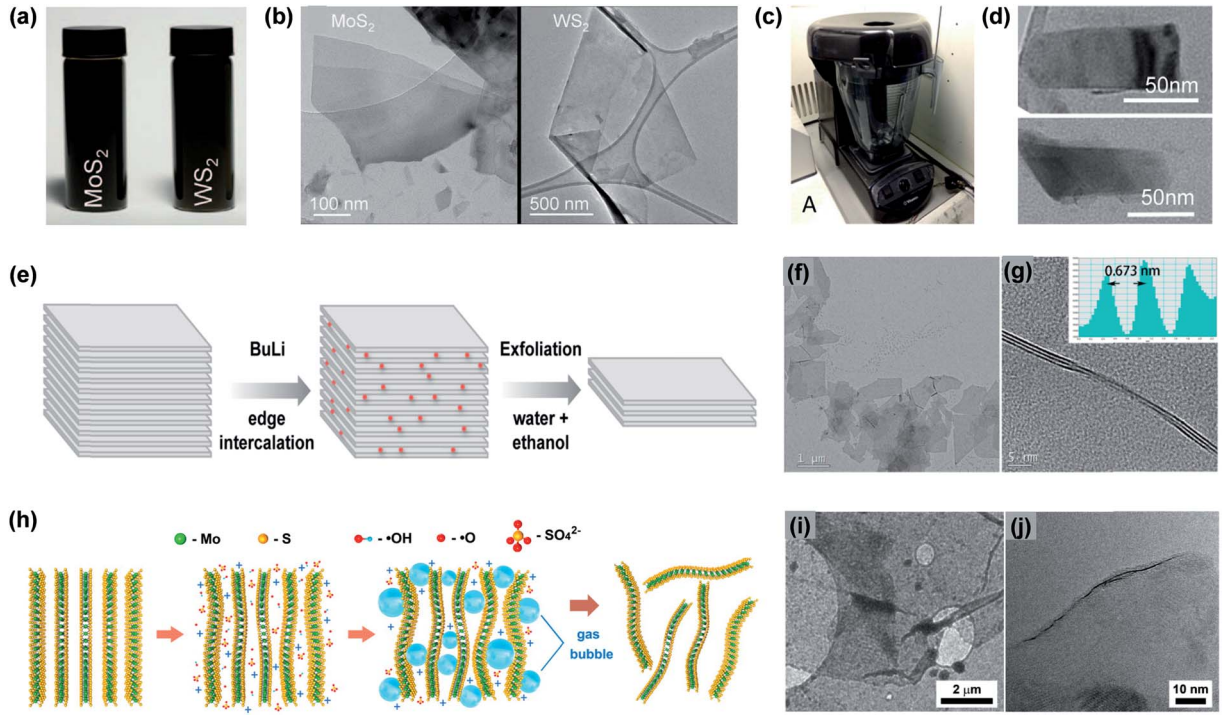

Fig. 7 (a) Photographs of dispersions of MoS_2 and WS_2 in NMP. (b) TEM images of MoS_2 and WS_2 flakes produced *via* sonication exfoliation.[59] (c) A photograph of a kitchen blender. (d) TEM images of typical MoS_2 flakes produced *via* shearing exfoliation.[60] (e) A schematic diagram of the preparation of trilayer MoS_2 nanosheets *via* chemical intercalation. (f and g) TEM images of the exfoliated MoS_2 nanosheets produced *via* chemical intercalation.[62] (h) A schematic illustration of the mechanism of MoS_2-flake formation *via* electrochemical intercalation. (i and j) TEM and HRTEM images of exfoliated MoS_2 flakes produced *via* electrochemical intercalation.[63]

mg min^{-1}) could be achieved. In addition, the surfactant concentration not only influenced the nanosheet concentration but it also had great effects on the nanosheet lateral size and thickness, with higher surfactant concentrations giving smaller flake sizes. In this regard, the average MoS_2 nanosheet dimensions could be controlled during shear exfoliation, at least in the ranges of about 40–220 nm for length and about 2–12 layers for thickness.

As reported, the surfactant plays a key role in liquid-phase exfoliation, and it could greatly influence the dimensions of the products. Zhao *et al.* prepared WS_2 nanodots with high quality and uniformity that were dispersed in aqueous solution *via* liquid-phase exfoliation from bulk crystals with the aid of ultrasonication in surfactant aqueous solution.[61] The size distributions of WS_2 nanodots showed that the lateral sizes were 2.7 ± 0.8 nm and the height was 0.7 nm, which was about the size of a single layer. Remarkably, a high concentration of 1T-WS_2 existed in the as-prepared WS_2 nanodots, which could be responsible for its enhanced electrocatalytic activity.

The second liquid-phase exfoliation route involves ionic intercalation, where lithium ions are typically intercalated between the TMS layers to reduce *van der Waals* forces between layers *via* enlarging the interlayer spacing.[64] Ionic intercalation is beneficial for subsequent exfoliation, and it can involve chemical intercalation and electrochemical intercalation. Fan *et al.* developed an chemical intercalation method *via* the incorporation of sub-stoichiometric amounts of *n*-butyllithium (BuLi) to controllably exfoliate MoS_2 crystals into trilayer nanosheets (Fig. 7e–g).[62] The intercalated lithium at the edges of the MoS_2 crystals could serve as a wedge to promote the exfoliation of MoS_2 *via* solvent molecules with a yield of 11–15 wt% exfoliated nanosheets in ethanol/water mixtures. The exfoliation efficiency of a pre-intercalated sample was notably increased by at least 1 order of magnitude compared with the starting MoS_2 microcrystals. However, some shortcomings related to chemical intercalation are inevitable, like extreme sensitivity to ambient conditions and the small lateral size of the chemically exfoliated nanosheets. Liu *et al.* prepared large-area atomically thin MoS_2 nanosheets *via* the electrochemical exfoliation of a bulk MoS_2 crystal (Fig. 7h–j).[63] Firstly, ·OH, ·O radicals, and/or SO_4^{2-} anions were inserted into the MoS_2 layers under a positive bias applied at the working electrode, weakening the *van der Waals* interactions between layers. Then, the oxidation of these radicals and/or anions could lead to the release of O_2 and/or SO_2 gas, which could cause the great expansion of the MoS_2 interlayers. Finally, atomically thin MoS_2 flakes were detached from the bulk MoS_2 crystal by the erupting gas and then suspended in solution.

Ball milling is a low-cost and easy scalable mechano-chemical route for preparing TMS nanostructures. In the ball-milling process, powder particles undergo severe mechanical deformation due to collisions with stainless-steel balls and the vessel; they then become continually deformed, cold-welded, and fractured. Concurrently, mechano-chemical reactions

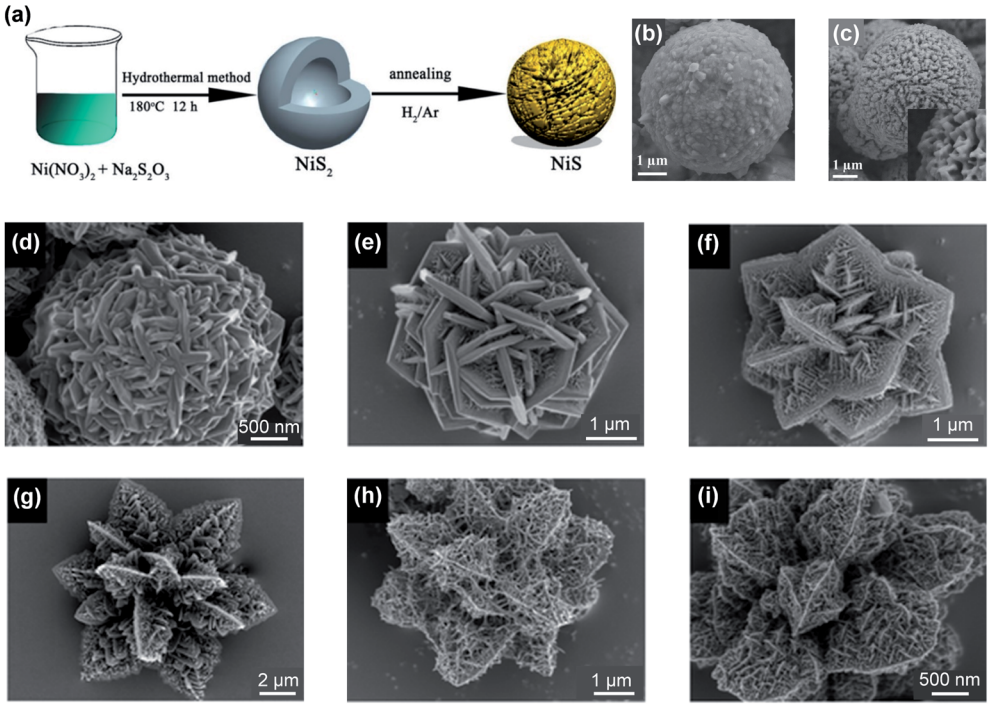

Fig. 8 (a) A schematic diagram of the hydrothermal synthesis of NiS_2 and NiS porous hollow microspheres. (b) An SEM image of NiS_2 hollow microspheres. (c) An SEM image of NiS porous hollow microspheres.[67] (d–i) FESEM images of CoS synthesized at 160 °C for given reaction times of 2 h, 5 h, 12 h, 24 h, 36 h, and 48 h, respectively.[68]

and/or solid-state reactions can happen in powder blends. The ball-milling time is a key parameter, and an inert gas atmosphere is usually used to protect the TMS powder from oxidation. Homogeneous NiS powders were prepared by ball milling of several mixed phases, such as Ni_3S_2, Ni_7S_6, Ni_xS_6, and Ni_3S_4, up to 12 h under an Ar atmosphere.[65] Similarly, Ambrosi *et al.* fabricated a MoS_2 electrocatalyst *via* ball milling bulk natural MoS_2, and the size reduction contributed to the enhanced electrocatalytic performance.[66]

3.2 'Bottom-up' strategies

Proverbially, bottom-up strategies refer to the build-up of nanomaterials atom by atom, molecule by molecule, or cluster by cluster, for example *via* hydrothermal method, solvothermal method, chemical vapor deposition, electrochemical deposition, atomic layer deposition, thermal deposition, and solid-phase synthesis.

A hydrothermal method is a chemical reaction in water at both high temperature and under high pressure, which usually happened in a sealed pressurized vessel. This method is a simple yet efficacious way to fabricate TMS nanomaterials with controlled compositions and structures, and it can be easily realized *via* adjusting the metal salt precursors and temperature/pressure conditions. Luo *et al.* fabricated NiS_2 hollow microspheres using a hydrothermal approach with $Ni(NO_3)_2$ and $Na_2S_2O_3$ solutions as the Ni and S sources, respectively.[67] In this typical procedure, the precursors were dissolved in water and stirred with ethylene glycol and oxalic acid for 20 min before being transferred into a Teflon-lined stainless-steel autoclave, then heated at 180 °C for 12 h in an electric oven and cooled to room temperature naturally. Finally, the product was washed with deionized water and ethanol and dried overnight in a vacuum oven at 60 °C. Interestingly, when annealed under a mixed atmosphere, the obtained NiS_2 hollow microspheres could further be transformed into NiS porous hollow microspheres (Fig. 8a–c). Interestingly, Dong *et al.* synthesized hierarchical CoS with flower-like, ball-like, cube-like, and hollowed-out nanostructures *via* the one-pot hydrothermal reaction of $Co(NO_3)_2 \cdot 6H_2O$ and thiourea.[68] Thiourea played an important role in the reaction, as it decomposed to produce S^{2-} for the formation of CoS and served as a structure-directing agent to control the growth of CoS crystals. The morphologies of the CoS nanostructures formed could be modified *via* fine-tuning the molar ratios of the solvents and reactants, the reaction temperature, the reaction time, and the ligand type (Fig. 8d–i). The growth process of the flower-like CoS nanostructures could be divided into three stages: the formation of small-sized nanoflakes; the formation of a skeleton sphere *via* the attachment of nanoflakes through an Ostwald ripening mechanism; and the development of hierarchical flower-like nanostructures *via* a dissolution–recrystallization process.

Due to the ease of regulation of the reaction, effective element doping can be achieved easily using the hydrothermal method. Xiong *et al.* prepared Co-doped MoS_2 nanosheets with different Co content levels *via* a facile one-step hydrothermal approach.[69] During the reaction, $(NH_4)_6Mo_7O_{24} \cdot 4H_2O$, thiourea, and $Co(NO_3)_2 \cdot 6H_2O$ were applied as the precursors for the

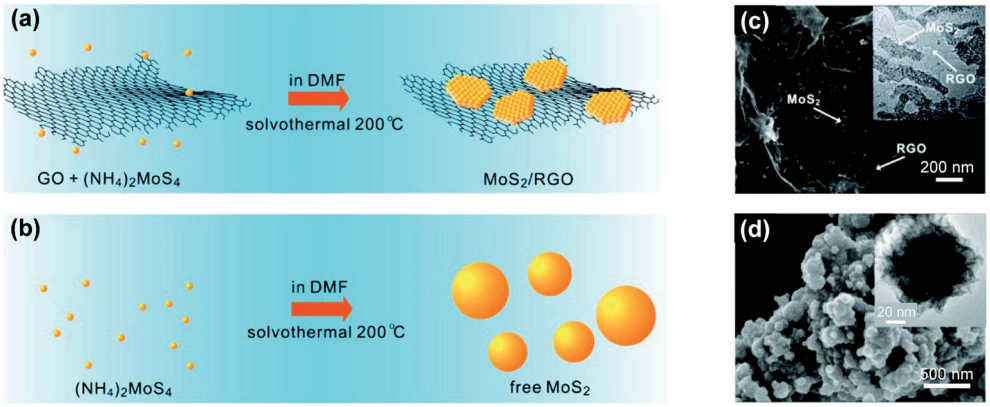

Fig. 9 (a and b) Schematic diagrams of the solvothermal synthesis of MoS_2 in solution with and without graphene sheets. (c and d) SEM and (insets) TEM images of the MoS_2/RGO hybrid and free MoS_2 particles.[70]

hydrothermal preparation of MoS_2 nanosheets covalently doped with Co. The level of Co doping could be regulated simply *via* changing the added amount of $Co(NO_3)_2 \cdot 6H_2O$ precursor. Remarkably, a hierarchical flower-like structure with improved conductivity was formed, composed of thin nanosheets, which could be employed as a superior bifunctional electrocatalyst for overall water splitting.

The solvothermal method is very similar to the hydrothermal method, except that an organic solution is applied as the precursor medium instead of water. Li *et al.* prepared MoS_2 nanoparticles on reduced graphene oxide (RGO) sheets *via* the one-step selective solvothermal reaction of $(NH_4)_2MoS_4$ and hydrazine in an *N*,*N*-dimethylformamide (DMF) solution of graphene oxide (GO) sheets at 200 °C (Fig. 9).[70] During this process, the $(NH_4)_2MoS_4$ precursor was reduced to MoS_2 nanoparticles that were laid uniformly and flatly on RGO that was formed from GO upon hydrazine reduction. Importantly, the GO sheets acted as a substrate for the nucleation and subsequent growth of MoS_2 nanoparticles, avoiding MoS_2 coalescing into 3D particles of various sizes. The selective growth of MoS_2 on GO could be attributed to interactions between the Mo precursor and the functional groups of the GO sheets in a suitable solvent environment, because when DMF was replaced with H_2O as the solvent, only two separate phases of MoS_2 and RGO could be obtained. Yuan *et al.* reported the direct growth of Fe-doped Ni_3S_2 nanosheet arrays on a conductive Fe–Ni alloy foil *via* a one-step solvothermal method.[71] A piece of Fe–Ni alloy foil was immersed into a mixture of Na_2S solution and ethanol, and this was then transferred into a Teflon-lined stainless-steel autoclave under N_2 flow. The reaction was carried out at 200 °C for 12 h in an electric oven and the obtained Fe-doped Ni_3S_2 nanosheet arrays grown *in situ* on the surface of the alloy foil could be applied as a self-supported electrode for water oxidation.

As key reaction factors in the solvothermal method, the temperature and precursor concentration exhibit great effects on the structural modification of CoS architectures, as proved by Wang *et al.*[72] 3D flower-like CoS architectures and CoS microspheres were synthesized through a one-pot solvothermal method using $CoCl_2 \cdot 6H_2O$ and thioacetamide as the precursors. According to crystal growth theory, the nucleation and subsequent growth of CoS could be regulated *via* adjusting the supersaturation of the reaction solution, which is related to the precursor concentration and temperature. CoS microspheres could be formed at a high starting precursor concentration, while flower-like CoS architectures were obtained at a low precursor concentration due to limited homogenous nucleation. Likewise, the higher the reaction temperature, the faster the nucleation rate and crystal growth rate. As a result, the controllable fabrication of various CoS nanostructures could be realized *via* a solvothermal route *via* synergistically adjusting the temperature and precursor concentrations, providing a promising way to synthesize TMS with specific morphologies and sizes.

Chemical vapor deposition (CVD) is defined as the deposition of solid materials onto a heated substrate from the vapor phase after several chemical reactions, which is well suited to the preparation of TMS thin films or nanoflakes with high crystallinity on a substrate. During the reaction, solid-state precursors of metal compounds or elemental metal will react with the sulfur source H_2S or vaporized S at high temperatures. Yuan *et al.* reported a facile CVD method to synthesize hexagonal 1T-VS_2 single-crystal nanosheets.[73] Typically, a vanadium chloride (VCl_3) precursor in an Al_2O_3 crucible was placed in a quartz tube at the center of the heating zone of a furnace. A SiO_2/Si substrate was placed on top of the crucible to collect the product. Sulfur was placed upstream of the quartz tube and it migrated with the carrier gas, a mixture of N_2 and 10% H_2, at ambient pressure. The furnace was gradually heated to 550 °C at a heating rate of 20 °C min^{-1} and it was cooled to room temperature naturally after being maintained at high temperature for 10 min. Well-aligned hexagonal and nearly "half-hexagonal" VS_2 nanosheets mostly parallel to the substrate could be obtained *via* tuning the addition of precursors.

Furthermore, in CVD, the reaction pressure and substrate both have great influence on the growth of TMS. Samad *et al.* directly synthesized phase-pure FeS_2 thin films with micron-sized crystalline domains *via* atmospheric pressure CVD with

metallic CoS_2 film as the substrate.[74] The synthesis of FeS_2 was achieved *via* reacting di-*tert*-butyl disulfide (TBDS) and $FeCl_3$ precursors at 400–450 °C. CoS_2 has the same cubic crystal structure as FeS_2 with only 2% lattice mismatch between them, so it is highly desirable as a film growth substrate that is unaffected by the sulfur atmosphere and as a conductive substrate for potential electrochemical applications. Subsequently, Shi *et al.* fabricated thickness-tunable TaS_2 flakes and ultrathin centimeter-sized films on gold (Au) foil *via* low-pressure CVD (LPCVD) and atmospheric-pressure CVD (APCVD) routes with $TaCl_5$ and S as precursors.[75] Replacing the general SiO_2/Si substrate for TMS growth with Au foil had great advantages, *e.g.*, Au foil could be applied as a metal catalyst for preparing TaS_2 and a conductive current collector of TaS_2-electrode, providing an opportunity to probe either fundamental physical phenomena or applications related to dimensionality effects. Intriguingly, TaS_2 tended to grow into centimeter-sized uniform, several-layer-thick 2H-TaS_2 thin films *via* the LPCVD route, while APCVD was an effective approach to grow TaS_2 with tailored thicknesses due to the excess precursor feeding rate in the synthesis procedure. Schematic illustrations of these two growth processes and the as-prepared TaS_2 are shown in Fig. 10.

For further optimizing the preparation conditions for the CVD growth of TMS, novel methods originating from CVD have been investigated in recent years, like plasma-enhanced CVD (PECVD) and metal–organic CVD (MOCVD). The reaction temperature could be lowered to 150–300 °C using a PECVD technique, thereby making it possible to deposit active TMS on plastic and flexible substrates. Kim *et al.* prepared uniform wafer-scale 1T-WS_2 film *via* a PECVD technique.[76] Different from common CVD methods, the plasma in an ionized gas state with ions and radicals does not have high thermal energy. The growth temperature was maintained at 150 °C, enabling the direct preparation of uniform and stable 1T-WS_2 films on both flexible polymer and rigid dielectric substrates. Specifically, organic–metallic precursors are used in MOCVD, and this method can be applied in modern semiconductor industries to prepare single-crystal epitaxial films. Song *et al.* prepared transferable few-layer MoS_2 structures with desired sizes and patterns *via* an MOCVD method with a Au catalyst.[77] The MOCVD reaction encompassed the following steps: the low-temperature reaction of $[Mo(CO)_6]$ and a pre-deposited Au thin film to form a Mo–Au surface alloy; and the reaction of the Mo–Au surface alloy with H_2S to obtain large-scale MoS_2 atomic layers that could be isolated from the substrate *via* etching the Au films. Importantly, the MoS_2 atomic layers could be fabricated with desired patterns through simply defining the pattern of the Au thin film *via* conventional lithographic techniques.

Solid-phase synthesis has been widely used to convert metal or metal compounds directly to TMS *via* a sulfurization process at high temperatures; it is also a promising method for fabricating self-supported TMS electrodes. Wang *et al.* reported hierarchical WS_2 film that was grown *in situ* on tungsten foil *via* one-step solid-phase synthesis, namely a surface-assisted chemical vapor transport method (Fig. 11a and b).[78] Tungsten foil and sulfur powder were sealed together in a small quartz ampoule under high vacuum and reacted at high temperature for 10 min to get thin WS_2 film with a hierarchical structure on the surface of the tungsten foil. Tungsten foil acted as the raw material for solid-phase synthesis and as the substrate for the nucleation and growth of WS_2 simultaneously. The strong interaction between WS_2 film and tungsten foil dramatically enhanced the electrical conductivity and electrocatalytic

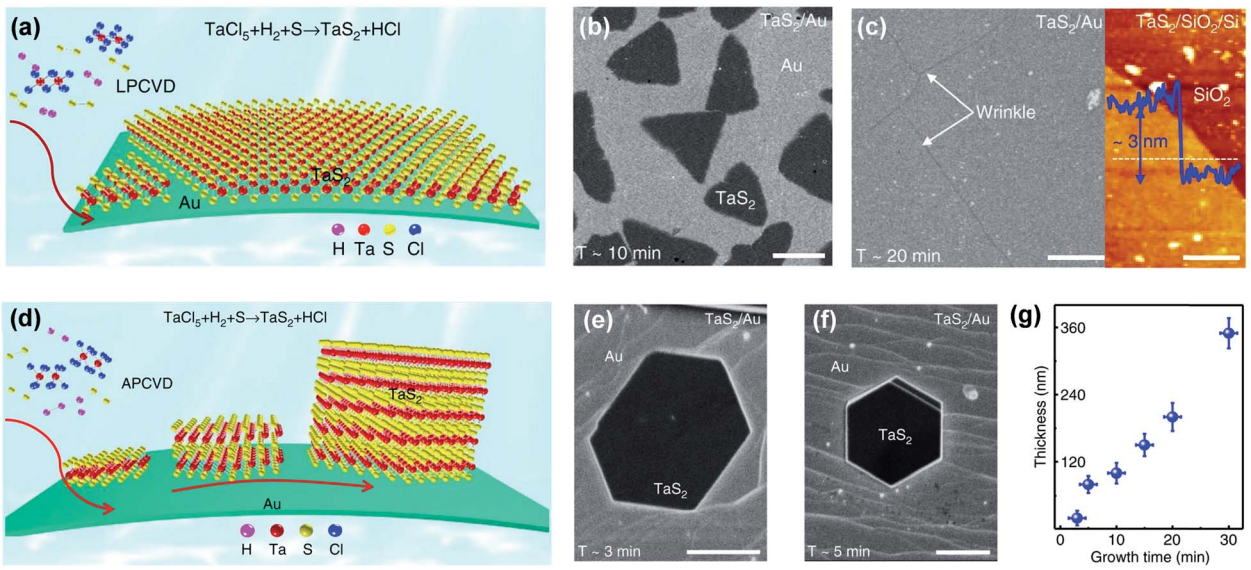

Fig. 10 (a) A schematic illustration of the LPCVD growth process of TaS_2. (b) An SEM image of 2H-TaS_2 flakes (synthesized at 750 °C for ~10 min) on Au foil. (c) An SEM image of 2H-TaS_2 flakes (synthesized at 750 °C for ~20 min) on Au foil, and an AFM height image of a transferred film edge. (d) A schematic illustration of the APCVD growth process of TaS_2. (e and f) SEM images of 2H-TaS_2 domains on Au foil with growth times of 3 and 5 min. (g) A plot of the tunable thickness of 2H-TaS_2 as a function of the growth time.[75]

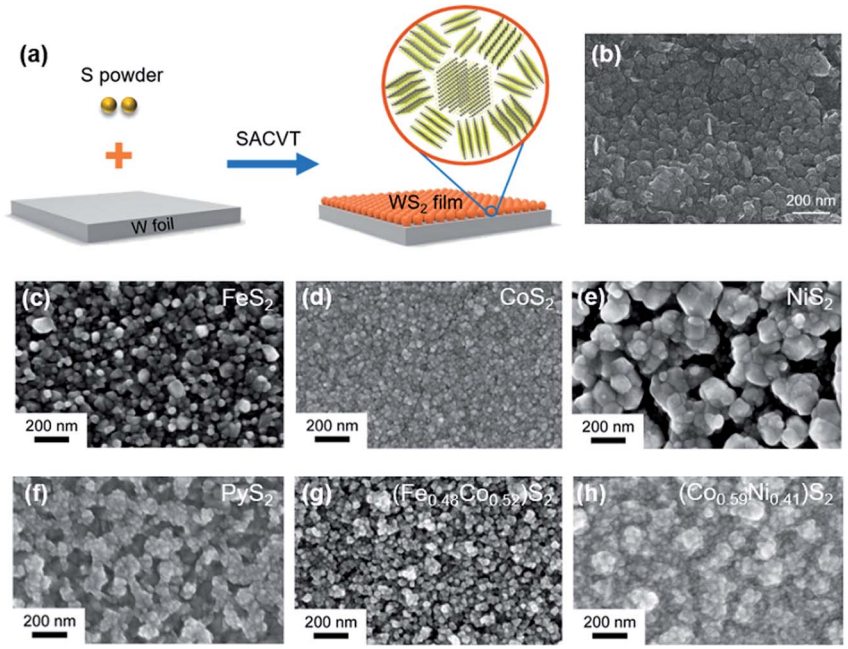

Fig. 11 (a) Schematic diagrams of WS_2 film on tungsten foil prepared *via* the SACVT method. (b) An SEM image of the WS_2 film.[78] (c–h) SEM images of FeS_2, CoS_2, NiS_2, PyS_2, $(Fe_{0.48}Co_{0.52})S_2$, and $(Co_{0.59}Ni_{0.41})S_2$ thin films on graphite disk substrates prepared *via* solid-phase synthesis.[80]

durability of this self-supported WS_2 electrode. Jin *et al.* fabricated vertically oriented single-crystal FeS_2 nanowires from steel foil *via* solid-phase synthesis.[79] During the sulfurization procedure, low-carbon steel foil, placed near the hot zone of the tube, was heated at 350 °C for 2 h under a sulfur atmosphere that was formed *via* evaporation from upstream sulfur powder.

What is more, metal sources can be deposited onto other substrates to reduce the utilization of metal. Faber *et al.* prepared pyrite-phase FeS_2, CoS_2, and NiS_2 thin films and thin films of their alloys *via* a simple solid-phase synthesis reaction (Fig. 11c–h).[80] Firstly, high-purity metal was deposited on the polished surface of a graphite disk substrate *via* electron-beam evaporation. To prepare ternary pyrite alloy films, metal bilayers containing two kinds of metals were sequentially evaporated onto graphite disk substrates. Finally, the metalized substrates were loaded into the center of a fused silica tube and heated at 500 °C for 1 h under a sulfur atmosphere until they were converted into their corresponding disulfides. In particular, solid-phase synthesis could also be combined with other methods, such as hydrothermal, solvothermal, and sol–gel methods. Miao *et al.* prepared mesoporous FeS_2 materials with large surface areas using a sol–gel method followed by solid-phase synthesis treatment.[81] Amorphous Fe_2O_3 was first obtained *via* an inverse micelle sol–gel method, and it was then sulfurized to FeS_2 using H_2S gas and sulfur powder as sulfur sources.

Except for the direct growth of TMS materials on substrates, TMS powder can also be synthesized *via* solid-phase synthesis. Single-crystal FeS_2 nanorods, nanobelts, and nanoplates have been prepared *via* the solid-phase synthesis reaction of $FeCl_2$ or $FeBr_2$ with sulfur powder at high temperatures.[82] During solid-phase synthesis reactions, dehydrated $FeCl_2$ or $FeBr_2$ precursor powder was heated at 425 °C under a flowing sulfur atmosphere to produce phase-pure cubic iron pyrite. Interestingly, Bara *et al.* investigated the effects of the degree of sulfurization on the preparation of MoS_2 slabs on an α-Al_2O_3 substrate from MoO_3 upon reaction with a H_2S/H_2 gas phase.[83] The degree of sulfurization during solid-phase synthesis strongly depended on the surface orientation of the α-Al_2O_3 substrate, and this had a clear impact on the strength of the metal–support interactions in the oxide states with consequences for the sulfurization, stacking, size, and orientation of MoS_2 slabs. Eventually, the maximum degree of sulfurization was about 90% at low temperature (300 °C) for the C (0001) plane with a larger MoS_2 slab size. However, the solid-phase synthesis process in this case was similar to the CVD method.

In summary, numerous effective preparation methods have been established for the fabrication of high-quality TMS materials, which could be divided into 'bottom-up' and 'top-down' strategies. From the viewpoint of surface morphology, the obtained TMS exhibited different morphologies, *e.g.*, nanodots, nanoparticles, nanosheets, flower/ball/cube-like nanostructures, microspheres, and thin films, which strongly depended on the synthesis method and conditions used. The experimental parameters all play key roles in the controllable synthesis of TMS materials, such as the sulfur/metal source type, the precursor concentration, the solvent type, and the reaction temperature/time. Importantly, self-supported TMS electrodes could be fabricated *via* the sulfurization of metal substrates. Although various methods have been successfully employed to prepare TMS materials, the growth mechanisms of TMS materials with different morphologies and compositions

remain unclear; these require more investigation in order to deeply understand the underlying behavior.

4. Water splitting properties of TMS

Numerous efforts have been made to develop efficient and inexpensive bifunctional electrocatalysts for electrochemical water splitting. Of these new bifunctional electrocatalysts, TMS have attracted extensive research attention due to their excellent electrocatalytic performance, wide availability, and low cost. Countless TMS have been explored and their great potential for efficiently catalyzing the HER or OER has been revealed. Nevertheless, most of these TMS electrocatalysts can only be utilized for either the HER or OER because of their intrinsic electrochemical properties; this can restrict their electrocatalytic activity and durability, with strong dependence on the pH of the electrolyte. For instance, most HER electrocatalysts are more active in acidic electrolytes, while most effective electrocatalysts for the OER exhibit high solubility in acidic electrolytes and thus are restricted to alkaline media. Consequently, discovering and designing bifunctional electrocatalysts with high activity and durability for both the HER and OER in the same electrolyte is technologically important. This section comprehensively reviewed the intrinsic electrocatalytic performance and optimizing strategies of layered TMS (M = Mo, W, Ta, *etc.*) and non-layered TMS (M = Fe, Co, Ni, *etc.*) for overall water splitting.

4.1 Bifunctional layered TMS (MS_2: Mo, W, Ta, *etc.*) electrocatalysts

4.1.1 Intrinsic electrocatalytic performance. Layered TMS with versatile and tunable properties have been extensively studied as robust substitutes for noble metals for electrocatalyzing the HER. For example, MoS_2,[84] WS_2,[78] TaS_2,[85] and NbS_2 (ref. 86) all can be applied as HER electrocatalysts with excellent activity and stability. Lin *et al.* chemically unzipped WS_2 nanotubes to make metallic WS_2 nanoribbons with increased edge active site content and high electrical conductivity.[87] The enhanced electrocatalytic HER activity of WS_2 is strongly associated with its well-exposed edge defects. Moreover, Lukowski *et al.* exfoliated metallic 1T-MoS_2 nanosheets *via* lithium intercalation from semiconducting 2H-MoS_2 nanostructures.[36] The metallic 1T-MoS_2 nanosheets boosted the electrocatalytic HER activity with a low overpotential of -187 mV at 10 mA cm^{-2} and a small Tafel slope of 43 mV dec^{-1}, showing facile electrode kinetics, low-loss electrical transport, and a proliferated density of active sites. While the basal plane of 2H-MoS_2 is nonreactive, the basal plane of 1T-MoS_2 is active; this mainly arises from the affinity of the surface S sites for binding H species.[88]

Hence, the well-exposed edge sites and good electrical conductivity properties of layered TMS mean they show remarkable intrinsic electrocatalytic HER activities. However, these kinds of TMS are not intrinsically suitable as OER electrocatalysts, and little research has been reported in which they could be directly used for electrocatalyzing the OER. In a rare example, pure 2H-TaS_2 nanoflakes were reported to have the potential to electrocatalyze both OER and HER processes with overpotentials of 315 mV and 145 mV, respectively, at 10 mA cm^{-2},[89] and MoS_2 microspheres on conductive Ni foam, with enhanced conductivity and accelerated electron transfer, showed great potential for OER applications.[90] More effort should be devoted to expanding the application of these layered TMS to the OER.

4.1.2 Strategies for optimizing the electrocatalytic performance of layered TMS. To make these layered TMS more suitable for both the HER and OER, numerous efforts have been put forward to optimize their electrochemical properties *via* improving the intrinsic electrical conductivity, enhancing the chemisorption capabilities for O-containing species, and/or improving stability. Practically, three main strategies are used to achieve this goal: phase engineering, composite designing, and heteroatom doping.

Phase engineering is a promising way to regulate the electrocatalytic OER activities of layered multiphase TMS. Traditionally, phase transformation can be realized *via* various strategies, such as chemical exfoliation, ion intercalation, strain engineering, and heteroatom doping. Wu *et al.* exfoliated 2D MoS_2 and TaS_2 nanosheets obtaining both 2H and 1T polymorphs and explored their electrocatalytic OER performances in an acidic medium.[91] The best OER performance, which was comparable to a benchmark IrO_2 electrocatalyst, came from 1T-MoS_2, followed by 1T-TaS_2, 2H-MoS_2, and 2H-TaS_2, unraveling the polymorphic dependence of the electrocatalytic OER activity. A theoretical study also revealed the same electrocatalytic activity trend, in which the 1T polymorph showed higher activity than the 2H layered TMS counterpart. Additionally, Wei *et al.* found that the spontaneous phase transformation of MoS_2 from the 2H to 1T phase was triggered by strong metal–support interactions during iridium (Ir) adsorption on the surface of 2H-MoS_2.[92] Strong charge transfer between MoS_2 and the adsorbed Ir atoms could promote the phase transformation of MoS_2 and enhance the electrocatalytic activity for overall water splitting, which was superior to even commercial Pt/C and IrO_2 electrodes. The significantly improved electrocatalytic performance could be ascribed to enhanced electrical conductivity and hydrophilicity, increased numbers of interfaces and active sites, and the activated basal plane of MoS_2. The strong synergistic and coupling effects between 1T-MoS_2 and Ir atoms markedly accelerated the reaction kinetics in alkaline solution.

Composite designing is the most attractive strategy for obtaining layered TMS-based bifunctional electrocatalysts for overall water splitting, and it involves integrating layered TMS with other active materials to construct novel heterostructures or composites. As we know, layered TMS can be employed as excellent HER electrocatalysts while they exhibit poor electrocatalytic OER performance. In turn, first-row metal compounds generally are preferred alternatives to noble metal oxides (IrO_2, RhO_2, or RuO_2) in the OER, such as metal sulfides, oxides, and hydroxides.[24] Hence, assembling a layered TMS with high activity for the HER with an active OER electrocatalyst in one system is a good choice for building highly effective

bifunctional electrocatalysts. The newly formed composite/heterostructure would possess enhanced electrochemical water-splitting performance due to the synergistic effect of the counterparts.

Based on this design concept, Zhang *et al.* fabricated MoS_2/Ni_3S_2 heterostructures with abundant interfaces on nickel (Ni) foam *via* decorating MoS_2 nanosheets on the surfaces of Ni_3S_2 nanoparticles (Fig. 12a–c).[93] The novel MoS_2/Ni_3S_2 heterostructures possessed both highly efficient OER and HER activities in alkaline solution, with overpotentials at 10 mA cm^{-2} as low as 218 mV and 110 mV, respectively. Furthermore, an alkaline electrolyzer assembled using the as-prepared MoS_2/Ni_3S_2 heterostructures could deliver a current density of 10 mA cm^{-2} at a low cell voltage of 1.56 V. Based on DFT calculations, the constructed interfaces between MoS_2 and Ni_3S_2 could synergistically facilitate the chemisorption of hydrogen- and oxygen-containing intermediates, thus enhancing the electrocatalytic performance for water splitting. Subsequently, Peng *et al.* prepared three-dimensional (3D) Co_9S_8/WS_2 array films on titanium (Ti) foil, in which WS_2 nanosheets were uniformly grown *in situ* on the surfaces of Co_9S_8 array structures to form hybrids with large electrochemically active surface areas.[94] Co_9S_8/WS_2 array films displayed superior electrocatalytic activity for both the HER and OER with a low cell voltage of 1.65 V at 10 mA cm^{-2} when acting as both the cathode and the anode. The good performance for water splitting was ascribed to the unique porous structure and the synergistic effect of electronic and chemical coupling between active WS_2 and Co_9S_8, which resulted in suitable kinetics and energetics for hydrogen adsorption and H_2 formation processes and facilitated electron transport during water electrolysis. To further strengthen the activity and durability, the construction of oxygenated-sulfide hetero-nanosheets was subsequently put forward. Hou *et al.* grew vertically aligned oxygenated-MS_2–MoS_2 (M = Fe, Co, or Ni) hetero-nanosheets on carbon fiber cloth using bimetal precursors through a hydrothermal strategy.[95] Among these samples, O-CoS_2–MoS_2 hetero-nanosheets presented the best performance, with low overpotentials of 97 and 272 mV to deliver a current density of 10 mA cm^{-2} for the HER and OER, respectively, in alkaline electrolyte. This unique architecture with well-exposed active hetero-interfaces, ultra-fast charge-transport channels, and abundant active sites was highly favorable for obtaining enhanced electrocatalytic performance, which was derived from the synergistic effect of heterostructures. When assembled in a two-electrode electrolyzer, O-CoS_2–MoS_2 hetero-nanosheets merely needed a low cell voltage of 1.6 V to reach a current density of 10 mA cm^{-2}.

Motivated by this research progress relating to active bimetal transition-metal sulfides, Yang *et al.* proposed the construction of 3D composites co-assembled from MoS_2 and Co_9S_8 nanosheets that were attached to Ni_3S_2 nanorod arrays.[97] The as-prepared MoS_2/Co_9S_8/Ni_3S_2 supported by Ni foam showed controllable morphologies and compositions, and it demonstrated excellent bifunctional electrocatalytic performance for both the HER and OER over a full pH range. Notably, the optimal sample could reach 10 mA cm^{-2} at very low overpotentials of 103, 117, and 113 mV for the HER in alkaline, neutral, and acidic solutions, respectively, while it required extremely low overpotentials of 166, 228, and 405 mV for the OER. In addition, a two-electrode electrolyzer assembled from MoS_2/Co_9S_8/Ni_3S_2 composites also only required low cell voltages of 1.54, 1.80, and 1.45 V to obtain a current density of 10 mA cm^{-2} in alkaline, neutral, and acidic media, respectively. The superior performance of the all-pH bifunctional MoS_2/Co_9S_8/Ni_3S_2 electrocatalyst was attributed to enhanced electron

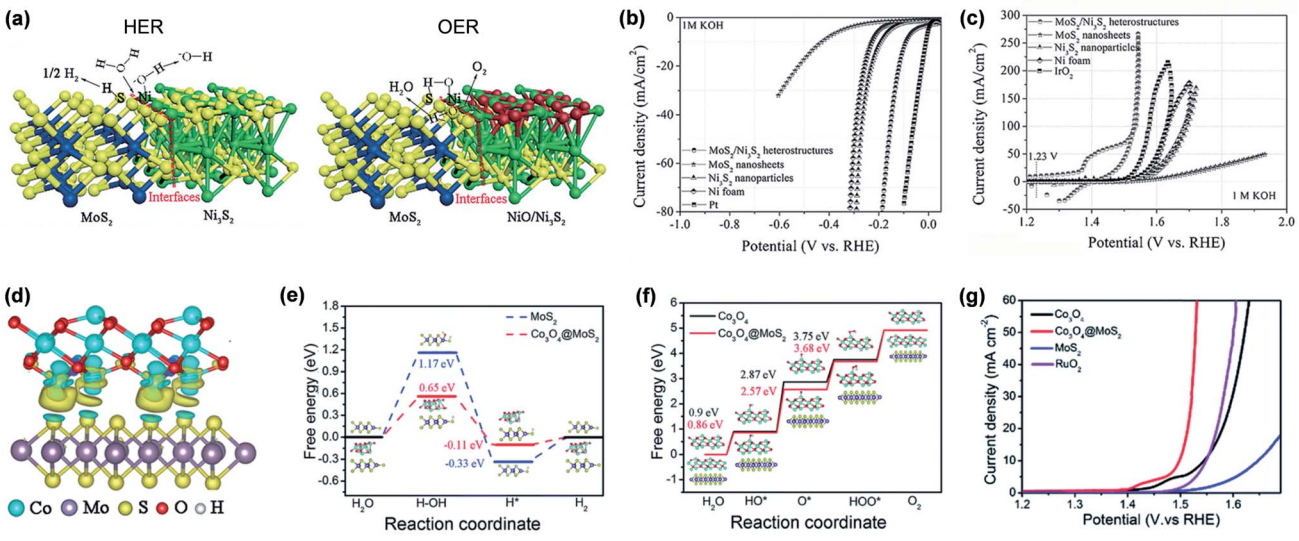

Fig. 12 (a) The proposed HER and OER mechanisms on MoS_2/Ni_3S_2 heterostructures; S: yellow, Mo: blue, Ni: green, H: white, and O: red. (b) Polarization curves and (c) CV curves from MoS_2/Ni_3S_2 heterostructures, MoS_2 nanosheets, Ni_3S_2 nanoparticles, Ni foam, and IrO_2/Pt.[93] (d) A schematic diagram of interfacial electron transfer between MoS_2 and Co_3O_4. (e) A free energy diagram of the HER on Co_3O_4@MoS_2 and MoS_2. (f) A free energy diagram of the OER on Co_3O_4@MoS_2 and Co_3O_4. (g) Polarization curves of MoS_2, Co_3O_4, and Co_3O_4@MoS_2 in 1 M KOH.[96]

and mass transfer, and the well-exposed active sites of MoS_2 and Co_9S_8 supported by a substrate with a 3D frame. The development of universal-pH bifunctional electrocatalysts has great significance for industrial applications involving seawater electrolysis.

As well as metal sulfides, layered TMS can also be integrated with other synergistic materials into well-designed architectures to achieve highly effective bifunctional electrocatalysts, like metal oxides, metal carbonitrides, and metal oxyhydroxides. Wang *et al.* innovatively prepared a WS_2 nanosheet array on carbon cloth and then decorated NiO@Ni onto the surface *via* electrodeposition and subsequent thermal oxidation.[98] This NiO@Ni/WS_2 synergistic electrocatalyst possessed Pt-like activity for the HER with only a low overpotential (40 mV) being needed to drive 10 mA cm^{-2}. Moreover, when serving as an anode for the OER, it required just 347 mV to deliver a current density of 50 mA cm^{-2}, which was superior to even commercial RuO_2. Excitingly, an electrolyzer with a two-electrode setup based on NiO@Ni/WS_2 composites could afford 10 mA cm^{-2} at an extremely low cell voltage of 1.42 V. The marvelous enhanced bifunctional electrocatalytic performance of the NiO@Ni/WS_2 composite may arise from the unique nanosheet array structure and multicomponent synergetic effects among WS_2, NiO, and Ni. What is more, Liu *et al.* designed Co_3O_4@MoS_2 heterostructures with balanced HER and OER performances.[96] Theoretical and experimental results revealed that the heterostructures synergistically favored reducing the energy barrier for initial water dissociation, optimizing subsequent H adsorption/desorption for the HER, and enhancing the adsorption of oxygen intermediates for the OER (Fig. 12d–g). Analogously, Ji *et al.* grafted thin MoS_2 nanosheets onto MOF-derived porous Co–N–C flakes and grew them on carbon nanofibers to get excellent bifunctional CoNC@MoS_2/CNF films.[99] The resultant CoNC@MoS_2/CNFs with hierarchical structures and superior flexibility exhibited remarkable activities and stabilities for both the HER and OER in 1 M KOH. Regarding water electrolysis, a low cell voltage of 1.62 V was required to generate a current density of 10 mA cm^{-2}, which could be ascribed to the high activity and rapid mass transport derived from a synergistic effect between MoS_2 and Co–N–C flakes. Undoubtedly, MoS_2 as a remarkable and representative layered TMS should be widely investigated to exploit its capacity for water splitting.

The stable phase of MoS_2 is the thermally preferred 2H phase, while free-standing 1T-MoS_2 suffers from an unstable nature. Integrating MoS_2 with other active materials can not only improve the electrocatalytic activity significantly but can also stabilize unstable 1T-MoS_2 *via* serving as a substrate. Shang *et al.* embedded atomically thin 1T-MoS_2 in quasi-amorphous CoOOH *via* a facile one-pot method to achieve a bifunctional electrocatalyst for overall water splitting.[100] The synthesized 1T MoS_2–CoOOH heterostructure exhibited highly efficient activity, with overpotentials of 158 mV in 0.5 M H_2SO_4 for the HER and 345 mV in 1 M KOH for the OER at 10 mA cm^{-2}. In this heterostructure, the vertical 1T-MoS_2 monolayer contributed mainly to the excellent HER activity, while the CoOOH nanosheets could provide superior OER activity. Importantly, the CoOOH nanosheets could also anchor and stabilize the 1T-MoS_2 monolayer, achieving a stable architecture, *via* acting as an electron donor to facilitate the phase transition and stabilization of the metallic phase, which also paved the way to the controllable synthesis of thermodynamically unstable phases of layered TMS.

Heteroatom doping is an effective strategy for regulating the fundamental properties of layered TMS and constructing efficient bifunctional electrocatalysts. On one hand, the heteroatoms can directly break the periodic crystalline structure of materials *via* generating defects and distortions in the lattices of layered TMS; this is mainly due to differences between the atomic radii of host atoms and heteroatoms. These defects and distortions can create more active sites for electrocatalytic reactions and increase the reactivity of the surface.[101] On the other hand, the introduction of heteroatoms can modulate the surface electronic structure of layered TMS through breaking the original charge balance, building a new charge distribution, and generating localized charge aggregation. The modulated electronic structure could further optimize the chemical adsorption energies of reactive intermediates and change the reaction pathways during water splitting.[102] All these advantageous effects can promote the formation of electrocatalysts with bifunctionality and enhanced performance for water splitting. Heteroatom doping strategies can be divided mainly into two types: substitutional doping and surface charge transfer doping.[103]

In the case of substitutional doping, metal atoms or S atoms in layered structures are substituted with heteroatoms with different valence electrons. Xiong *et al.* developed a covalent Co doping strategy to induce bifunctionality into MoS_2 for effective water splitting (Fig. 13c).[104] Co atoms replaced Mo atoms to obtain MoS_2 covalently doped with Co, which possesses enhanced intrinsic conductivity, a decreased ΔG_H value upon optimizing the electronic structure of MoS_2, and improved OER activity, which was ascribed to Co species in a high valence state under anodic potentials. Consequently, the best-performing MoS_2 covalently doped with Co exhibited overpotentials of 48 and 260 mV to afford a current density of 10 mA cm^{-2} during the HER and OER, respectively, in 1.0 M KOH. A resultant electrolyzer assembled from MoS_2 covalently doped with Co could generate 4.5 and 9.1 μmol min^{-1} O_2 and H_2, respectively, with nearly 100% faradaic efficiency. Specially, it should also be noted that the covalent doping of Ni and P into 1T-enriched MoS_2 could significantly activate the basal planes, expand the interlayer spacing, and increase the edge density of 1T-enriched MoS_2 in bifunctional nanostructures for water splitting.[105] Further, Xue *et al.* prepared bifunctional Fe-doped MoS_2 nanocanopies on Ni foam (Fe-MoS_2/NF) *via* an *in situ* solvothermal reaction.[106] Fe doping would modify the electronic structure of Mo, and some Fe would likely be present as iron sulfide. Strong coupling interactions between Fe and MoS_2 markedly promote the electrocatalytic activity. The Fe-MoS_2/NF electrode exhibited an OER overpotential of 230 mV at 20 mA cm^{-2} and a HER overpotential of 153 mV at 10 mA cm^{-2} in 1.0 M KOH.

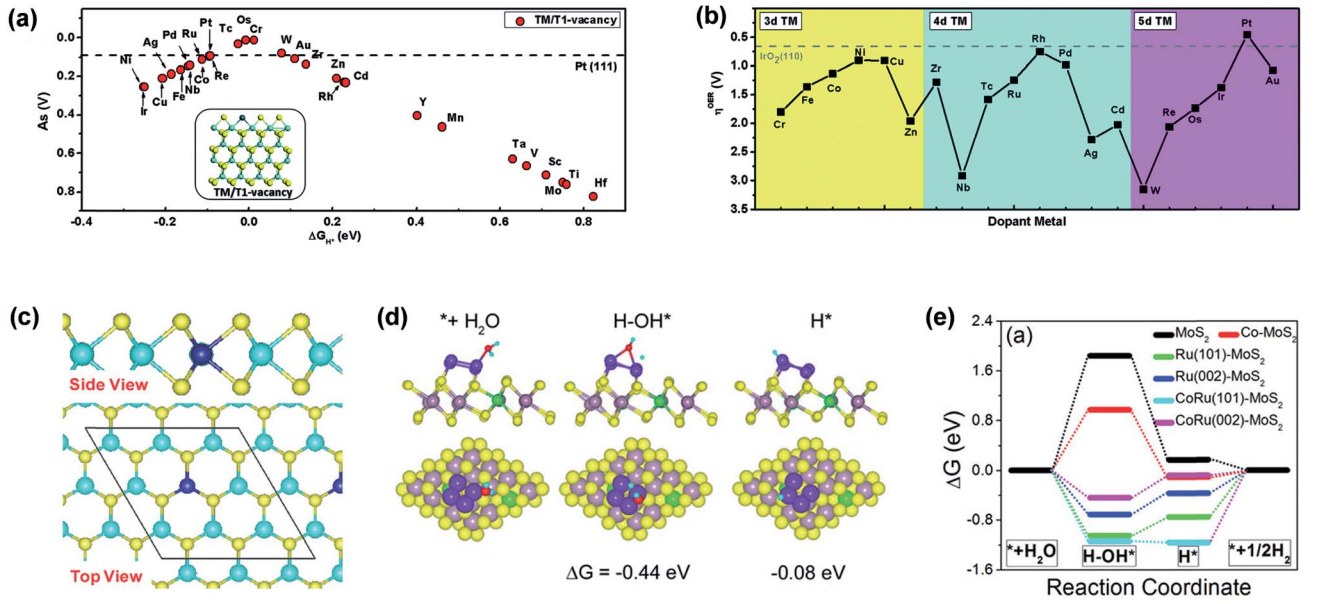

Fig. 13 (a) HER activity as a function of the Gibbs free adsorption energy of hydrogen and the configuration of TM/T1-vacancies. (b) The OER overpotentials of TM-doped T1 vacancy terminations; TM is a transitional metal and a T1 vacancy means that 37.5% of S atoms are added to initial Mo termini.[107] (c) Side and top views of the optimized structure of MoS_2 covalently doped with Co; Mo: green, S: yellow, and Co: blue.[104] (d) The optimized geometries of CoRu(002)–MoS_2 with absorbed intermediates; Mo: grayish purple, S: yellow, Ru: purple, Co: green, H: cyan, and O: red. (e) Gibbs free energy diagrams of the H_2 production pathway (*via* the Volmer–Heyrovsky reaction in alkaline solution) on different samples.[108]

Surface charge transfer doping is realized *via* electron exchange between layered TMS and materials adsorbed on their surfaces. The introduction of doped heteroatoms is a viable method for triggering the bifunctional electrocatalytic activity of layered TMS, as has been proved *via* theoretical methods. Cheng *et al.* screened 28 transition-metal single-atom catalysts (SACs) supported on the edges of MoS_2 as bifunctional electrocatalysts based on DFT calculations (Fig. 13a and b).[107] These SACs could trigger OER activity and maintain the HER performance of MoS_2 edges. The OER activity was calculated *via* a simple equation including the electronegativity of the atoms in the local structure and the coordination number of active metal centers. The lowest theoretical overpotentials for the HER and OER were derived from MoS_2 edges modified with Pt single atoms. Pt single atoms enhanced the intrinsic HER activity of MoS_2 *via* modifying the bonds between S/Mo atoms and H and improved the OER activity *via* influencing the coordination environment and adsorption energy. This work provided theoretical guidance for developing innovative bifunctional electrocatalysts for overall water splitting.

Additionally, the synergistic effect of substitutional doping and surface charge transfer doping could lead to the great enhancement of the electrocatalytic performance of layered TMS. Kwon *et al.* doped metallic 1T′-MoS_2 with Co atoms and further decorated this material with Ru nanoparticles (size = 1–5 nm) to prepare unique Co–Ru–MoS_2 nanosheets for overall water splitting (Fig. 13d and e).[108] Co atoms substituted for Mo atoms homogeneously and Ru nanoparticles were deposited on the surface of Co-doped MoS_2. The enhanced HER performance in 1.0 M KOH was characterized based on the low overpotential of 52 mV at 10 mA cm^{-2} and small Tafel slope of 55 mV dec^{-1}, and this was attributed to favorable water adsorption and dissociation on Ru atoms and advantageous reaction intermediates being catalyzed by Co atoms. The high OER performance benefitted from active RuO_2 that was generated due to the oxidation of Ru nanoparticles, exhibiting a low overpotential of 308 mV at 10 mA cm^{-2} and a small Tafel slope of 50 mV dec^{-1}. In short, the synergistic effect of doped Co atoms and active Ru nanoparticles could bring about excellent bifunctional electrocatalytic performance for overall water splitting *via* producing optimized electronic structures.

In conclusion, layered TMS exhibit excellent intrinsic electrocatalytic HER activities due to their well-exposed edge sites and good electrical conductivity, while their bifunctional electrocatalytic performances for water electrolysis could be optimized *via* some strategies such as phase engineering, composite designing, and heteroatom doping. Currently, MoS_2-based and WS_2-based bifunctional electrocatalysts are the most widely investigated materials in the layered TMS family, and they were always coupled with other active materials. To reach a current density of 10 mA cm^{-2} in the HER, a NiO@Ni/WS_2 composite only requires an overpotential of 40 mV with a low Tafel slope of 83.1 mV dec^{-1} in 1.0 M KOH, which is even superior to Pt.[98] To obtain 10 mA cm^{-2} in the OER, the best performance is shown by a $MoS_2/Co_9S_8/Ni_3S_2$ composite, which only needs a small overpotential of 116 mV in 1.0 M KOH.[97] A summary of current layered TMS-based bifunctional electrocatalysts is shown in Table 1, and further investigations should put more effort into the design of novel composites.

Table 1 A summary of layered TMS-based bifunctional electrocatalysts for overall water splitting

TMS-based material	Preparation method	Electrolyte	Reaction/J (mA cm^{-2})	Overpotential η (mV)	Tafel slope (mV dec^{-1})	Cell voltage (V @ mA cm^{-2})	Stability
2H-TaS_2 nanoflakes[89]	Solid-state + hydrothermal	1 M KOH	HER/10, OER/10	145, 315	121, 81	—	—
Co_9S_8/WS_2 array films[94]	Hydrothermal + solid-phase synthesis	1 M KOH	HER/10, OER/10	138, —	80.2, —	1.65	24 h
NiO@Ni/WS_2 (ref. 98)	Hydrothermal + solid-phase synthesis	1 M KOH	HER/10, OER/50	40, 347	83.1, 108.9	1.42	40 h
MoS_2/Ni_3S_2 heterostructures[93]	Solvothermal	1 M KOH	HER/10, OER/10	110, 218	83, 88	1.56	10 h
MoS_2/Ni_3S_2 heteronanorods[161]	Hydrothermal	1 M KOH	HER/10, OER/10	98, 248	61, 57	1.50	48 h
MoS_2/Ni_3S_2 nanorod arrays[144]	Hydrothermal	1 M KOH	HER/10, OER/10	187, 217	90, 38	1.467	24 h
MoS_2/Ni_3S_2/Ni foam[162]	Electrodeposition + solvothermal	1 M KOH	HER/10, OER/10	99, 185	71, 46	1.50	48 h
MoS_2/NiS_2 nanosheets[151]	Hydrothermal + solid-phase synthesis	1 M KOH	HER/10, OER/10	62, 278	50.1, 91.7	1.59	24 h
MoS_2/NiS yolk–shell microspheres[163]	Hydrothermal	1 M KOH	HER/10, OER/10	244, 350	97, 108	1.64	24 h
Ni_3S_2–MoS_x/Ni foam[164]	Solvothermal	1 M KOH	HER/10, OER/50	65, 312	81, 103	1.54	20 h
CoNC@MoS_2/CNF films[99]	Carbonization + solvothermal	1 M KOH	HER/10, OER/10	143, 350	68, 51.9	1.62	56 h
MoS_2/Co_9S_8/Ni_3S_2 composites[97]	Hydrothermal	1 M KOH	HER/10, OER/10	113, 116	85, 58	1.54	24 h
		0.5 M H_2SO_4	HER/10, OER/10	103, 228	55, 78	1.45	80 min
		1.0 M PBS	HER/10, OER/10	117, 405	56, 71	1.80	20 h
MoS_2/Co_9S_8/N-carbon heterostructures[165]	Solvothermal	1 M KOH	HER/10, OER/10	95, 230	94, 77	1.63	25 h
1T MoS_2–CoOOH[100]	Hydrothermal	0.5 M H_2SO_4, 1 M KOH	HER/10, OER/10	158, 345	42, 59	—	20 h
O–CoS_2–MoS_2 heteronanosheets[95]	Hydrothermal	1 M KOH	HER/10, OER/10	97, 272	70, 45	1.60	10 h
CoS_x@MoS_2 heterostructures[166]	Solvothermal	1 M KOH	HER/10, OER/10	146, 276	56.5, 26.1	1.668	20 h
Ni–Fe-LDH/MoS_2 superlattices[167]	Exfoliation + assembly	1 M KOH	HER/10, OER/10	180, 250	67, 45	1.4	11 h
(Ni, Fe)S_2@MoS_2 heterostructures[168]	Hydrothermal	1 M KOH	HER/10, OER/10	130, 270	101.22, 43.21	1.56	45 h
1T′-MoS_2/(Co, Fe, Ni)$_9S_8$ nanotube arrays[118]	Solvothermal	1 M KOH	HER/10, OER/10	58, 184	37.5, 49.9	1.429	80 h
MoS_2–NiS_2/N-doped graphene[169]	CVD	1 M KOH	HER/10, OER/10	172, 370	70, —	1.64	24 h
CoS–Co$(OH)_2$@MoS_{2+x} (ref. 170)	Hybridization	1 M KOH	HER/10, OER/10	143, 380	68, 68	1.58	11 h
CoS_2–C@MoS_2 nanofibers[171]	Hydrothermal	1 M KOH	HER/10, OER/10	173, 391	61, 46	—	1000 cycles
CoS_2–MoS_2 hollow spheres[172]	Solvothermal	1 M KOH	HER/10, OER/10	109, 288	52, 62.1	1.61	10 h
Co_3S_4@MoS_2 heterostructures[173]	Hydrothermal	1 M KOH	HER/10, OER/10	136, 280	43, 74	1.58	10 h
Co_9S_8@MoS_2/carbon nanofibers[120]	Solid-phase synthesis	1 M KOH	HER/10, OER/10	190, 430	110, 61	—	12 h
Co_3O_4/MoS_2 heterostructures[96]	Hydrothermal	1 M KOH	HER/10, OER/10	90, 269	59.5, 58	1.59	12 h
Co_3O_4/MoS_2 heterostructures[174]	Hydrothermal	1 M KOH	HER/10, OER/20	205, 230	98, 45	—	14 h
Ni_2P/MoO_2@MoS_2 nanomaterials[175]	Solid-phase synthesis + phosphorization	1 M KOH	HER/10, OER/10	159, 280	77, 85	1.72	40 h

Table 1 (*Contd.*)

TMS-based material	Preparation method	Electrolyte	Reaction/J (mA cm^{-2})	Overpotential η (mV)	Tafel slope (mV dec^{-1})	Cell voltage (V @ mA cm^{-2})	Stability
Phosphorene quantum dot/MoS_2 nanosheets[176]	Electrochemical	0.1 M KOH	HER/10, OER/10	600, 370	162, 46	—	15 h
N–Ni_3S_2/N–MoS_2 heteronanowires[177]	Solid-phase synthesis	1 M KOH	HER/10, OER/200	54, 387	104.5, 101.2	1.79 @ 100	15 h
MoS_2/NiS nanosheets[178]	Solvothermal + solid-phase synthesis	1 M KOH	HER/10, OER/15	92, 271	113, 53	1.61	80 h
Co_3S_4@MoS_2–Ni_3S_2 nanorods[179]	Hydrothermal	1 M KOH	HER/10, OER/50	136, 270	72, 69	—	30 h
MoS_2/NiCoS nanosheets[180]	Solvothermal	1 M KOH	HER/10, OER/10	189, 290	75, 77	1.5	22 h
MoS_2/$Fe_5Ni_4S_8$ heterostructures[181]	CVD	1 M KOH	HER/10, OER/10	120, 204	45.1, 28.1	—	10 h
Amorphous Ni–Co complexes/1T-MoS_2 (ref. 182)	Solvothermal	1 M KOH	HER/10, OER/10	70, 235	38.1, 45.7	1.44	48
MoS_2/(Co, Ni and Fe) sulfide[183]	Solvothermal	1 M KOH	HER/100, OER/10	359, 178	76, 35.7	—	32 h
Fe–MoS_2/Ni_3S_2 (ref. 184)	Solvothermal	1 M KOH	HER/10, OER/10	130.6, 256	112.7, 59.5	1.61	180 h
Co–MoS_2 (ref. 104)	Hydrothermal	1 M KOH	HER/10, OER/10	48, 260	52, 85	—	11 h
Fe–MoS_2 nanocanopies[106]	Solvothermal	1 M KOH	HER/10, OER/20	153, 230	85.6, 78.7	1.52	140 h
Co–Ru–MoS_2 nanosheets[108]	Hydrothermal	1 M KOH	HER/10, OER/10	52, 308	55, 50	1.67 @ 20	16 h
Ir/MoS_2 nanosheets[92]	Hydrothermal	1 M KOH	HER/10, OER/10	44, 330	32, 44	1.57	12 h
Co–MoS_2 nanosheets[69]	Hydrothermal	1 M KOH	HER/10, OER/10	90, 190	50.3, 64.7	1.58	—
		0.5 M H_2SO_4	HER/10, OER/10	60, 540	64.7, 245.9	1.90	~11 h

4.2 Bifunctional non-layered TMS (M_xS_y: Fe, Co, Ni, *etc.*) electrocatalysts

Non-layered TMS electrocatalysts are the most extensively studied bifunctional electrocatalysts for overall water splitting and they include FeS_2, Ni_3S_2, and CoS_2. Composed of first-row transition metals and S elements, these kinds of materials are very widely available, inexpensive, and chemically stable, making them quite valuable for energy conversion applications.[80] Such bifunctional electrocatalysts based on Fe, Co, and Ni have been widely reported, frequently with similar or, in some cases, even better activities for both the HER and OER compared with electrocatalysts based on noble metals (like Pt, Ir, and Ru). To further improve their electrocatalytic performances for overall water splitting, many strategies have been developed, such as synergetic composite designing, heteroatom doing, strain engineering, facet engineering, edge engineering, and defect engineering.

4.2.1 Intrinsic bifunctional electrocatalysts. Ni-based sulfides are highly efficient non-noble metal-based bifunctional electrocatalysts with high conductivity and unique configurations, including Ni_3S_2, Ni_3S_4, and NiS.[109] The controllable preparation of NiS_x compounds with different phases and compositions can be easily realized *via* adjusting the added precursor ratios. Shi *et al.* prepared three NiS_x compounds with large surface areas *via* a hydrothermal method, namely hexagonal NiS and cubic Ni_3S_4 and NiS_2.[110] Upon increasing the S/Ni molar ratio in the final product, the particle size decreases and the surface of the NiS_x compound becomes rougher. A pyrite-type NiS_2 electrocatalyst with enriched Ni^{3+} sites on the surface exhibited the best electrocatalytic activity, which was characterized by low overpotentials of 241 and 147 mV at 10 mA cm^{-2} for the OER and HER, respectively, in 1.0 M KOH. In practice, the enhanced performance could be attributed to the high-valence-state Ni^{3+} sites, which could optimize the binding energies with H* and OH* species, reduce the reaction barriers, and consequently speed up the sluggish kinetics. Similarly, Zheng *et al.* synthesized a series of NiS_x nanocrystals with controllable phases and compositions *via* a facile polyol solution process, namely NiS, Ni_3S_2, and NiS_2.[111] Ni_3S_2 exhibited superior OER and HER activities compared to NiS and NiS_2 in alkaline media, requiring overpotentials of 295 mV and 112 mV to afford 10 mA cm^{-2} for the OER and HER, respectively. The higher proportion of Ni in Ni_3S_2 leads to intrinsic metallic conductivity, abundant active sites, and optimized ΔG_H values for the HER, additionally generating more active NiOOH species on the surface of Ni_3S_2 for the OER.

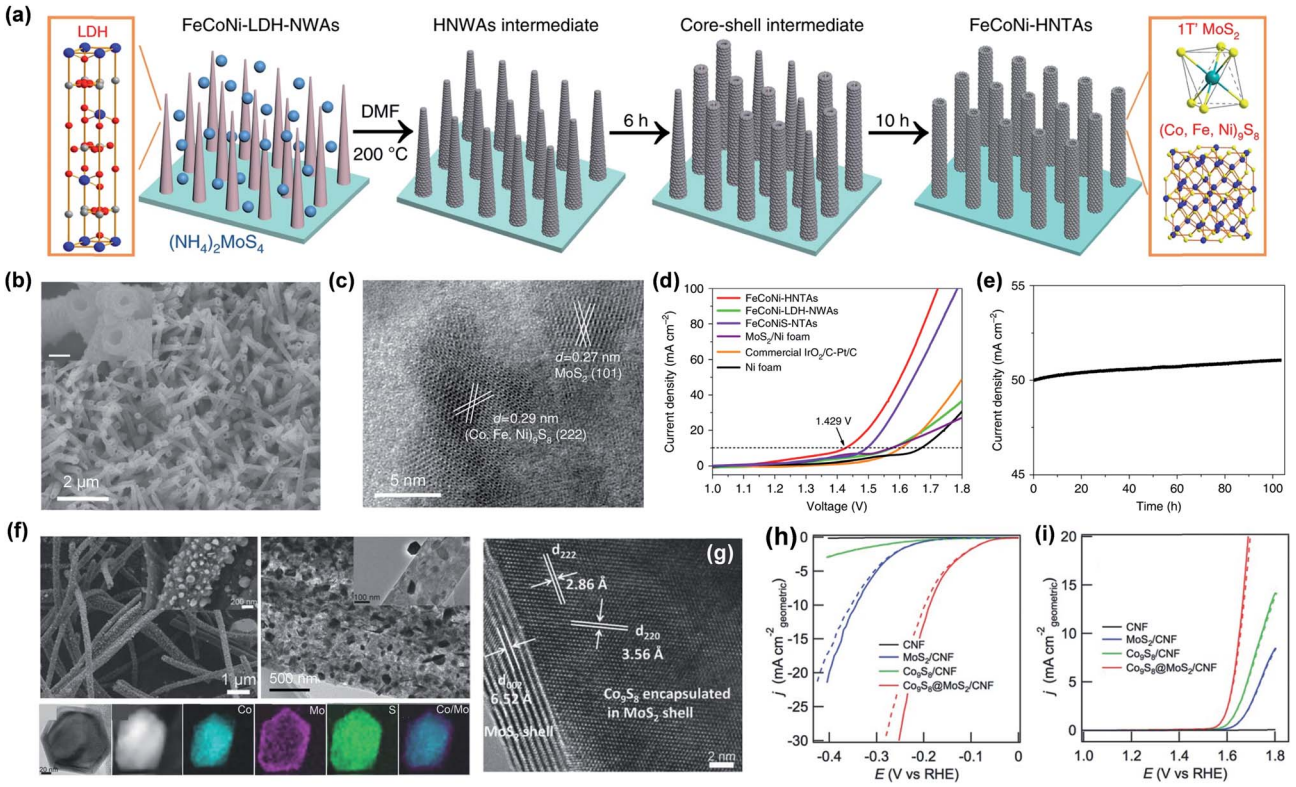

Fig. 14 (a) Schematic diagrams of the preparation process of FeCoNi-HNTAs. (b) An FESEM image and (c) HRTEM image of the as-prepared FeCoNi-HNTAs. (d) Polarization curves and (e) the chronoamperometric response of FeCoNi-HNTAs in 1 M KOH with a typical two-electrode set-up.[118] (f) FESEM, TEM, STEM, and STEM-EDS element mapping images of a Co_9S_8@MoS_2 nanocrystal. (g) A HRTEM image of the Co_9S_8@MoS_2 nanocrystal. Polarization curves of Co_9S_8@MoS_2/CNFs, MoS_2/CNFs, Co_9S_8/CNFs, and CNFs for (h) the HER in 0.5 M H_2SO_4 and (i) the OER in 1 M KOH.[120]

Obviously, Ni_3S_2 shows superior electrocatalytic performance owing to the high Ni element content, which could bring about intrinsic metallic behavior and a continuous network of Ni–Ni bonds throughout its whole structure. Zeng *et al.* reported 3D hierarchical Ni_3S_2 superstructures grown *in situ* on Ni foam *via* a chemical etching method.[112] The porous rod-like array structure of Ni_3S_2 could provide large active surface areas, porosity, and highly effective accessibility. This desirable self-supported electrode offered ~100% Faradaic yields for both the HER and OER, and it exhibited remarkable electrocatalytic stability for more than 50 h in 1.0 M KOH. Coincidentally, Zhang *et al.* fabricated 3D coral-like Ni_3S_2 on Ni foam (Ni_3S_2/NF) *via* a one-step electrochemical method.[113] The optimal Ni_3S_2/NF electrode exhibited high electrocatalytic activity for overall water splitting, with low overpotentials of 89 and 242 mV for the HER and OER, respectively, to afford 10 mA cm^{-2}. When the as-prepared Ni_3S_2/NF electrodes were assembled in an electrolyzer, a low cell voltage of 1.577 V was required to get 10 mA cm^{-2}, with extremely long-term durability.

Ni-based sulfides can use commercial Ni foam directly as both a raw material and a growth template; the *in situ* growth of active Ni-based sulfides on Ni foam could further result in a self-supporting electrode for overall water splitting. Zhu *et al.* reported NiS microsphere film grown *in situ* on Ni foam (NiS/NF) *via* a vapor sulfurization reaction.[114] This NiS/NF electrode could deliver 20 mA cm^{-2} with an overpotential of 158 mV for the HER and 50 mA cm^{-2} with an overpotential of 335 mV for the OER in 1.0 M KOH, exhibiting superior electrocatalytic activity and durability. The *in situ* strongly coupled interactions between NiS and Ni contributed to the enhanced electron interactions and lowered charge transfer barrier at the interface, which were beneficial for efficient electrocatalytic reactions. In fact, the interface between active Ni-based sulfides and Ni foam played a key role in generating their excellent electrocatalytic performance because a rational interface could create new electrochemically active sites *via* inducing unsaturated bonding, lattice distortion, and interfacial polarization.

Co-based sulfides also exhibit different phases and compositions, which can greatly affect the electrocatalytic activity and stability toward overall water splitting, with examples such as Co_9S_8, Co_3S_4, and CoS_2. Ma *et al.* synthesized Co_9S_8, Co_3S_4, and CoS_2 hollow nanospheres *via* adjusting the molar ratios of S and Co precursors using a facile solution-based strategy.[115] The as-prepared CoS_2 with a Co-rich component was superior to Co_9S_8 and Co_3S_4 in 1.0 M KOH, exhibiting overpotentials of 193 mV for the HER and 290 mV for the OER at 10 mA cm^{-2}, and respective Tafel slopes of 57 and 100 mV dec^{-1}. The electrocatalytic activities of these binary CoS_x species were determined based on the coordination environments of Co^{n+} active sites, the surface morphology, and the crystallographic structure. As is

commonly known, metal atoms of transitional metal sulfides play important roles in determining electrocatalytic performance. Simultaneously, sulfur vacancies are also crucial in electrocatalytic processes. Water adsorption and dissociation on the low-index (100) facets of Co_9S_8 and Co_3S_4 have been investigated *via* a DFT approach.[116] The sulfur vacancies on the (100) facet of Co_9S_8 enhanced the electrocatalytic activity toward water dissociation *via* elevating the energy level of unhybridized Co 3d states to the Fermi level, while having no significant impact on the energetics of the Co_3S_4 (100) facet.

Fe-based sulfides are emerging as a new generation of earth-abundant, low-cost, and highly active alternatives for water electrolysis. However, research into the OER performance of FeS_2 is undertaken much less frequently than research into the HER electrocatalytic activity.[38,81] Li *et al.* prepared FeS_2/C nanoparticles on Ni foam *via* a facile hydrothermal strategy.[117] These FeS_2/C nanoparticles had excellent electrocatalytic activity, long-term durability, and fast charge-transfer kinetics, and they could deliver 10 mA cm^{-2} at overpotentials of 240 and 202 mV for the OER and HER, respectively.

4.2.2 Strategies for enhancing the electrocatalytic performance of non-layered TMS. Various inventive strategies have been developed for optimizing and improving the electrocatalytic performances of non-layered TMS *via* increasing the number of active sites and enhancing the intrinsic activity and electrical conductivity. Typically, synergetic composite designing, strain engineering, and heteroatom doping can significantly enhance the charge transfer kinetics during water electrolysis. Facet engineering, edge engineering, and defect engineering can improve the intrinsic electrocatalytic activities of non-layered TMS *via* exposing more active facets or creating more accessible active sites. In practice, these strategies are not mutually independent and sometimes can be applied simultaneously.

Designing composites is a conventional method for enhancing the charge transfer kinetics and creating new active sites; this can lead to a synergetic effect from each component and trigger the creation of additional interfaces and defects. Active species, like metal-based sulfides, oxides, and carbides, and carbon-based materials, all can be coupled with non-layered TMS to enhance bifunctional electrocatalytic activities. Li *et al.* reported complex polymetallic sulfide systems based on 1T′-MoS_2 and (Co, Fe, Ni)$_9S_8$ as highly active bifunctional nanotube-array electrodes for water splitting, which were denoted as FeCoNi-HNTAs.[118] The preparation process and microstructures of FeCoNi-HNTAs are shown in Fig. 14a–c. The electrode only required low overpotentials of 58 and 184 mV at 10 mA cm^{-2} for the HER and OER respectively, while maintaining good long-term stability. Further, when the electrodes were assembled into an electrolyzer, 10 mA cm^{-2} could be delivered at a low cell voltage of 1.429 V and excellent durability was exhibited (Fig. 14d and e). The outstanding electrocatalytic performance was principally thanks to the systematic optimization of the chemical composition and geometric structure. Abundant active sites, the excellent conductivity of metallic 1T′-MoS_2, the synergistic effect of Fe, Co, and Ni ions, and the superaerophobicity of the electrode surface all contributed to the prominent electrocatalytic performance.

The interfaces between non-layered TMS and other materials in composites can bring about the proliferation of active sites. Li *et al.* constructed FeS_2/CoS_2 nanosheets with abundant defects at their interfaces as efficient bifunctional electrocatalysts.[119] Benefiting from the disordered nanosheet interface structure with rich defects, FeS_2/CoS_2 nanosheets showed excellent electrocatalytic performance, with low overpotentials of 78.2 mV at 10 mA cm^{-2} for the HER and 302 mV at 100 mA cm^{-2} for the OER in 1.0 M KOH. More importantly, the FeS_2/CoS_2 nanosheets displayed remarkable performance for overall

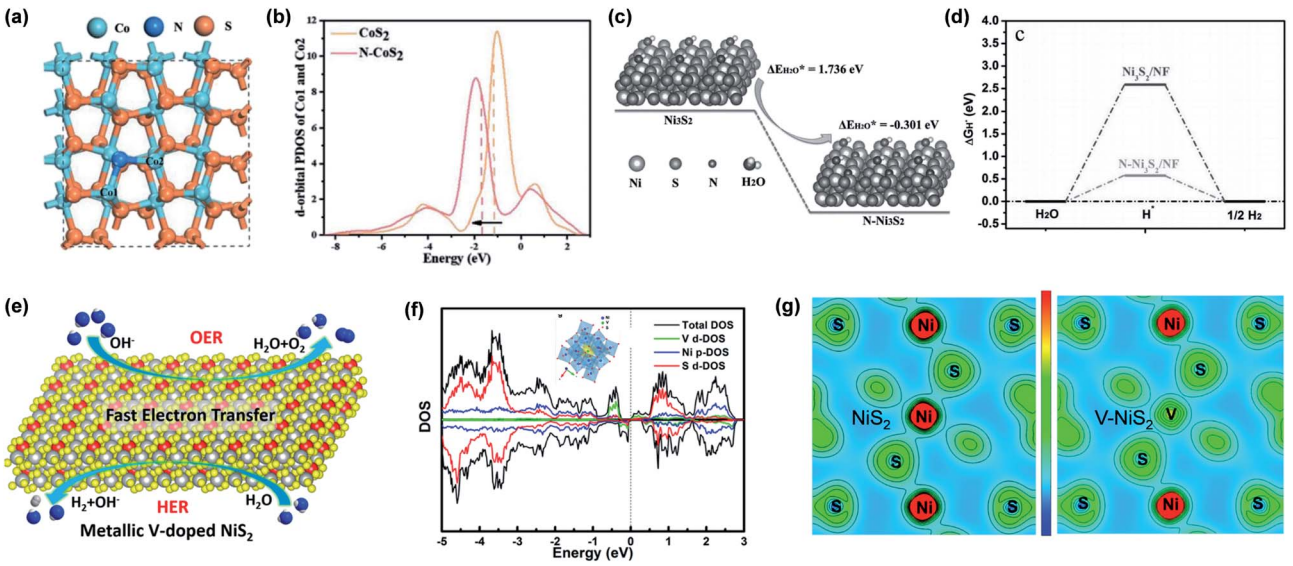

Fig. 15 (a) A top view of the optimized N-CoS_2 (001) structure and (b) the d-orbital partial density of states of Co1 and Co2 from the areas labeled in (a).[133] (c) The calculated water adsorption energy and (d) the HER free-energy change for N-Ni_3S_2 and pristine Ni_3S_2.[135] (e) A schematic diagram of overall water splitting with V-NiS_2 (with 10% V molar doping). (f) The calculated DOS of V-NiS_2. (g) Charge-density contour maps of NiS_2 and V-NiS_2.[134]

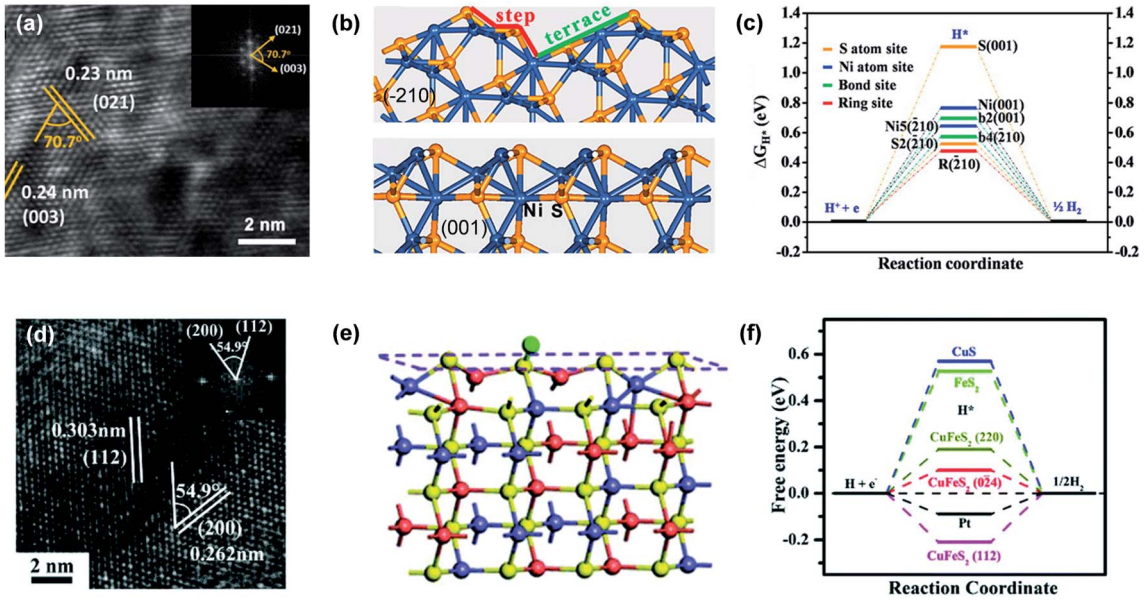

Fig. 16 (a) HRTEM and fast Fourier transform images of Ni_3S_2. (b) The most stable terminations of the (−210) and (001) surfaces of Ni_3S_2; the yellow and blue spheres represent S and Ni atoms, respectively. (c) A calculated free-energy diagram for the HER on the (−210) and (001) surfaces of Ni_3S_2 at equilibrium potential.[142] (d) A HRTEM image of $CuFeS_2$ nanosheets. (e) A chemisorption model of H on the (0−24) facet of $CuFeS_2$ nanosheets; the brown, yellow, blue, and green spheres represent Cu, S, Fe, and H atoms, respectively. (f) A calculated free energy diagram for the HER using different materials.[143]

water splitting with a cell voltage of 1.47 V required to achieve 10 mA cm^{-2}, and this activity could be maintained for more than 21 h. Zhu *et al.* designed and synthesized a hybrid system involving a cubic Co_9S_8@MoS_2 core–shell structure on carbon nanofibers for overall water splitting, as shown in Fig. 14f–i.[120] The Co_9S_8 nanoparticle core was surrounded by a shell of fullerene-like MoS_2 layers to form a unique Co_9S_8@MoS_2 core–shell structures on carbon nanofibers (CNFs) hybrid system.

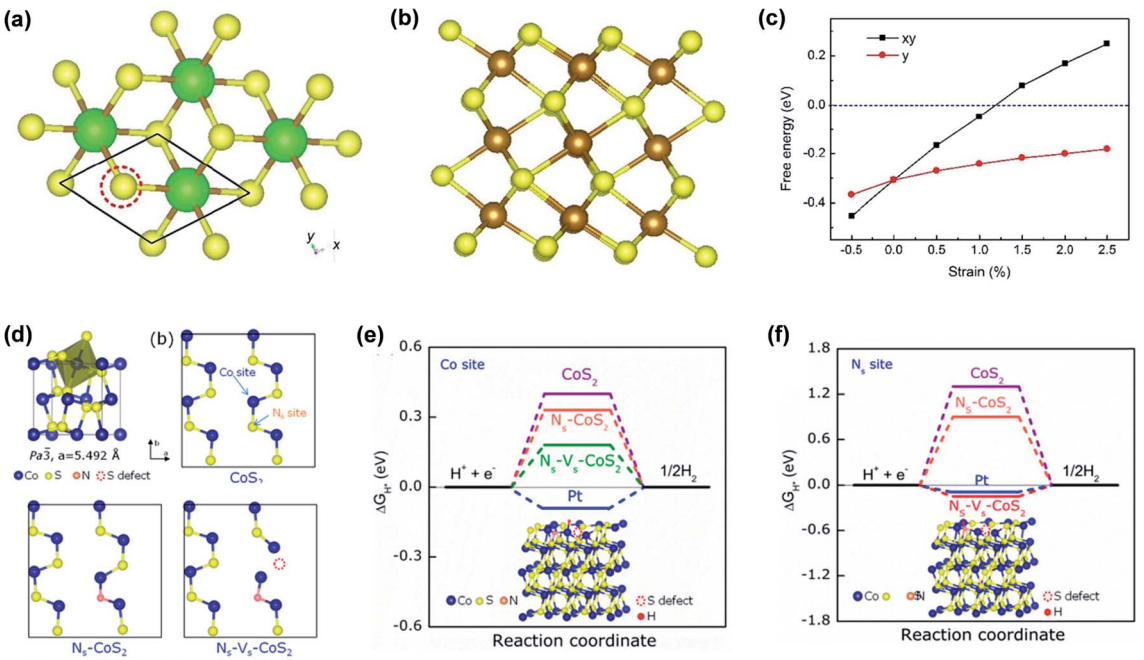

Fig. 17 The charge densities of an optimized (1 × 1) Fe_3S_4 monolayer (a) without external strain and (b) with 1.0% compressed strain. (c) The Gibbs free energy of hydrogen adsorbed on the surface of a Fe_3S_4 monolayer as a function of the external strain.[149] (d) The crystal structure of CoS_2 and models of surface single-layer atoms in CoS_2, N-doped CoS_2 (N_s-CoS_2), and N-doped CoS_2 with a S vacancy (N_s-V_s-CoS_2). (e) The HER free energy diagram for Co sites. (f) The HER free energy diagram for N_s sites.[150]

Table 2 Summary of non-layered TMS-based bifunctional electrocatalysts for overall water splitting

TMS-based materials	Preparation method	Electrolyte	Reaction/J (mA cm^{-2})	Overpotential η (mV)	Tafel slope (mV dec^{-1})	Cell voltage (V @ mA cm^{-2})	Stability
FeS_2/C nanoparticles[117]	Hydrothermal	1 M KOH	HER/10, OER/10	202, 240	98, 92	1.72	5 h
FeS nanosheets[185]	Solvothermal	1 M KOH	HER/100, OER/10	243, 238	77, 82.7	—	50 h
Ni–FeS_2 (ref. 186)	Electrodeposition	1 M KOH	HER/10, OER/100	157, 255	112.5, 58.3	1.588	11 h
Co–FeS_2 nanospheres[187]	Solvothermal	1 M KOH	HER/10, OER/10	267, 324	58, 50	1.60	10 h
NiS_2/FeS_2/N-doped carbon nanorods[188]	Carbonization + solid-phase synthesis	1 M KOH	HER/10, OER/20	172, 231	115.64, 44.29	1.58	80 h
FeS/NiS/Ni foam[189]	Deposition + solvothermal	1 M KOH	HER/10, OER/10	144, 203	120, 39	1.618	10 h
CoS_2 hollow nanospheres[115]	Hydrothermal	1 M KOH	HER/10, OER/10	193, 290	100, 57	1.54	10 h
CoS_2 nanosheets[190]	CVD	1 M KOH	HER/10, OER/10	90, 220	48, 92	1.58	22 h
CoS_2 nanotube arrays[145]	Solid-phase synthesis	1 M KOH	HER/10, OER/10	193, 276	88, 81	1.67	20 h
CoS_x freestanding sheets[191]	Liquid-phase growth	1 M KOH	HER/10, OER/10	127, 288	117, 91	1.55 @ 20	48 h
CoS nanoflake array[192]	Hydrothermal	1 M KOH	HER/50, OER/10	247, 310	114.8, 73.4	1.72	15 h
Co_9S_8 nanosheets[193]	Hydrothermal	0.5 M H_2SO_4, 1 M KOH	HER/10, OER/10	178, 206	82, 87	—	8 h
Co_3S_4 nanosheets[194]	Solvothermal	1 M KOH	HER/10, OER/10	270, 360	124.5, 84.7	1.63	5 h
Co–S films[156]	Electrodeposition	1 M KOH	HER/100, OER/100	124, 322	65.5, 66.4	1.79	150 h
CoS_2/graphite foam[131]	Hydrothermal	1 M KOH	HER/20, OER/20	224, 298	148, 82.6	1.74 @ 20	18 h
Co_3S_4@carbon microflowers[152]	Hydrothermal	1 M KOH	HER/10, OER/10	140, 250	103, 78	1.58	8 h
Mo–Co_9S_8 nanorod array[195]	Hydrothermal	1 M KOH	HER/10, OER/50	139, 210	57, 123	1.50	20 h
Cu–Co_9S_8 nanorod array[196]	Solid-phase synthesis	1 M KOH	HER/10, OER/50	62, 260	76.7, 132.4	1.49	25 h
Cr–Co_9S_8 nanoarrays[197]	Hydrothermal + solid-phase synthesis	1 M KOH	HER/10, OER/100	120, 313	138.8, 10.1	1.45	12 h
Ni–Co_9S_8 nanoarrays[198]	Hydrothermal + solid-phase synthesis	1 M KOH	HER/10, OER/100	90, 300	62.8, 105.1	1.45	15 h
Ni–Co_3S_4 nanowires[199]	Hydrothermal	1 M KOH	HER/10, OER/100	199, 283	91, 65	1.70	40 h
F–CoS_2/NF composites[200]	Hydrothermal	1 M KOH	HER/10, OER/100	112, 1596	61, 104	—	100 h
N–CoS_2/Ni foam[133]	Hydrothermal + heating	1 M KOH	HER/10, OER/20	28, 200	42.6, 55	1.50	11 h
P–CoS_2/carbon cloth[201]	Solvothermal	1 M KOH	HER/10, OER/10	80, 250	98, 90	1.56	24 h
$Co_{0.9}S_{0.58}P_{0.42}$ (ref. 202)	Solid-phase synthesis + phosphorization	1 M KOH	HER/10, OER/10	140, 266	78, 48	1.59	30 h
TiO_2@Co_9S_8 core-branch arrays[203]	Solid-phase synthesis	1 M KOH	HER/10, OER/10	139, 240	65, 55	1.56	30 h
P–CoMoS/carbon cloth[204]	Hydrothermal + phosphorization	1 M KOH	HER/10, OER/10	66, 260	60.1, 72.2	1.54	24 h
CoS@few-layer graphene[205]	High-temperature treatment	1 M KOH	HER/10, OER/10	118, 350	63, 70.9	1.77	10 h
CoS_2@N-doped graphene[206]	Hydrothermal	1 M KOH	HER/10, OER/10	204, 243	108, 51.8	1.53	12 h

Table 2 (*Contd.*)

TMS-based materials	Preparation method	Electrolyte	Reaction/J (mA cm^{-2})	Overpotential η (mV)	Tafel slope (mV dec^{-1})	Cell voltage (V @ mA cm^{-2})	Stability
N-, O-, S-tridoped carbon-encapsulated Co_9S_8 (ref. 207)	Pyrolysis	1 M KOH	HER/10, OER/10	320, 340	105, 68	1.60	10 h
Co_9S_8/N,S-rGO[130]	Polyol refluxing + solid-phase synthesis + calcination	1 M KOH	HER/10, OER/10	332.4, 266	131.4, 75.5	—	20 h
S,N-CNTs/CoS_2@Co nanoparticles[208]	Self-catalysis + solid-phase synthesis	1 M KOH	HER/10, OER/10	112, 157	104.9, 76.1	1.633	20 h
Co_9S_8/N,S-doped carbon@Mo_2C[126]	Pyrolysis	0.5 M H_2SO_4	HER/10, OER/10	74, —	69.3, —	—	—
		1.0 M phosphate solution	HER/10, OER/10	121, —	106.4, —	—	—
		1 M KOH	HER/10, OER/10	89, 293	86.7, 59.7	1.61	20 h
Co_9S_8/MnS/Ni foam[209]	Solvothermal	1 M KOH	HER/100, OER/100	217, 298	48.2, 43.9	1.47	20 h
$CoNi_2S_4$@CoS_2/Ni foam[210]	Hydrothermal + solid-phase synthesis	1 M KOH	HER/10, OER/10	173, 259	51, 45	—	16 h
$Co_9S_4P_4$ pentlandite[159]	Etching + CVD	1.0 M PBS	HER/10, OER/25.9	87, 570	51, 106	1.67	24 h
$Zn_{0.3}Co_{2.7}S_3P$ nanoparticles[211]	Solvothermal + phosphorization	1 M KOH	HER/10, OER/10	188, 261	76.1, 56.2	1.70	10 h
$CuCo_2S_4$ nanowire arrays[212]	Hydrothermal	1 M KOH	HER/10, OER/100	65, 310	42, 49	1.65 @ 100	50 h
$CuCo_2S_4$ (ref. 213)	Hydrothermal	1 M KOH	HER/10, OER/20	158, 290	113, —	1.66	24 h
$CuCo_2S_4$@$Ni(OH)_2$ nanorods[214]	Hydrothermal + electrodeposition	1 M KOH	HER/10, OER/100	117, 250	170, 103.4	1.47	20 h
$FeCo_2S_4$ nanosheet arrays[215]	Hydrothermal	1 M KOH	HER/10, OER/50	132, 270	164, 59	1.56	20 h
$FeCo_2S_4$ nanosheet arrays[138]	Hydrothermal + solid-phase synthesis	1 M KOH	HER/10, OER/20	131, 259	52, 173	1.541	12 h
Fe–Co–S nanosheets[216]	Hydrothermal	1 M KOH	HER/10, OER/10	68, 208	114, 37	1.44	80 h
$NiCo_2S_4$ nanowire array[217]	Wet-chemistry solid-phase synthesis	1 M KOH	HER/50, OER/50	266, 300	130.5, 90.9	1.66	20 h
$NiCo_2S_4$ nanowire arrays[137]	Hydrothermal	1 M KOH	HER/10, OER/10	210, 260	58.9, 40.1	1.63	50 h
$NiCo_2S_4$ nanoflakes[218]	Reverse microemulsion + solid-phase synthesis	1 M KOH	HER/10, OER/100	169, 319	97.1, 53.3	1.61	70 h
$NiCo_2S_4$ nanowires[219]	Hydrothermal	1 M KOH	HER/10, OER/40	191, 256	116.9, 67.7	1.59	12 h
$Ni_{4.3}Co_{4.7}S_8$ (ref. 220)	Hydrothermal	1 M KOH	HER/10, OER/20	148, 133.8	90, 194.2	1.67 @ 50	—
$(Ni_{0.33}Co_{0.67})S_2$ nanowires/carbon cloth[221]	Hydrothermal	1 M KOH	HER/100, OER/100	334, 216	127, 78	1.57	30 h
Ni–Mo–S nanowires[222]	Electroplating + solid-phase synthesis	1 M KOH	HER/100, OER/100	290, 390	103, 75	2 @ 100	12 h
NiFeMoS nanorods[223]	Electrodeposition + hydrothermal	1 M KOH	HER/10, OER/150	100, 280	121, 69	1.52 @ 100	10 h
$Ni_8V_2(Mo_3S_4)_{11}$/Ni–Co foam[224]	Hydrothermal	1 M KOH	HER/10, OER/10	129, 330	136, 183	—	25 h
NiCo/$NiCo_2S_4$@NiCo arrays[225]	Hydrothermal + electrodeposition	1 M KOH	HER/10, OER/100	132, 294	58.2, 59.6	1.55	27 h
$FeCo_2S_4$–$NiCo_2S_4$ nanosheet arrays[140]	Hydrothermal	1 M KOH	HER/10, OER/10	150, 230	38, 65	1.51	10 h
Cu@CoS_x/copper foam[226]	Chemical deposition	1 M KOH	HER/10, OER/10	134, 160	61, —	1.50	200 h
Ni–Fe–Co–S nanosheets[227]	Electrodeposition	1 M KOH	HER/10, OER/10	106, 207	95, 63	1.54	10 h
Ni–Co–S nanosheet arrays[228]	Annealing + solid-phase synthesis	1 M KOH	HER/10, OER/10	110, 270	56, 80	1.62	12 h

Table 2 (*Contd.*)

TMS-based materials	Preparation method	Electrolyte	Reaction/J (mA cm^{-2})	Overpotential η (mV)	Tafel slope (mV dec^{-1})	Cell voltage (V @ mA cm^{-2})	Stability
P–(Ni, Fe)$_3S_2$ nanosheet arrays[229]	Phosphorization + solid-phase synthesis	1 M KOH	HER/10, OER/10	98, 196	88, 30	1.54	15 h
(Ni–Fe)S_x/NiFe(OH)$_y$ hollow microtubes/spheres[230]	Electrodeposition	1 M KOH	HER/100, OER/100	124, 290	68, 58	1.46	50 h
Co(OH)$_2$/Ni–Co–S nanotube arrays[231]	Hydrothermal	1 M KOH	HER/100, OER/100	254, 340	88, 64	1.62	20 h
Co_9S_8/Ni_3Se_2/graphene[232]	Hydrothermal + solvothermal	1 M KOH	HER/20, OER/10	170, —	83, —	1.62	10 h
Ni–Mo–S@Co_3O_4/carbon fibers[233]	Hydrothermal	1 M KOH	HER/10, OER/10	85, 275	50, 109	1.57	50 h
N-carbon coated $NiCo_2S_4$ hollow nanotubes[234]	Solvothermal	1 M KOH	HER/100, OER/100	295, 330	89.8, 86.8	1.60	15 h
rGO/($Ni_xMn_yCo_z$)$_3S_4$ nanocomposites[235]	Solid-phase synthesis	1 M KOH	HER/10, OER/10	151, 320	52, 58	1.56 @ 20	24 h
Nanoporous (003)-Ni_3S_2 (ref. 50)	Anodization + solid-phase synthesis	1 M NaOH	HER/10, OER/10	135, 175	75.7, 101.2	1.611	30 h
(−210)-Ni_3S_2 nanosheet arrays[142]	Solid-phase synthesis	1 M KOH	HER/10, OER/10	223, 260	—, —	—	200 h
NiS microsphere film[114]	Solid-phase synthesis	1 M KOH	HER/20, OER/50	158, 335	83, 89	1.64	35 h
Ni_3S_2 superstructures[112]	Chemical etching	1 M KOH	HER/10, OER/100	135, 320	75, 59	1.59	50 h
Ni_3S_2 nanocrystals[111]	Ambient-pressure polyol solution	1 M KOH	HER/10, OER/10	112, 295	67, 52	1.63	108 h
Ni_3S_2 nanorods[236]	Hydrothermal	1 M KOH	HER/10, OER/10	82, 310	73.8, 80.1	1.61	30 h
Ni_3S_2 superstructures/Ni foam[237]	Chemical etching	1 M KOH	HER/10, OER/10	182, 340	89, 150	—	12 h
Ni_3S_2/Ni foam[238]	Annealing	1 M KOH	HER/10, OER/10	131, 312	96, 111	1.68	14 h
Coral-like Ni_3S_2/Ni foam[113]	Electrodeposition	1 M KOH	HER/10, OER/10	89, 242	85, 74	1.577	40 h
Ni_3S_2/Ni foam[239]	Solvothermal	1 M KOH	HER/10, OER/10	123, 222	91, 60	1.59	20 h
NiS_2 nanospheres[110]	Hydrothermal	1 M KOH	HER/10, OER/10	147, 241	105, 65	1.66	40 h
NiS_2 nanowires/carbon fiber paper[240]	Solid-phase synthesis	1 M KOH	HER/10, OER/10	165, 246	134, 94.5	1.59	20 h
NiS_2 microspheres and NiS microspheres[67]	Hydrothermal + annealing	1 M KOH	HER/10, OER/10	148, 320	79, 59	1.58	12 h
Ni_7S_6 foam[241]	Annealing	0.5 M H_2SO_4, 0.1 M KOH	HER/10, OER/10	70, 140	63, 119	—, 1.51	24 h
NiS/Ni coupled interface[146]	Solid-phase synthesis	1 M KOH	HER/10, OER/10	161, 301	74, 46	—	18.6 h
Ni/NiS/N-doped mesoporous carbon[242]	Solid-phase synthesis	1 M KOH	HER/10, OER/10	70, 337	45, 52	1.61	25 h
Ni($S_{0.5}Se_{0.5}$)$_2$ hollow/porous spheres[243]	Hydrothermal + selenization	1 M PBS	HER/10, OER/100	124, 501	81, 94	1.87	12 h
N–Ni_3S_2 (ref. 135)	Annealing	1 M KOH	HER/10, OER/100	110, 330	—, 70	1.48	8 h
Sn–Ni_3S_2 nanosheets[244]	Hydrothermal	1 M KOH	HER/100, OER/100	170, 270	55.6, 52.7	1.46	60 h
Mo–Ni_3S_2 nanorods[153]	Hydrothermal	1 M KOH	HER/100, OER/100	278, 180	72.9, 45.5	1.53	15 h
Mo–Ni_3S_2 nanosheets[245]	Hydrothermal	1 M KOH	HER/10, OER/10	212, 260	98, 85	1.67	13 h
Mo–NiS heterostructures[246]	Hydrothermal + solid-phase synthesis	1 M KOH	HER/10, OER/50	147.6, 390	88.1, 185	1.92	18 h
Mo/Mn–Ni_xS_y/Ni foam[247]	Hydrothermal + solid-phase synthesis	1 M KOH	HER/10, OER/50	144, 162	91, 110	1.49	24 h

Table 2 (*Contd.*)

TMS-based materials	Preparation method	Electrolyte	Reaction/J (mA cm^{-2})	Overpotential η (mV)	Tafel slope (mV dec^{-1})	Cell voltage (V @ mA cm^{-2})	Stability
$Ni_{0.7}Fe_{0.3}S_2$ microflowers[139]	Hydrothermal	1 M KOH	HER/10, OER/10	155, 198	109, 56	1.625	14 h
Fe-Ni_3S_2 nanowires[248]	Solvothermal	1 M KOH	HER/10, OER/200	109, 223	49.5, 55.7	1.53	14 h
Fe-Ni_3S_2 nanosheet arrays[8]	Hydrothermal + ion exchange	1 M KOH	HER/10, OER/10	47, 214	95, 42	1.54	10 h
$Fe_{11.1\%}$-Ni_3S_2/Ni foam[249]	Hydrothermal + wet-chemistry conversion	1 M KOH	HER/50, OER/100	203, 252	89, 61.7	1.60	42 h
Co–Ni_3S_2 nanoarrays[250]	Hydrothermal	1 M KOH	HER/10, OER/10	240, 120	145, 38.4	1.69 @ 50	10 h
V–NiS_2 nanosheets[134]	Solid-phase synthesis	1 M KOH	HER/10, OER/10	110, 290	90, 45	1.56	20 h
V–Ni_3S_2 nanorod array[251]	Hydrothermal	1 M KOH	HER/10, OER/10	133, 148	70, 42	1.421	60 h
V–Ni_3S_2@NiO/Ni foam[252]	Hydrothermal	1 M KOH	HER/10, OER/10	112, 170	69, 98.8	1.52	55 h
(−210)-Ni_3S_2 branch arrays[253]	Solid-phase synthesis	1 M KOH	HER/10, OER/10	112, 220	69, —	1.58	10 h
MoO_x/Ni_3S_2 microspheres[125]	Solid-phase synthesis + hydrothermal	1 M KOH	HER/10, OER/10	106, 136	90, 50	1.45	200 h
Ni_3S_2/VO_2 core/shell nanoarray[254]	Hydrothermal	1 M KOH	HER/10, OER/10	100, 150	114, 47	1.42	15 h
Ni_3N/Ni_3S_2 (ref. 255)	Calcination	1 M KOH	HER/100, OER/100	197, 404	58.8, 112	—	12 h
Ni_3S_2/MnS nanosheets[256]	Hydrothermal	1 M KOH	HER/10, OER/10	116, 228	41, 46	1.54	50 h
Se–MnS/NiS heterojunctions[257]	Hydrothermal chemical-deposition	1 M KOH	HER/10, OER/10	56, 211	55, 50	1.47	48 h
CdS/Ni_3S_2 nanosheet flowers[258]	Hydrothermal	1 M KOH	HER/10, OER/10	121, 151	110, 174	—	12 h
$Ni_xCo_{3-x}S_4$/Ni_3S_2/Ni foam[259]	Cation exchange	1 M KOH	HER/10, OER/10	136, 160	107, 95	1.53	200 h
$CoMoS_4$/Ni_3S_2 nanostructures[158]	Hydrothermal + solid-phase synthesis	1 M KOH	HER/10, OER/10	158, 200	169, 63	1.568	10 h
N-$NiMoO_4$/NiS_2 nanowires/nanosheets[260]	Solid-phase synthesis	1 M KOH	HER/10, OER/10	99, 283	74.2, 44.3	1.60	20 h
Carbon dots/$NiCo_2S_4$/Ni_3S_2 (ref. 157)	Hydrothermal + cation exchange	1 M KOH	HER/10, OER/10	127, 116	148, 99	1.50	12 h
$Mo_{(1-x)}W_xS_2$/Ni_3S_2 heterostructures[261]	Hydrothermal	1 M KOH	HER/10, OER/10	98, 285	92, 98	1.62	50 h
NiS–CoS nanorod arrays[262]	Electrodeposition + hydrothermal	1 M KOH	HER/10, OER/10	102, 170	92, 71	1.47	12 h
NiS_2/CoS_2 microstructures[122]	Solid-phase synthesis	1 M KOH	HER/10, OER/20	165, 310	72, 78	1.61	24 h
Co_9S_8/Ni_3S_2 nanowire arrays[263]	Hydrothermal + vulcanization	1 M KOH	HER/10, OER/10	128, 227	97.6, 46.5	1.64	9 h
Co_9S_8@$Ni(OH)_2$ nanorods[264]	Hydrothermal + electrodeposition	1 M KOH	HER/10, OER/60	100, 250	143.5, 273.4	1.55	10 h
CoS_x/Ni_3S_2 heterostructures[265]	Hydrothermal	1 M KOH	HER/10, OER/20	204, 280	113.1, 92.7	1.572	30 h
Ni_3S_2/Co_9S_8 arrays[121]	Solid-phase synthesis	1 M KOH	HER/100, OER/100	269, 340	98, 66	1.55	12 h
CoS/Ni_3S_2–FeS nanopetals[266]	Electrodeposition + solid-phase synthesis	1 M KOH	HER/10, OER/10	75, 136	57, 51	—	24 h
FeS_2/CoS_2 interface nanosheets[119]	Hydrothermal + solid-phase synthesis	1 M KOH	HER/10, OER/100	78.2, 302	44, 42	1.47	21 h
Cu_2S–Ni_3S_2 array[267]	Hydrothermal	1 M KOH	HER/10, OER/10	149, 329	75.89, 44.11	1.77	100 h

Table 2 (*Contd.*)

TMS-based materials	Preparation method	Electrolyte	Reaction/J (mA cm^{-2})	Overpotential η (mV)	Tafel slope (mV dec^{-1})	Cell voltage (V @ mA cm^{-2})	Stability
Ni_3S_2/VS_4 nanohorn array[268]	Solvothermal	1 M KOH	HER/10, OER/50	177, 317	139, 43	1.57	70 h
NiS/NiS_2 (ref. 123)	Thermal decomposition	1 M KOH	HER/100, OER/100	248, 416	95.1, 156.5	1.62	36 h
$NiS–NiS_2–Ni_3S_2$/Ni foam[124]	Solid-phase synthesis	1 M KOH	HER/20, OER/20	137, 143	87, 80	1.46	14 h
Mn-doped $Cu_{7.2}S_4@NiS_2@NiS$[269]	Hydrothermal + solid-phase synthesis	1 M KOH	HER/10, OER/50	87, 252	43.7, 130.1	1.514	46 h
Mo–Ni_3S_2/Ni_xP_y hollow nanorods[270]	Solvothermal	1 M KOH	HER/10, OER/50	109, 238	68.4, 60.6	1.46	72 h
Ni_2P/Ni_3S_2 heteronanoflake arrays[271]	Hydrothermal + phosphorization	1 M KOH	HER/10, OER/10	80, 210	65, 62	1.50	36 h
NiS/Ni_2P heterostructures[272]	Hydrothermal + solid-phase synthesis + phosphorization	1 M KOH	HER/20, OER/20	111, 265	78.1, 41.3	1.67	10 h
N-Ni_3S_2/VS_2 nanosheets[273]	Hydrothermal	1 M KOH	HER/10, OER/10	151, 227	107.5, 70.5	1.648	20 h
$Ni(OH)_2/Ni_3S_2$ nanosheet arrays[274]	Co-precipitation + solid-phase synthesis	1 M KOH	HER/20, OER/20	270, 211	129, 152.7	1.57	10 h
$NiS/Ni_2P@Ni(OH)_2$ (ref. 275)	Electrodeposition	1 M KOH	HER/10, OER/10	120, 219	71, 82	1.58	160 h
NiFe-LDH@Ni_3S_2 nanosheet arrays[276]	Hydrothermal	1 M KOH	HER/20, OER/50	197, 230	99, 29	1.65	12 h
Se–$(NiCo)S_x/(OH)_x$ nanosheets[277]	Solvothermal	1 M KOH	HER/10, OER/10	103, 155	87.3, 33.9	1.60	66 h
N-CNTs/$NiS_2@Mo_2C$[127]	Calcination + CVD	1 M KOH	HER/10, OER/10	227, 320	114.6, 77.5	1.52	24 h
Ni_3S_2/N-CNTs[129]	Solid-phase synthesis	1 M KOH	HER/50, OER/50	135, 380	58, 77	1.721 @ 100	50 h
Ni_3S_2@graphite foam@Ni foam[278]	Hydrothermal	1 M KOH	HER/10, OER/10	99, 240	98.2, 62.4	1.63	30 h
N-doped graphene QDs/Ni_3S_2 nanosheets[128]	Hydrothermal	1 M KOH	HER/10 OER/10	218, 216	89, 95.5	1.58	17 h
3D graphene–Au–Ni_3S_2 (ref. 279)	Electrodeposition	1 M KOH	HER/10, OER/91.2	140, 370	93, 148	1.63	19 h

When compared with pure MoS_2/CNFs and Co_9S_8/CNFs nanostructures, the hybrid system exhibited impressive enhanced HER and OER activities, which were attributed to a synergetic effect between Co and Mo in the proposed localized nano-interface region between Co_9S_8 and MoS_2. The nano-interfaces could generate strong electron transfer between Mo and Co through intermediate S atoms bonded to both, which led to the promising improved electrocatalytic activity. Various composites based on non-layered TMS for overall water splitting have been exploited due to the diverse types of these materials, such as Ni_3S_2/Co_9S_8 arrays,[121] NiS_2/CoS_2 nanostructures,[122] interwoven NiS/NiS_2 structures,[123] and multiphase $NiS–NiS_2–Ni_3S_2$.[124]

Metal-based oxides could also be applied as effective enhancers. Wu *et al.* reported ultrathin nanosheet-built, hollow MoO_x/Ni_3S_2 microspheres on Ni foam that possess prominent electrocatalytic activity toward both the OER and HER.[125] The unique structural features of the composite promoted the exposure of high-density electrocatalytically active sites, requiring an impressive low cell voltage of 1.45 V to reach 10 mA cm^{-2} with remarkable durability for more than 100 h in an alkaline electrolyzer. Furthermore, metal-based carbides, such as Mo_2C with good electrical conductivity and a Pt-like d-orbital electronic structure, have been extensively studied for constructing composites with non-layered TMS, for example, porous Co_9S_8/N, S-doped carbon@Mo_2C[126] and a NiS_2/carbon nanotubes@Mo_2C bifunctional electrode.[127]

Carbon materials with different dimensions are another good choice for building composites based on non-layered TMS, like 0D graphene quantum dots, 1D carbon nanotubes, 2D graphene, and 3D graphite foam. Lv *et al.* fabricated nitrogen-doped graphene quantum dots (NGQDs) and Ni_3S_2 nanosheets on Ni foam (Ni_3S_2–NGQDs/NF).[128] Self-supported Ni_3S_2–NGQDs/NF electrodes delivered 10 mA cm^{-2} at overpotentials of 216 and 218 mV for the OER and HER, respectively, and required a low voltage of 1.58 V at 10 mA cm^{-2} in an alkali electrolyzer. The experimental results and theoretical calculations proved that the excellent performance arose from synergistic effects between the constructed active interfaces of Ni_3S_2 and NGQDs; in other words, NGQDs could effectively regulate

the electrocatalytic activity of Ni_3S_2. Analogously, Guo *et al.* synthesized metal sulfide (Ni_3S_2, Co_9S_8, or FeS) foams *via* the *in situ* conversion of corresponding metal (Ni, Co, or Fe) foams, and these then acted as templates for the surface growth of N-doped carbon nanotube (CNT) arrays for fabricating metal sulfide/CNT foam composites.[129] Of these, Ni_3S_2/CNT foam served as the most effective electrode for overall water splitting with voltages of 1.5 and 1.72 V at 10 and 100 mA cm^{-2}, respectively. Ni_3S_2 foam could provide abundant active sites and excellent conductivity; meanwhile, the CNT array coating could supply special superaerophobic geometry and protect the foam from electro-corrosion, indicating that tuning the surface geometry was an efficacious way to promote the electrocatalytic performance. Liu *et al.* grew vertically aligned ultrathin Co_9S_8 nanosheets *in situ* on N and S co-doped reduced graphene oxide (Co_9S_8/N,S-rGO) as an efficient electrocatalyst for water electrolysis.[130] This unique hierarchical architecture was adopted to promote electron transport and fully expose active sites. Co_9S_8/N,S-rGO showed highly efficient and stable electrocatalytic performance for the OER and moderate HER activity in alkaline media, benefitting from a synergetic catalytic effect between Co_9S_8 nanosheets and N,S/rGO. Tong *et al.* prepared self-standing cobalt-disulfide/graphite foam (CoS_2/GF) composite films *via* a hydrothermal approach.[131] This 3D porous CoS_2/GF electrode exhibited ultrahigh electrocatalytic activities for both the HER and OER, delivering a current density of 20 mA cm^{-2} at a cell voltage of 1.74 V in an alkaline electrolyzer. The excellent performances of CoS_2/GF composite films were mainly attributed to the following factors: a strong synergistic effect between CoS_2 and GF; the high electrical conductivity of GF, which could facilitate charge transfer during water electrolysis; the porous inter-layer structure of GF, which could provide effective pathways for releasing H_2 and O_2 bubbles; and the large surface area and numerous active sites of CoS_2/GF composite electrodes.

Heteroatom doping plays a pivotal role in enhancing the electrocatalytic performances of non-layered TMS *via* regulating electronic structures to allow faster electron transfer and to optimize the binding energy of intermediates; strategies include substitutional doping and surface charge transfer doping. The substitutional doping of heteroatoms has attracted widespread attention in recent years, for example, the nitrogen doping of CoS_2 could change the electronic density and minimize the adsorption free energy of materials.[132] Yao *et al.* synthesized nitrogen-doped 3D dandelion-flower-like CoS_2 structures directly grown on Ni foam (N-CoS_2/NF).[133] Benefiting from the unique 3D architecture and optimized hydrogen and water adsorption free energies due to N doping, an N-CoS_2/NF electrode showed remarkable electrocatalytic performance, requiring only a low overpotential of 28 mV to gain 10 mA cm^{-2} for the HER and an overpotential of 200 mV at 20 mA cm^{-2} for the OER in alkaline solution (Fig. 15a and b). In fact, non-noble metal atoms are always applied as dopants due to the merits of high conductivity and low cost. Liu *et al.* reported pyrite NiS_2 nanosheets doped with vanadium heteroatoms, with the conversion of the electronic structure from a typical semiconducting form to one showing metallic characteristics.[134] This interesting electronic structure reconfiguration of NiS_2 was rooted in electron transfer from doped V sites to Ni sites, and it enabled Ni sites to obtain more electrons (Fig. 15e–g). Consequently, the metallic V-doped NiS_2 nanosheets (with 10% V molar doping) displayed outstanding electrocatalytic performance, with overpotentials of 290 and 110 mV for the OER and HER, respectively, at 10 mA cm^{-2} in 1 M KOH.

Ternary and quaternary non-layered TMS with higher conductivity and richer redox reactions always exhibit greatly enhanced electrocatalytic performance, with examples such as Ni–Co–S, Fe–Co–S, and Ni–Fe–S systems.[136] Sivanantham *et al.* directly grew $NiCo_2S_4$ nanowire arrays on the surface of 3D Ni foam ($NiCo_2S_4$ NW/NF) *via* a pressurized hydrothermal method.[137] Benefiting from a high surface area, a well-distributed nanowire array structure, and enhanced charge transport due to the presence of mixed metals, this self-supported $NiCo_2S_4$ NW/NF electrode exhibited superior electrocatalytic performance, with low overpotentials of 260 and 210 mV at 10 mA cm^{-2} for the OER and HER, respectively, in 1 M KOH. Gong *et al.* synthesized $FeCo_2S_4$ nanosheets that were grown *in situ* on Ni foam ($FeCo_2S_4$/NF) using a facile hydrothermal sulfurization method.[138] The self-supported $FeCo_2S_4$/NF electrodes delivered 10 mA cm^{-2}, only requiring a small cell voltage of 1.541 V in a two-electrode alkaline electrolyzer. Furthermore, Yu *et al.* prepared hierarchical porous ternary nickel-iron sulfide ($Ni_{0.7}Fe_{0.3}S_2$) microflowers on Ni foam *via* a traditional two-step method.[139] Owing to the special 3D morphology and strong electron interactions between Ni, Fe, and S atoms, the as-synthesized electrocatalyst exhibited enhanced activity and durability for overall water splitting. The incorporation of Fe not only altered the morphology of sulfides from vertically aligned nanoplates to 3D hierarchical microflowers, but it also tuned the electronic structure of NiS_2 and further optimized the binding energies of reactive intermediates. Furthermore, Li *et al.* reported hierarchical trimetallic sulfide $FeCo_2S_4$–$NiCo_2S_4$ nanosheet arrays supported on Ti mesh as efficient 3D bifunctional electrocatalysts for overall water splitting.[140] This trimetallic sulfide electrode showed superior electrocatalytic performance, with low overpotentials of 230 and 150 mV at 10 mA cm^{-2} for the OER and HER, respectively, which could be attributed to the fully exposed active sites, fast charge transfer, and synergistic effects between multiple components.

Surface charge transfer doping with heteroatoms can be used to modify the electronic structures and morphologies of non-layered TMS simultaneously. Chen *et al.* developed 3D N-anion-decorated Ni_3S_2 on Ni foam (N-Ni_3S_2/NF) prepared *via* a one-step calcination route for both the OER and HER.[135] Remarkably, the as-prepared N-Ni_3S_2/NF electrodes displayed extremely high electrocatalytic activity, long-term stability, and favorable reaction kinetics for both OER and HER processes. Low overpotentials of 330 and 110 mV were needed to reach 100 and 10 mA cm^{-2} for the OER and HER, respectively, in 1.0 M KOH, and a very low cell voltage of 1.48 V was required to deliver a current density of 10 mA cm^{-2} in an overall water-splitting device. The introduction of N anions notably modified the electronic structure and morphology of Ni_3S_2, leading to fully exposed active sites, enhanced electrical conductivity, and

optimized hydrogen and water adsorption energies (Fig. 15c and d). Wang *et al.* synthesized metallic Co_9S_8 decorated with single-atomic Mo as an extremely efficient bifunctional electrocatalyst under various pH conditions.[141] The superior electrocatalytic performance of Mo–Co_9S_8 could be attributed to the following factors: synergistic effects between atomically dispersed Mo and high oxidation state Co led to greatly increased activity and durability; the increased active surface area and superaerophobic interface could facilitate gas release; and the regulation of the electronic structure of Co_9S_8 *via* the immobilization of single-site Mo species on its surface could enhance the electrical conductivity, with a higher density electron cloud and altered binding energies of adsorbed intermediate species.

Facet engineering is a unique method for increasing the intrinsic electrocatalytic activity of non-layered TMS *via* exposing more highly active facets. As is widely known, transition metals in non-layered TMS play a crucial role in determining the electrochemical performance, and they are always responsible for the good electrocatalytic activity. On one hand, transition metal cations on exposed low-index facets usually involve an unsaturated coordination environment, which would possess high electrochemical activity. For example, the low-index (100) facet of FeS_2 is terminated with nonpolar [S–Fe–S] repeated along the regular facet direction, while Fe cations with five-fold coordination are located in a square pyramidal environment, as seen in Fig. 3d.[38]

On the other hand, the electrocatalytic activities of high-index facets with special structures, such as an asymmetric zigzag structure, will be higher than those of low-index facets in non-layered TMS. Feng *et al.* reported that the exposed (−210) high-index facet with an asymmetric zigzag structure in Ni_3S_2 nanosheet arrays contributed to the remarkable catalytic activity, which was much higher than the (001) low-index facet in Ni_3S_2.[142] The as-prepared Ni_3S_2 nanosheet arrays with the (−210) high-index facet were synthesized *via* the direct sulfurization of Ni foam in a hydrothermal system and exhibited efficient and stable electrocatalytic activity toward both the HER and OER. DFT computations also elucidated that the HER and OER activities of the (−210) surface were better than those of the low-index (001) surface (Fig. 16a–c). Similarly, Li *et al.* synthesized ultrathin metallic $CuFeS_2$ nanosheets with abundant exposed high-index (0−24) facets.[143] Theoretical calculations and experimental results confirmed that the $CuFeS_2$ nanosheets with exposed (0−24) high-index facets exhibited excellent electrocatalytic HER activity, benefitting from high electrical conductivity, optimized water adsorption energy, and the fast transformation efficiency of adsorbed H into H_2 (Fig. 16d–f). However, these $CuFeS_2$ nanosheets also have great potential for electrocatalyzing the OER.

In brief, optimizing the density of crystallographic facets with a high fraction of low-coordinated atoms or unique asymmetric zigzag structures could be an effective way to improve the electrocatalytic activities of non-layered TMS. However, facet engineering strongly depends on the synthetic methods used for the controllable exposure of highly active TMS facets.

Edge engineering is a universal route for remarkably improving the electrocatalytic activity of non-layered TMS *via* creating more active sites or increasing their number; it is always presented as a change in structure or morphology. Regular arrangements and the design of unique structures of active materials are conducive to the full exposure of active sites on edges. Zhang *et al.* fabricated 3D hierarchical MoS_2/Ni_3S_2 nanorod arrays that were nearly vertically aligned on Ni foam (MoS_2/Ni_3S_2/NF) *via* a one-step hydrothermal procedure.[144] Thanks to the elaborately designed and well-aligned architecture, the MoS_2/Ni_3S_2/NF electrode with a large surface area and abundant active sites owned excellent electrocatalytic activity and durability for water electrolysis in an alkaline electrolyte. The hierarchical nearly vertically aligned structure possessed enough space for the diffusion of electrolyte into the well-exposed active sites, thus notably increasing the effective electrochemically active surface area of the electrode.

Guan *et al.* prepared self-supported hollow CoS_2 nanotube arrays with hierarchical pores and rich active sites on a flexible substrate, which were derived from uniform wire-like metal–organic framework (MOF) nanoarrays.[145] The open pore space and numerous nanoscale grains of hollow CoS_2 nanotube arrays could provide a large surface area, a high density of active sites, and enhanced gas releasing abilities. The well-defined connection of active CoS_2 with the flexible support ensured high levels of electron transport and good electrode mechanical stability. Consequently, the unique hollow CoS_2 nanotube arrays exhibited high electrochemical activity, with a cell voltage of 1.67 V required to deliver a current density of 10 mA cm^{-2}.

It is worth mentioning that the nanocrystallization of TMS materials is also a simple and promising way to increase the number of active sites *via* edge engineering. Yan *et al.* synthesized mulberry-like NiS/Ni nanoparticles *via* a surface modification strategy.[146] Unique nanostructures of NiS/Ni could provide more active edges sites. Therefore, NiS/Ni nanoparticles exhibited excellent electrocatalytic activity in alkaline solution with remarkably low Tafel slopes of 46 and 74 mV dec^{-1} and small overpotentials of 301 and 161 mV for the OER and HER, respectively. In fact, all the TMS nanostructures mentioned here demonstrated the importance of nanocrystallization.

Strain engineering offers a novel path for promoting the electrocatalytic performance of non-layered TMS for efficient water splitting *via* inducing more active sites.[147] The effects of strain engineering on layered NbS_2 and MoS_2 monolayers have been proved by Chen *et al.*[148] They considered a wide strain range covering both tensile (0–10%) and compressive (0–6%) regions. Biaxial tensile strain enhanced the HER activity of layered TMS monolayers more effectively than uniaxial tensile strain, while compressive strain deteriorated the HER activity. Theoretical calculations revealed that tensile strain could reduce the adiabatic proton affinity but simultaneously increase the adiabatic electron affinity to a larger extent, activate relatively inert inner valence electrons, and further enlarge the d-band exchange splitting, all of which could enhance the electrocatalytic HER activity of layered TMS.

Conceivably, this strategy is also suitable for non-layered TMS. Shan *et al.* predicted strain-induced changes in the

electronic structure and electrocatalytic performance of a 2D Fe_3S_4 material.[149] The calculation results revealed that the half-metallic features of Fe_3S_4 would be converted into metallic features due to the small lattice deformation in Fe_3S_4 monolayers induced by applied external strain, which could optimize the Gibbs adsorption free energy of hydrogen and improve the electron transfer capabilities (Fig. 17a–c). However, more efforts should be carried out to investigate the influence of strain engineering on the OER performance of TMS-based electrocatalysts.

The defect engineering of non-layered TMS is not naturally independent, and it is usually combined with the formation of heterogeneous interfaces,[151] unique architecture design,[152] and heteroatom doping.[153] Defects always have a positive effect on the adsorption activation energy of reactants and the dissociation energy of products in overall water splitting, facilitating the generation and conversion of intermediates *via* regulating the electronic structure.[154] Here, attention is focused on vacancy defects in the lattice structure, which can be induced *via* special techniques such as plasma etching.[85] Theoretical calculations based on first-principles studies revealed the effects of single cobalt and sulfur vacancies on structural and electronic changes *via* making pyrite CoS_2 samples with high densities of defects and inducing localized defect states in the gap range of the minority spin channel.[155] Yang *et al.* developed highly porous Co–S films that were grown *in situ* on Ni foam, which had superior electrocatalytic activity and a robust nature for water electrolysis.[156] Self-supported Co–S film with a S content level of 21.7 at% could drive a high current density of 500 mA cm^{-2} with low overpotentials of 368 and 155 mV for the OER and HER, respectively. The optimal S content in Co–S film could create more vacancy defects, which would give rise to the proliferation of electrocatalytically active sites or oxygen deficiencies during the OER, significantly enhancing the intrinsic activity and reaction kinetics for both the HER and OER. As reported, sulfur vacancies and strain could be used to finely tune the HER electrocatalytic activity of monolayer MoS_2.[41] Similarly, Zhang *et al.* proposed that sulfur vacancies and nitrogen dopants in CoS_2 could synergistically activate and optimize the HER activity *via* enhancing the activities of neighboring Co sites with optimal hydrogen adsorption free energies, as shown in Fig. 17d–f.[150]

All in all, non-layered TMS are the most extensively studied bifunctional electrocatalysts for water electrolysis with the advantages of being highly active, chemically stable, widely available, and cheap. To further improve their bifunctional electrocatalytic performances, many strategies have been proposed for increasing the number of active sites and enhancing the intrinsic activity and electrical conductivity, such as composite design, heteroatom doping, strain engineering, facet engineering, edge engineering, and defect engineering. To now, studies of non-layered TMS bifunctional electrocatalysts have mainly focused on Ni-based and Co-based sulfides. A summary of non-layered TMS-based bifunctional electrocatalysts is shown in Table 2. N-CoS_2/Ni foam requires a quite low overpotential of 28 mV to reach 10 mA cm^{-2} for the HER in 1.0 M KOH, exhibiting the best electrocatalytic HER activity.[133] Moreover, to reach a current density of 10 mA cm^{-2} in the OER, carbon dots/$NiCo_2S_4$/Ni_3S_2 composites require the smallest overpotential of 116 mV in 1.0 M KOH.[157] Surprisingly, these non-layered TMS bifunctional electrocatalysts possess the potential to surpass noble-metal oxides in overall water splitting, showing far-reaching significance for large-scale water electrolysis applications.

5. Conclusions and outlook

In summary, we have outlined the research progress relating to bifunctional electrocatalysts based on transition metal sulfides for effective overall water splitting, showing their potential as candidates to replace noble-metal-based electrocatalysts. The fabrication of TMS electrocatalysts *via* 'bottom-up' and 'top-down' strategies has been summarized. Typically, exfoliation and ball milling approaches are the leading 'top-down' strategy processing methods, which are suitable for synthesizing nano-structured and micro-structured TMS on a large scale from bulk TMS materials. Additionally, hydrothermal, solvothermal, chemical vapor deposition, and solid-phase synthesis approaches are the main representatives of the 'bottom-up' strategy, showing great potential for the preparation of self-supported TMS electrodes when suitable reaction substrates are adopted. *Via* these controlled fabrication approaches, the rational tuning of well-defined TMS shapes, sizes, hierarchical structures, and defect states could be achieved, with great influence on the electronic structure and electrocatalytic performance of TMS. Importantly, the active sites of TMS electrocatalysts are nearly always metal atoms, while exposed S atoms and S vacancies also play a vital direct role in the HER *via* increasing the number of active sites and changing the coordination environments of adjacent metal atoms. Moreover, the indirect role of S atoms in the HER provides locations for hydrogen adhesion and separation when metal atoms act as the active sites. However, TMS tend to function as pre-catalysts in complex OER processes, with involvement in conversion to transition metal hydr(oxy)oxides.

Layered TMS (*e.g.*, MoS_2, WS_2, and TaS_2) exhibit excellent intrinsic electrocatalytic HER activity due to their well-exposed edge sites and good electrical conductivity, while their direct application in the OER is limited. To further explore the potential of layered TMS for use in water splitting, numerous efforts have been carried out to optimize their electrochemical properties *via* improving their intrinsic electrical conductivity and stability and enhancing their chemisorption capabilities for O-containing species. Phase engineering, composite design, and heteroatom doping are favorable strategies for achieving this goal. Phase engineering is a promising way to enhance the electrocatalytic OER activity of layered TMS, as the 1T phase usually exhibits higher OER activity than the 2H phase. Integrating layered TMS with other materials with highly active OER performance or good conductivity can be used to construct bifunctional electrocatalysts with novel composites/heterostructures utilizing synergistic effects relating to the counterparts. Lastly, heteroatom doping is favorable for modulating the electronic structures of layered TMS and

optimizing the chemical-adsorption energies of reactive intermediates during the water splitting reactions, and for creating more active sites *via* generating more defects and distortions in the lattice. Heteroatom doping can be divided into two types, namely substitutional doping and surface charge transfer doping, depending on the interactions between heteroatoms and layered TMS.

Non-layered TMS are the most extensively studied bifunctional electrocatalysts for overall water splitting, with the advantages of being widely available, inexpensive, chemically stable, and highly active, and examples include FeS_2, Ni_3S_2, NiS_2, CoS_2, and Co_3S_4. Many strategies have been researched to improve their bifunctional electrocatalytic performance *via* increasing the number of active sites and enhancing the intrinsic activity and electrical conductivity, *e.g.*, composite designing, heteroatom doping, strain engineering, facet engineering, edge engineering, and defect engineering. Similar to layered TMS, the composite designing of non-layered TMS can enhance the charge transfer kinetics and create new active sites due to synergetic effects between the components and the triggering of additional interfaces and defects. Heteroatom doping also can be used to regulate electronic structures to acquire faster electron transfer and optimize the binding energies of intermediates with non-layered TMS. The development of ternary and quaternary TMS-based materials with excellent redox reversibility and high electronic conductivity has created effective substitutes for noble-metal-based electrocatalysts. Facet engineering is strongly dependent on the synthetic methods used for the controllable exposure of the highly active facets of non-layered TMS, and it is favorable for improving the intrinsic activity. Strain engineering and edge engineering can change the electronic character and induce the creation of more active sites, respectively, and these methods are worth further exploration. Finally, as a universal method for optimizing the electrocatalytic performance of non-layered TMS, defect engineering is not a naturally independent method, and it is usually combined with the formation of heterogeneous interfaces, unique architecture design, and heteroatom doping. In principle, most strategies for enhancing the performance of non-layered TMS are also suitable for use with layered TMS whose OER activities need to be further exploited.

Although a lot of progress has been made related to the development of TMS-based bifunctional electrocatalysts, some challenges still exist, as follows:

(1) The electrocatalytic reaction mechanisms related to these bifunctional electrocatalysts in overall water splitting have still not been fully revealed, and more theoretical study efforts should be devoted to uncovering them and providing strong support for exploiting advanced electrocatalysts. On one hand, the detailed reaction mechanism of the OER requires more investigation to uncover its true intrinsic nature. As a sluggish four electron–proton coupled reaction, the several OH*, O*, and OOH* intermediates formed during the OER make it a great challenge to evolve a consolidated reaction mechanism, and different reaction mechanisms for the OER have been proposed by different research groups.[24] On the other hand, the HER reaction mechanism at the atomic level is still ambiguous at present, and it requires more in-depth investigation. As is known, the HER mechanism in alkaline electrolytes is totally different from that in acidic media, where it only involves hydrogen binding energetics. The HER mechanism in alkaline media is more complex, including the adsorption/dissociation of water molecules, the adsorption/desorption of hydrogen, and even the OH^- poisoning of the electrocatalyst surface. To further explore the reaction mechanisms, advanced *in situ* characterization techniques, such as *in situ* X-ray absorption spectroscopy (XAS), *in situ* Raman spectroscopy, and surface interrogation scanning electrochemical microscopy (SI-SECM), should be widely developed and applied to explore dynamic changes in electronic structures, the dynamic evolution of intermediates, and the binding strengths of adsorbates on the surfaces of electrocatalysts. Nowadays, theoretical calculations based on the first-principles calculations provide powerful support when exploring reaction mechanisms at an atomic level. More importantly, multi-scale modelling approaches involving atomic-level models (such as DFT) and energy minimization techniques (molecular dynamics and Monte Carlo models) could be promising for understanding electrocatalytic processes. Combining theoretical calculations with advanced experimental characterization techniques could provide more in-depth understanding of HER and OER mechanisms.

(2) The development of new or combined approaches for further improving the activity of TMS-based electrocatalysts is essential. The direction of efforts to improve the electrocatalytic activities of TMS-based materials is aimed at increasing the number of active sites, improving the electrical conductivity, and optimizing the absorption energies of reaction intermediates. In this review, several strategies for enhancing the HER and OER performances of TMS-based electrocatalysts have been summarized. The approaches of phase engineering, heteroatom doing, strain engineering, and composite designing are favorable for improving the electron transfer characteristics of materials, and the approaches of edge engineering, facet engineering, and defect engineering are beneficial for increasing the number of exposed active sites. The effects of strain engineering, especially on the OER activities of TMS-based materials, need to be further investigated from a mechanistic perspective and examined through experiments. Utilizing multiple approaches simultaneously to realize a maximized enhancement effect is feasible and effective, for example integrating heteroatom doping and strain engineering together[41] or integrating heteroatom doping and composite design together.[158] In this regard, the synergistic effects of different optimization methods provide a fascinating way to enhance the electrocatalytic activities of TMS-based materials. Examples include preparing highly active heteroatom-doped TMS-based composites with low-dimensional nanostructures *via* coupling composite designing, edge engineering, and heteroatom doping, and designing metallic-phase TMS-based composites with special morphologies *via* coupling composite designing, phase engineering, and edge engineering.

(3) Although enhancements in the activities of TMS-based electrocatalysts are fruitful and activities can even be

comparable with noble-metal-based electrocatalysts, the stabilities of most bifunctional electrocatalysts cannot meet the needs of industrial applications completely, as they suffer from susceptibility to corrosion and the destruction of structures during long-term water electrolysis. Moreover, the large-scale preparation of TMS-based electrodes is also a bottleneck for industrial applications. Hence, robust materials and electrodes that can be manufactured on a large scale need to be further investigated urgently. On one hand, the creation of TMS-based materials decorated with protective or sacrificial materials could be a simple method to improve corrosion and oxidation resistance. On the other hand, the *in situ* growth of active TMS on conductive substrates that could be employed as self-supported electrodes is quite a promising approach for dramatically enhancing durability. Strong interactions between active TMS and substrates could dramatically enhance the electrocatalytic durability and electron transfer during long-term service. *In situ* growth can also avoid the usage of carbon additives and polymer binders, providing more exposed active sites and reducing cost. Broadly speaking, when employing conductive substrates during the preparation process, the 'bottom-up' approaches of hydrothermal, solvothermal, chemical vapor deposition, and solid-phase synthesis all exhibit potential for synthesizing self-supported electrodes on a large scale. In this case, the development of reaction devices capable of the large-scale preparation of TMS-based materials is critical for satisfying industrial application demands. Additionally, advanced preparation methods suitable for the large-scale fabrication of these novel electrocatalysts require more attention and development, such as atomic layer deposition, spray pyrolysis, and pulsed laser deposition.

(4) Currently, reported bifunctional electrocatalysts are mostly employed in alkaline electrolytes, while only a few have been applied in acidic and/or neutral media, as the instability of TMS-based electrocatalysts seriously limits their applications.[159] However, universal-pH bifunctional electrocatalysts with superior activity and durability in near-neutral media are still required, as these would have great significance for the industrial large-scale development of seawater electrolysis. For example, other binary, ternary, or multiple sulfides with precisely defined shapes, sizes, and compositions, including Sb, Sn, Mn, Re, Cu, and Zn metal based examples, deserve more attention. In addition, bifunctional electrocatalysts for overall urea–water electrolysis are highly desired,[160] as they can be applied to efficient H_2 generation and the purification of urea-rich wastewater to meet the requirements of both energy conversion and environmental protection.

All in all, developing bifunctional TMS-based electrocatalysts for overall water splitting is very appealing yet challenging. With continuing research efforts being focused on the strategies mentioned above, it is conceivable that TMS-based bifunctional electrocatalysts with extremely improved activity and long-term stability will be developed for industrial applications.

Conflicts of interest

There are no conflicts to declare.

Acknowledgements

This work was supported by the Basic Science Center Project of the NSFC (51788104) and National Key Research and Development Program of China (2017YFB1104300).

References

1 Z. W. Seh, J. Kibsgaard, C. F. Dickens, I. Chorkendorff, J. K. Norskov and T. F. Jaramillo, Combining theory and experiment in electrocatalysis: insights into materials design, *Science*, 2017, **355**, 4998.

2 S. Chandrasekaran, L. Yao, L. Deng, C. Bowen, Y. Zhang, S. Chen, Z. Lin, F. Peng and P. Zhang, Recent advances in metal sulfides: from controlled fabrication to electrocatalytic, photocatalytic and photoelectrochemical water splitting and beyond, *Chem. Soc. Rev.*, 2019, **48**, 4178–4280.

3 J. W. Joo, T. Kim, J. Lee, S. I. Choi and K. Lee, Morphology-controlled metal sulfides and phosphides for electrochemical water splitting, *Adv. Mater.*, 2019, **37**, 1806682.

4 J. S. Jirkovsky, C. D. Malliakas, P. P. Lopes, N. Danilovic, S. S. Kota, K. C. Chang, B. Genorio, D. Strmcnik, V. R. Stamenkovic, M. G. Kanatzidis and N. M. Markovic, Design of active and stable Co-Mo-S_x chalcogels as pH-universal catalysts for the hydrogen evolution reaction, *Nat. Mater.*, 2016, **15**, 197–203.

5 H. Jin, J. Joo, N. K. Chaudhari, S. I. Choi and K. Lee, Recent progress in bifunctional electrocatalysts for overall water splitting under acidic conditions, *ChemElectroChem*, 2019, **6**, 3244–3253.

6 B. Tang, X. Yang, Z. Kang and L. Feng, Crystallized $RuTe_2$ as unexpected bifunctional catalyst for overall water splitting, *Appl. Catal. B Environ.*, 2020, **278**, 119281.

7 Y. Li, Y. Sun, Y. Qin, W. Zhang, L. Wang, M. Luo, H. Yang and S. Guo, Recent advances on water-splitting electrocatalysis mediated by noble-metal-based nanostructured materials, *Adv. Energy Mater.*, 2020, **10**, 1903120.

8 G. Zhang, Y. S. Feng, W. T. Lu, D. He, C. Y. Wang, Y. K. Li, X. Y. Wang and F. F. Cao, Enhanced catalysis of electrochemical overall water splitting in alkaline media by Fe doping in Ni_3S_2 nanosheet arrays, *ACS Catal.*, 2018, **8**, 5431–5441.

9 J. R. Varcoe, P. Atanassov, D. R. Dekel, A. M. Herring, M. A. Hickner, P. A. Kohl, A. R. Kucernak, W. E. Mustain, K. Nijmeijer, K. Scott, T. Xu and L. Zhuang, Anion-exchange membranes in electrochemical energy systems, *Energy Environ. Sci.*, 2014, **7**, 3135–3191.

10 Z. Kang, H. Guo, J. Wu, X. Sun, Z. Zhang, Q. Liao, S. Zhang, H. Si, P. Wu, L. Wang and Y. Zhang, Engineering an earth-abundant element-based bifunctional electrocatalyst for highly efficient and durable overall water splitting, *Adv. Funct. Mater.*, 2019, **29**, 1807031.

11 J. Wang, X. Yue, Y. Yang, S. Sirisomboonchai, P. Wang, X. Ma, A. Abudula and G. Guan, Earth-abundant

transition-metal-based bifunctional catalysts for overall electrochemical water splitting: a review, *J. Alloys Compd.*, 2020, **819**, 153346.

12 F. Yu, L. Yu, I. K. Mishra, Y. Yu, Z. F. Ren and H. Q. Zhou, Recent developments in earth-abundant and non-noble electrocatalysts for water electrolysis, *Mater. Today Phys.*, 2018, **7**, 121–138.

13 C. Hu, L. Zhang and J. Gong, Recent progress made in the mechanism comprehension and design of electrocatalysts for alkaline water splitting, *Energy Environ. Sci.*, 2019, **12**, 2620–2645.

14 S. Anantharaj, S. R. Ede, K. Sakthikumar, K. Karthick, S. Mishra and S. Kundu, Recent trends and perspectives in electrochemical water splitting with an emphasis on sulfide, selenide, and phosphide catalysts of Fe, Co, and Ni: a review, *ACS Catal.*, 2016, **6**, 8069–8097.

15 Q. Lu, Y. Yu, Q. Ma, B. Chen and H. Zhang, 2D Transition-Metal-Dichalcogenide-Nanosheet-Based Composites for Photocatalytic and Electrocatalytic Hydrogen Evolution Reactions, *Adv. Mater.*, 2016, **28**, 1917–1933.

16 X. Chia, A. Ambrosi, P. Lazar, Z. Sofer and M. Pumera, Electrocatalysis of layered Group 5 metallic transition metal dichalcogenides (MX_2, M = V, Nb, and Ta; X = S, Se, and Te), *J. Mater. Chem. A*, 2016, **4**, 14241–14253.

17 C. Feng, M. B. Faheem, J. Fu, Y. Xiao, C. Li and Y. Li, Fe-Based Electrocatalysts for Oxygen Evolution Reaction: Progress and Perspectives, *ACS Catal.*, 2020, **10**, 4019–4047.

18 W. Zhang, L. Cui and J. Liu, Recent advances in cobalt-based electrocatalysts for hydrogen and oxygen evolution reactions, *J. Alloys Compd.*, 2020, **821**, 153542.

19 Y. N. Guo, T. Park, J. W. Yi, J. Henzie, J. Kim, Z. L. Wang, B. Jiang, Y. Bando, Y. Sugahara, J. Tang and Y. Yamauchi, Nanoarchitectonics for transition-metal-sulfide-based electrocatalysts for water splitting, *Adv. Mater.*, 2019, **31**, 1807134.

20 X. Zou and Y. Zhang, Noble metal-free hydrogen evolution catalysts for water splitting, *Chem. Soc. Rev.*, 2015, **44**, 5148–5180.

21 H. Sun, Z. Yan, F. Liu, W. Xu, F. Cheng and J. Chen, Self-supported transition-metal-based electrocatalysts for hydrogen and oxygen evolution, *Adv. Mater.*, 2019, 1806326.

22 N. Mahmood, Y. Yao, J. W. Zhang, L. Pan, X. Zhang and J. J. Zou, Electrocatalysts for hydrogen evolution in alkaline electrolytes: mechanisms, challenges, and prospective solutions, *Adv. Sci.*, 2018, **5**, 1700464.

23 K. Ojha, S. Saha, P. Dagar and A. K. Ganguli, Nanocatalysts for hydrogen evolution reactions, *Phys. Chem. Chem. Phys.*, 2018, **20**, 6777–6799.

24 N. T. Suen, S. F. Hung, Q. Quan, N. Zhang, Y. J. Xu and H. M. Chen, Electrocatalysis for the oxygen evolution reaction: recent development and future perspectives, *Chem. Soc. Rev.*, 2017, **46**, 337–365.

25 Z. Liu, C. Zhang, H. Liu and L. Feng, Efficient synergism of $NiSe_2$ nanoparticle/NiO nanosheet for energy-relevant water and urea electrocatalysis, *Appl. Catal. B Environ.*, 2020, **276**, 119281.

26 J. Rossmeisl, Z. W. Qu, H. Zhu, G. J. Kroes and J. K. Nørskov, Electrolysis of water on oxide surfaces, *J. Electroanal. Chem.*, 2007, **607**, 83–89.

27 M. Zeng and Y. Li, Recent advances in heterogeneous electrocatalysts for the hydrogen evolution reaction, *J. Mater. Chem. A*, 2015, **3**, 14942–14962.

28 C. C. McCrory, S. Jung, J. C. Peters and T. F. Jaramillo, Benchmarking heterogeneous electrocatalysts for the oxygen evolution reaction, *J. Am. Chem. Soc.*, 2013, **135**, 16977–16987.

29 D. Li, H. Liu and L. Feng, A Review on Advanced FeNi-Based Catalysts for Water Splitting Reaction, *Energy Fuels*, 2020, **34**, 13491–13522.

30 C. C. McCrory, S. Jung, J. C. Peters and T. F. Jaramillo, Benchmarking heterogeneous electrocatalysts for the oxygen evolution reaction, *J. Am. Chem. Soc.*, 2013, **135**, 16977–16987.

31 M. Wang, L. Zhang, M. Huang, Y. Liu, Y. Zhong, J. Pan, Y. Wang and H. Zhu, Morphology-controlled tantalum diselenide structures as self-optimizing hydrogen evolution catalysts, *Energy. Environ. Mater.*, 2019, **3**, 12–18.

32 M. Chhowalla, H. S. Shin, G. Eda, L. J. Li, K. P. Loh and H. Zhang, The chemistry of two-dimensional layered transition metal dichalcogenide nanosheets, *Nat. Chem.*, 2013, **5**, 263–275.

33 A. Ambrosi and M. Pumera, Exfoliation of layered materials using electrochemistry, *Chem. Soc. Rev.*, 2018, **47**, 7213–7224.

34 X. Chia, A. Y. Eng, A. Ambrosi, S. M. Tan and M. Pumera, Electrochemistry of nanostructured layered transition-metal dichalcogenides, *Chem. Rev.*, 2015, **115**, 11941–11966.

35 G. H. Han, D. L. Duong, D. H. Keum, S. J. Yun and Y. H. Lee, van der Waals metallic transition metal dichalcogenides, *Chem. Rev.*, 2018, **118**, 6297–6336.

36 M. A. Lukowski, A. S. Daniel, F. Meng, A. Forticaux, L. Li and S. Jin, Enhanced hydrogen evolution catalysis from chemically exfoliated metallic MoS_2 nanosheets, *J. Am. Chem. Soc.*, 2013, **135**, 10274–10277.

37 A. Ambrosi, Z. Sofer and M. Pumera, 2H-1T phase transition and hydrogen evolution activity of MoS_2, $MoSe_2$, WS_2 and WSe_2 strongly depends on the MX_2 composition, *Chem. Commun.*, 2015, **51**, 8450–8453.

38 D. Kong, J. J. Cha, H. Wang, H. R. Lee and Y. Cui, First-row transition metal dichalcogenide catalysts for hydrogen evolution reaction, *Energy Environ. Sci.*, 2013, **6**, 3553–3558.

39 C. R. Zhu, D. Gao, J. Ding, D. Chao and J. Wang, TMD-based highly efficient electrocatalysts developed by combined computational and experimental approaches, *Chem. Soc. Rev.*, 2018, **47**, 4332–4356.

40 T. H. M. Lau, S. Wu, R. Kato, T. S. Wu, J. Kulhavý, J. Mo, J. Zheng, J. S. Foord, Y. L. Soo, K. Suenaga, M. T. Darby and S. C. E. Tsang, Engineering monolayer 1T-MoS_2 into a bifunctional electrocatalyst via sonochemical doping of isolated transition metal atoms, *ACS Catal.*, 2019, **9**, 7527–7534.

41 H. Li, C. Tsai, A. L. Koh, L. Cai, A. W. Contryman, A. H. Fragapane, J. Zhao, H. S. Han, H. C. Manoharan,

F. A. Pedersen, J. K. Norskov and X. Zheng, Activating and optimizing MoS_2 basal planes for hydrogen evolution through the formation of strained sulphur vacancies, *Nat. Mater.*, 2016, **15**, 364.

42 J. Xie, J. Zhang, S. Li, F. Grote, X. Zhang, H. Zhang, R. Wang, Y. Lei, B. Pan and Y. Xie, Controllable disorder engineering in oxygen-incorporated MoS_2 ultrathin nanosheets for efficient hydrogen evolution, *J. Am. Chem. Soc.*, 2013, **135**, 17881–17888.

43 K. Sun, L. Zeng, S. Liu, L. Zhao, H. Zhu, J. Zhao, Z. Liu, D. Cao, Y. Hou, Y. Liu, Y. Pan and C. Liu, Design of basal plane active MoS_2 through one-step nitrogen and phosphorus co-doping as an efficient pH-universal electrocatalyst for hydrogen evolution, *Nano Energy*, 2019, **58**, 862–869.

44 X. Chen, Z. Wang, Y. Qiu, J. Zhang, G. Liu, W. Zheng, W. Feng, W. Cao, P. Hu and W. Hu, Controlled growth of vertical 3D $MoS_{2(1-x)}Se_{2x}$ nanosheets for an efficient and stable hydrogen evolution reaction, *J. Mater. Chem. A*, 2016, **4**, 18060–18066.

45 P. Liu, J. Zhu, J. Zhang, K. Tao, D. Gao and P. Xi, Active basal plane catalytic activity and conductivity in Zn doped MoS_2 nanosheets for efficient hydrogen evolution, *Electrochim. Acta*, 2018, **260**, 24–30.

46 Y. Liu, J. Wu, K. P. Hackenberg, J. Zhang, Y. M. Wang, Y. Yang, K. Keyshar, J. Gu, T. Ogitsu, R. Vajtai, J. Lou, P. M. Ajayan, B. C. Wood and B. I. Yakobson, Self-optimizing, highly surface-active layered metal dichalcogenide catalysts for hydrogen evolution, *Nat. Energy*, 2017, **2**, 17127.

47 R. Sun, M. K. Y. Chan and G. Ceder, First-principles electronic structure and relative stability of pyrite and marcasite: Implications for photovoltaic performance, *Phys. Rev. B: Condens. Matter Mater. Phys.*, 2011, **83**, 235311.

48 M. R. Gao, Y. R. Zheng, J. Jiang and S. H. Yu, Pyrite-type nanomaterials for advanced electrocatalysis, *Acc. Chem. Res.*, 2017, **50**, 2194–2204.

49 A. N. Buckley and R. Woods, Electrochemical and XPS studies of the surface oxidation of synthetic heazlewoodite (Ni_3S_2), *J. Appl. Electrochem.*, 1991, **21**, 575–582.

50 J. Dong, F. Q. Zhang, Y. Yang, Y. B. Zhang, H. He, X. Huang, X. Fan and X. M. Zhang, (003)-Facet-exposed Ni_3S_2 nanoporous thin films on nickel foil for efficient water splitting, *Appl. Catal. B Environ.*, 2019, **243**, 693–702.

51 Y. Chen, K. Yang, B. Jiang, J. Li, M. Zeng and L. Fu, Emerging two-dimensional nanomaterials for electrochemical hydrogen evolution, *J. Mater. Chem. A*, 2017, **5**, 8187–8208.

52 T. F. Jaramillo, K. P. Jørgensen, J. Bonde, J. H. Nielsen, S. Horch and I. Chorkendorff, Identification of Active Edge Sites for Electrochemical H_2 Evolution from MoS_2 Nanocatalysts, *Science*, 2007, **317**, 100–102.

53 R. Subbaraman, D. Tripkovic, K. C. Chang, D. Strmcnik, A. P. Paulikas, P. Hirunsit, M. Chan, J. Greeley, V. Stamenkovic and N. M. Markovic, Trends in activity for the water electrolyser reactions on 3d M (Ni, Co, Fe, Mn) hydr(oxy)oxide catalysts, *Nat. Mater.*, 2012, **11**, 550–557.

54 S. Jin, Are Metal Chalcogenides, Nitrides, and Phosphides Oxygen Evolution Catalysts or Bifunctional Catalysts?, *ACS Energy Lett.*, 2017, **2**, 1937–1938.

55 O. Mabayoje, A. Shoola, B. R. Wygant and C. B. Mullins, The Role of Anions in Metal Chalcogenide Oxygen Evolution Catalysis: Electrodeposited Thin Films of Nickel Sulfide as "Pre-catalysts", *ACS Energy Lett.*, 2016, **1**, 195–201.

56 S. A. Han, R. Bhatia and S. W. Kim, Synthesis, properties and potential applications of two-dimensional transition metal dichalcogenides, *Nano Converg.*, 2015, **2**, 17.

57 H. Li, J. Wu, Z. Yin and H. Zhang, Preparation and applications of mechanically exfoliated single-layer and multilayer MoS_2 and WSe_2 nanosheets, *Acc. Chem. Res.*, 2014, **47**, 1067–1075.

58 Z. Li, R. J. Young, C. Backes, W. Zhao, X. Zhang, A. A. Zhukov, E. Tillotson, A. P. Conlan, F. Ding, S. J. Haigh, K. S. Novoselov and J. N. Coleman, Mechanisms of Liquid-Phase Exfoliation for the Production of Graphene, *ACS Nano*, 2020, **14**, 10976–10985.

59 J. N. Coleman, M. Lotya, A. O'Neill, S. D. Bergin, P. J. King, U. Khan and K. Young, Two-dimensional nanosheets produced by liquid exfoliation of layered materials, *Science*, 2011, **331**, 568–571.

60 E. Varrla, C. Backes, K. R. Paton, A. Harvey, Z. Gholamvand, J. McCauley and J. N. Coleman, Large-scale production of size-controlled MoS_2 nanosheets by shear exfoliation, *Chem. Mater.*, 2015, **27**, 1129–1139.

61 X. Zhao, X. Ma, J. Sun, D. Li and X. Yang, Enhanced catalytic activities of surfactant-assisted exfoliated WS_2 nanodots for hydrogen evolution, *ACS Nano*, 2016, **10**, 2159–2166.

62 X. Fan, P. Xu, Y. C. Li, D. Zhou, Y. Sun, M. A. Nguyen, M. Terrones and T. E. Mallouk, Controlled exfoliation of MoS_2 crystals into trilayer nanosheets, *J. Am. Chem. Soc.*, 2016, **138**, 5143–5149.

63 N. Liu, P. Kim, J. H. Kim, J. H. Ye, S. Kim and C. J. Lee, Large-area atomically thin MoS_2 nanosheets prepared using electrochemical exfoliation, *ACS Nano*, 2014, **8**, 6902–6910.

64 X. Huang, Z. Zeng and H. Zhang, Metal dichalcogenide nanosheets: preparation, properties and applications, *Chem. Soc. Rev.*, 2013, **42**, 1934–1946.

65 S. C. Han, H. S. Kim, M. S. Song, J. H. Kim, H. J. Ahn and J. Y. Lee, Nickel sulfide synthesized by ball milling as an attractive cathode material for rechargeable lithium batteries, *J. Alloys Compd.*, 2003, **351**, 273–278.

66 A. Ambrosi, X. Chia, Z. Sofer and M. Pumera, Enhancement of electrochemical and catalytic properties of MoS2 through ball-milling, *Electrochem. Commun.*, 2015, **54**, 36–40.

67 P. Luo, H. Zhang, L. Liu, Y. Zhang, J. Deng, C. Xu, N. Hu and Y. Wang, Targeted synthesis of unique nickel sulfide (NiS, NiS_2) microarchitectures and the applications for the enhanced water splitting system, *ACS Appl. Mater. Interfaces*, 2017, **9**, 2500–2508.

68 W. Dong, X. Wang, B. Li, L. Wang, B. Chen, C. Li, X. Li, T. Zhang and Z. Shi, Hydrothermal synthesis and

structure evolution of hierarchical cobalt sulfide nanostructures, *Dalton Trans.*, 2011, **40**, 243–248.

69 Q. Xiong, X. Zhang, H. Wang, G. Liu, G. Wang, H. Zhang and H. Zhao, One-step synthesis of cobalt-doped MoS_2 nanosheets as bifunctional electrocatalysts for overall water splitting under both acidic and alkaline conditions, *Chem. Commun.*, 2018, **54**, 3859–3862.

70 Y. Li, H. Wang, L. Xie, Y. Liang, G. Hong and H. Dai, MoS_2 nanoparticles grown on graphene: an advanced catalyst for the hydrogen evolution reaction, *J. Am. Chem. Soc.*, 2011, **133**, 7296–7299.

71 C. Z. Yuan, Z. T. Sun, Y. F. Jiang, Z. K. Yang, N. Jiang, Z. W. Zhao, U. Y. Qazi, W. H. Zhang and A. W. Xu, One-step in situ growth of iron-nickel sulfide nanosheets on FeNi alloy foils: high-performance and self-supported electrodes for water oxidation, *Small*, 2017, **13**, 1604161.

72 Q. Wang, L. Jiao, H. Du, W. Peng, Y. Han, D. Song, Y. Si, Y. Wang and H. Yuan, Novel flower-like CoS hierarchitectures: one-pot synthesis and electrochemical properties, *J. Mater. Chem.*, 2011, **21**, 327–329.

73 J. Yuan, J. Wu, W. J. Hardy, P. Loya, M. Lou, Y. Yang, S. Najmaei, M. Jiang, F. Qin, K. Keyshar, H. Ji, W. Gao, J. Bao, J. Kono, D. Natelson, P. M. Ajayan and J. Lou, Facile synthesis of single cystal vanadium disulfide nanosheets by chemical vapor deposition for efficient hydrogen evolution reaction, *Adv. Mater.*, 2015, **27**, 5605–5609.

74 L. Samad, M. C. Acevedo, M. J. Shearer, K. Park, R. J. Hamers and S. Jin, Direct chemical vapor deposition synthesis of phase-pure iron pyrite (FeS_2) thin films, *Chem. Mater.*, 2015, **27**, 3108–3114.

75 J. Shi, X. Wang, S. Zhang, L. Xiao, Y. Huan, Y. Gong, Z. Zhang, Y. Li, X. Zhou, M. Hong, Q. Fang, Q. Zhang, X. Liu, L. Gu, Z. Liu and Y. Zhang, Two-dimensional metallic tantalum disulfide as a hydrogen evolution catalyst, *Nat. Commun.*, 2017, **8**, 958.

76 H. U. Kim, V. Kanade, M. Kim, K. S. Kim, B. S. An, H. Seok, H. Yoo, L. E. Chaney, S. I. Kim, C. W. Yang, G. Y. Yeom, D. Whang, J. H. Lee and T. Kim, Wafer-scale and low-temperature growth of 1T-WS_2 film for efficient and stable hydrogen evolution reaction, *Small*, 2020, **16**, 1905000.

77 I. Song, C. Park, M. Hong, J. Baik, H. J. Shin and H. C. Choi, Patternable large-scale molybdenium disulfide atomic layers grown by gold-assisted chemical vapor deposition, *Angew. Chem., Int. Ed.*, 2014, **126**, 1290–1293.

78 M. Wang, L. Zhang, M. Huang, Q. Zhang, X. Zhao, Y. He, S. Lin, J. Pan and H. Zhu, One-step synthesis of a hierarchical self-supported WS_2 film for efficient electrocatalytic hydrogen evolution, *J. Mater. Chem. A*, 2019, **7**, 22405–22411.

79 M. C. Acevedo, M. S. Faber, Y. Tan, R. J. Hamers and S. Jin, Synthesis and properties of semiconducting iron pyrite (FeS_2) nanowires, *Nano Lett.*, 2012, **12**, 1977–1982.

80 M. S. Faber, M. A. Lukowski, Q. Ding, N. S. Kaiser and S. Jin, Earth-abundant metal pyrites (FeS_2, CoS_2, NiS_2, and their alloys) for highly efficient hydrogen evolution and polysulfide reduction electrocatalysis, *J. Phys. Chem. C*, 2014, **118**, 21347–21356.

81 R. Miao, B. Dutta, S. Sahoo, J. He, W. Zhong, S. A. Cetegen, T. Jiang, S. P. Alpay and S. L. Suib, Mesoporous Iron Sulfide for Highly Efficient Electrocatalytic Hydrogen Evolution, *J. Am. Chem. Soc.*, 2017, **139**, 13604–13607.

82 M. C. Acevedo, D. Liang, K. S. Chew, J. P. DeGrave, N. S. Kaiser and S. Jin, Synthesis, Characterization, and Variable Range Hopping Transport of Pyrite (FeS_2) Nanorods, Nanobelts, and Nanoplates, *ACS Nano*, 2013, **7**(2), 1731–1739.

83 C. Bara, A. F. L. Humblot, E. Fonda, A. S. Gay, A. L. Taleb, E. Devers, M. Digne, G. D. Pirngruber and X. Carrier, Surface-dependent sulfidation and orientation of MoS_2 slabs on alumina-supported model hydrodesulfurization catalysts, *J. Catal.*, 2016, **344**, 591–605.

84 X. M. Geng, W. W. Sun, W. Wu, B. Chen, A. A. Hilo, M. Benamara, H. L. Zhu, F. Watanabe, J. B. Cui and T. Chen, Pure and stable metallic phase molybdenum disulfide nanosheets for hydrogen evolution reaction, *Nat. Commun.*, 2016, **7**, 10672.

85 H. Li, Y. Tan, P. Liu, C. Guo, M. Luo, J. Han, T. Lin, F. Huang and M. Chen, Atomic-Sized Pores Enhanced Electrocatalysis of TaS_2 Nanosheets for Hydrogen Evolution, *Adv. Mater.*, 2016, **28**, 8945–8949.

86 L. Najafi, S. Bellani, R. O. Nuñez, B. M. García, M. Prato, V. Mazánek, D. Debellis, S. Lauciello, R. Brescia, Z. Sofer and F. Bonaccorso, Niobium disulphide (NbS_2)-based heterogeneous electrocatalysts for an efficient hydrogen evolution reaction, *J. Mater. Chem. A*, 2019, **7**, 25593–25608.

87 J. Lin, Z. Peng, G. Wang, D. Zakhidov, E. Larios, M. J. Yacaman and J. M. Tour, Enhanced Electrocatalysis for Hydrogen Evolution Reactions from WS_2 Nanoribbons, *Adv. Energy Mater.*, 2014, **4**, 1301875.

88 Q. Tang and D. Jiang, Mechanism of Hydrogen Evolution Reaction on 1T-MoS_2 from First Principles, *ACS Catal.*, 2016, **6**, 4953–4961.

89 M. Zhang, Y. He, D. Yan, H. Xu, A. Wang, Z. Chen, S. Wang, H. Luo and K. Yan, Multifunctional 2H-TaS_2 nanoflakes for efficient supercapacitors and electrocatalytic evolution of hydrogen and oxygen, *Nanoscale*, 2019, **11**, 22255–22260.

90 K. Yan and Y. Lu, Direct Growth of MoS_2 Microspheres on Ni Foam as a Hybrid Nanocomposite Efficient for Oxygen Evolution Reaction, *Small*, 2016, **12**, 2975–2981.

91 J. Wu, M. Liu, K. Chatterjee, K. P. Hackenberg, J. Shen, X. Zou, Y. Yan, J. Gu, Y. Yang, J. Lou and P. M. Ajayan, Exfoliated 2D Transition Metal Disulfides for Enhanced Electrocatalysis of Oxygen Evolution Reaction in Acidic Medium, *Adv. Mater. Interfaces*, 2016, **3**, 1500669.

92 S. Wei, X. Cui, Y. Xu, B. Shang, Q. Zhang, L. Gu, X. Fan, L. Zheng, C. Hou, H. Huang, S. Wen and W. Zheng, Iridium-Triggered Phase Transition of MoS_2 Nanosheets Boosts Overall Water Splitting in Alkaline Media, *ACS Energy Lett.*, 2019, **4**, 368–374.

93 J. Zhang, T. Wang, D. Pohl, B. Rellinghaus, R. Dong, S. Liu, X. Zhuang and X. Feng, Interface Engineering of MoS_2/Ni_3S_2 Heterostructures for Highly Enhanced

Electrochemical Overall-Water-Splitting Activity, *Angew. Chem., Int. Ed.*, 2016, **55**, 6702–6707.

94 S. Peng, L. Li, J. Zhang, T. L. Tan, T. Zhang, D. Ji, X. Han, F. Cheng and S. Ramakrishna, Engineering Co_9S_8/WS_2 array films as bifunctional electrocatalysts for efficient water splitting, *J. Mater. Chem. A*, 2017, **5**, 23361–23368.

95 J. Hou, B. Zhang, Z. Li, S. Cao, Y. Sun, Y. Wu, Z. Gao and L. Sun, Vertically Aligned Oxygenated-CoS_2-MoS_2 Heteronanosheet Architecture from Polyoxometalate for Efficient and Stable Overall Water Splitting, *ACS Catal.*, 2018, **8**, 4612–4621.

96 J. Liu, J. Wang, B. Zhang, Y. Ruan, H. Wan, X. Ji, K. Xu, D. Zha, L. Miao and J. Jiang, Mutually beneficial Co_3O_4@MoS_2 heterostructures as a highly efficient bifunctional catalyst for electrochemical overall water splittin, *J. Mater. Chem. A*, 2018, **6**, 2067–2072.

97 Y. Yang, H. Yao, Z. Yu, S. M. Islam, H. He, M. Yuan, Y. Yue, K. Xu, W. Hao, G. Sun, H. Li, S. Ma, P. Zapol and M. G. Kanatzidis, Hierarchical Nanoassembly of MoS_2/Co_9S_8/Ni_3S_2/Ni as a Highly Efficient Electrocatalyst for Overall Water Splitting in a Wide pH Range, *J. Am. Chem. Soc.*, 2019, **141**, 10417–10430.

98 D. Wang, Q. Li, C. Han, Z. Xing and X. Yang, When NiO@Ni Meets WS_2 Nanosheet Array: A Highly Efficient and Ultrastable Electrocatalyst for Overall Water Splitting, *ACS Cent. Sci.*, 2018, **4**, 112–119.

99 D. Ji, S. Peng, L. Fan, L. Li, X. Qin and S. Ramakrishna, Thin MoS_2 nanosheets grafted MOFs-derived porous Co-N-C flakes grown on electrospun carbon nanofibers as self-supported bifunctional catalysts for overall water splitting, *J. Mater. Chem. A*, 2017, **5**, 23898–23908.

100 B. Shang, P. Ma, J. Fan, L. Jiao, Z. Liu, Z. Zhang, N. Chen, Z. Cheng, X. Cui and W. Zheng, Stabilized monolayer 1T MoS_2 embedded in CoOOH for highly efficient overall water splitting, *Nanoscale*, 2018, **10**, 12330–12336.

101 C. Xie, D. Yan, W. Chen, Y. Zou, R. Chen, S. Zang, Y. Wang, X. Yao and S. Wang, Insight into the design of defect electrocatalysts: From electronic structure to adsorption energy, *Mater. Today*, 2019, **31**, 47–68.

102 J. Deng, H. Li, J. Xiao, Y. Tu, D. Deng, H. Yang, H. Tian, J. Li, P. Ren and X. Bao, Triggering the electrocatalytic hydrogen evolution activity of the inert two-dimensional MoS_2 surface via single-atom metal doping, *Energy Environ. Sci.*, 2015, **8**, 1594–1601.

103 V. P. Pham and G. Y. Yeom, Recent Advances in Doping of Molybdenum Disulfide: Industrial Applications and Future Prospects, *Adv. Mater.*, 2016, **28**, 9024–9059.

104 Q. Xiong, Y. Wang, P. F. Liu, L. R. Zheng, G. Wang, H. G. Yang, P. K. Wong, H. Zhang and H. Zhao, Cobalt Covalent Doping in MoS_2 to Induce Bifunctionality of Overall Water Splitting, *Adv. Mater.*, 2018, **30**, 1801450.

105 U. N. Pan, T. I. Singh, D. R. Paudel, C. C. Gudal, N. H. Kim and J. H. Lee, Covalent doping of Ni and P on 1T-enriched MoS_2 bifunctional 2D-nanostructures with active basal planes and expanded interlayers boosts electrocatalytic water splitting, *J. Mater. Chem. A*, 2020, **8**, 19654–19664.

106 J. Y. Xue, F. L. Li, Z. Y. Zhao, C. Li, C. Y. Ni, H. W. Gu, D. J. Young and J. P. Lang, In Situ Generation of Bifunctional Fe-Doped MoS_2 Nanocanopies for Efficient Electrocatalytic Water Splitting, *Inorg. Chem.*, 2019, **58**, 11202–11209.

107 X. Xu, H. Xu and D. Cheng, Design of high-performance MoS_2 edge supported single-metal atom bifunctional catalysts for overall water splitting via a simple equation, *Nanoscale*, 2019, **11**, 20228–20237.

108 I. S. Kwon, T. T. Debela, I. H. Kwak, Y. C. Park, J. Seo, J. Y. Shim, S. J. Yoo, J. G. Kim, J. Park and H. S. Kang, Ruthenium Nanoparticles on Cobalt-Doped 1T' Phase MoS_2 Nanosheets for Overall Water Splitting, *Small*, 2020, **16**, 2000081.

109 N. Jiang, Q. Tang, M. L. Sheng, B. You, D. Jiang and Y. J. Sun, Nickel sulfides for electrocatalytic hydrogen evolution under alkaline conditions: a case study of crystalline NiS, NiS_2, and Ni_3S_2 nanoparticles, *Catal. Sci. Technol.*, 2016, **6**, 1077–1084.

110 X. Shi, X. Ling, L. Li, C. Zhong, Y. Deng, X. Han and W. Hu, Nanosheets assembled into nickel sulfide nanospheres with enriched Ni^{3+} active sites for efficient water-splitting and zinc-air batteries, *J. Mater. Chem. A*, 2019, **7**, 23787–23793.

111 X. Zheng, X. Han, Y. Zhang, J. Wang, C. Zhong, Y. Deng and W. Hu, Controllable synthesis of nickel sulfide nanocatalysts and their phase-dependent performance for overall water splitting, *Nanoscale*, 2019, **11**, 5646–5654.

112 L. Zeng, K. Sun, Z. Yang, S. Xie, Y. Chen, Z. Liu, Y. Liu, J. Zhao, Y. Liu and C. Liu, Tunable 3D hierarchical Ni_3S_2 superstructures as efficient and stable bifunctional electrocatalysts for both H_2 and O_2 generation, *J. Mater. Chem. A*, 2018, **6**, 4485–4493.

113 J. Zhang, Y. Li, T. Zhu, Y. Wang, J. Cui, J. Wu, H. Xu, X. Shu, Y. Qin, H. Zheng, P. M. Ajayan, Y. Zhang and Y. Wu, 3D Coral-Like Ni_3S_2 on Ni Foam as a Bifunctional Electrocatalyst for Overall Water Splitting, *ACS Appl. Mater. Interfaces*, 2018, **10**, 31330–31339.

114 W. Zhu, X. Yue, W. Zhang, S. Yu, Y. Zhang, J. Wang and J. Wang, Nickel sulfide microsphere film on Ni foam as an efficient bifunctional electrocatalyst for overall water splitting, *Chem. Commun.*, 2016, **52**, 1486–1489.

115 X. Ma, W. Zhang, Y. Deng, C. Zhong, W. Hu and X. Han, Phase and composition controlled synthesis of cobalt sulfide hollow nanospheres for electrocatalytic water splitting, *Nanoscale*, 2018, **10**, 4816–4824.

116 M. Fronzi, M. H. N. Assadi and M. J. Ford, Ab Initio Investigation of Water Adsorption and Hydrogen Evolution on Co_9S_8 and Co_3S_4 Low-Index Surfaces, *ACS Omega*, 2018, **3**, 12215–12228.

117 Z. Li, M. Xiao, Y. Zhou, D. Zhang, H. Wang, X. Liu, D. Wang and W. Wang, Pyrite FeS_2/C nanoparticles as an efficient bi-functional catalyst for overall water splitting, *Dalton Trans.*, 2018, **47**, 14917–14923.

118 H. Li, S. Chen, Y. Zhang, Q. Zhang, X. Jia, Q. Zhang, L. Gu, X. Sun, L. Song and X. Wang, Systematic design of superaerophobic nanotube-array electrode comprised of

transition-metal sulfides for overall water splitting, *Nat. Commun.*, 2018, **9**, 2452.

119 Y. Li, J. Yin, L. An, M. Lu, K. Sun, Y. Q. Zhao, D. Gao, F. Cheng and P. Xi, FeS_2/CoS_2 Interface Nanosheets as Efficient Bifunctional Electrocatalyst for Overall Water Splitting, *Small*, 2018, **14**, 1801070.

120 H. Zhu, J. Zhang, R. Y. Zhang, M. Du, Q. Wang, G. Gao, J. Wu, G. Wu, M. Zhang, B. Liu, J. Yao and X. Zhang, When cubic cobalt sulfide meets layered molybdenum disulfide: a core-shell system toward synergetic electrocatalytic water splitting, *Adv. Mater.*, 2015, **27**, 4752–4759.

121 J. Lin, H. Wang, X. Zheng, Y. Du, C. Zhao, J. Qi, J. Cao, W. Fei and J. Feng, Controllable synthesis of core-branch Ni_3S_2/Co_9S_8 directly on nickel foam as an efficient bifunctional electrocatalyst for overall water splitting, *J. Power Sources*, 2018, **401**, 329–335.

122 W. Xin, W. J. Jiang, Y. Lian, H. Li, S. Hong, S. Xu, H. Yan and J. S. Hu, NiS_2 nanodotted carnation-like CoS_2 for enhanced electrocatalytic water splitting, *Chem. Commun.*, 2019, **55**, 3781–3784.

123 Q. Li, D. Wang, C. Han, X. Ma, Q. Lu, Z. Xing and X. Yang, Construction of amorphous interface in an interwoven NiS/NiS_2 structure for enhanced overall water splitting, *J. Mater. Chem. A*, 2018, **6**, 8233–8237.

124 F. Jing, Q. Lv, J. Xiao, Q. Wang and S. Wang, Highly active and dual-function self-supported multiphase NiS-NiS_2-Ni_3S_2/NF electrodes for overall water splitting, *J. Mater. Chem. A*, 2018, **6**, 14207–14214.

125 Y. Y. Wu, G. D. Li, Y. P. Liu, L. Yang, X. R. Lian, T. Asefa and X. X. Zou, Overall Water Splitting Catalyzed Efficiently by an Ultrathin Nanosheet-Built, Hollow Ni_3S_2-Based Electrocatalyst, *Adv. Funct. Mater.*, 2016, **26**, 4839–4847.

126 X. Luo, Q. Zhou, S. Du, J. Li, J. Zhong, X. Deng and Y. Liu, Porous Co_9S_8/Nitrogen, Sulfur-Doped Carbon@Mo_2C Dual Catalyst for Efficient Water Splitting, *ACS Appl. Mater. Interfaces*, 2018, **10**, 22291–22302.

127 J. Y. Wang, T. Ouyang, Y. P. Deng, Y. S. Hong and Z. Q. Liu, Metallic Mo_2C anchored pyrrolic-N induced N-CNTs/NiS_2 for efficient overall water electrolysis, *J. Power Sources*, 2019, **420**, 108–117.

128 J. J. Lv, J. Zhao, H. Fang, L. P. Jiang, L. L. Li, J. Ma and J. J. Zhu, Incorporating Nitrogen-Doped Graphene Quantum Dots and Ni_3S_2 Nanosheets: A Synergistic Electrocatalyst with Highly Enhanced Activity for Overall Water Splitting, *Small*, 2017, **13**, 1700264.

129 M. Guo, A. Qayum, S. Dong, X. Jiao, D. Chen and T. Wang, In situ conversion of metal (Ni, Co or Fe) foams into metal sulfide (Ni_3S_2, Co_9S_8 or FeS) foams with surface grown N-doped carbon nanotube arrays as efficient superaerophobic electrocatalysts for overall water splitting, *J. Mater. Chem. A*, 2020, **8**, 9239–9247.

130 H. Liu, C. Y. Xu, Y. Du, F. X. Ma, Y. Li, J. Yu and L. Zhen, Ultrathin Co_9S_8 nanosheets vertically aligned on N, S/rGO for low voltage electrolytic water in alkaline media, *Sci. Rep.*, 2019, **9**, 1951.

131 Y. Tong, X. Yu and G. Shi, Cobalt disulfide/graphite foam composite films as self-standing electrocatalytic electrodes for overall water splitting, *Phys. Chem. Chem. Phys.*, 2017, **19**, 4821–4826.

132 J. Hao, W. Yang, Z. Peng, C. Zhang, Z. Huang and W. Shi, A Nitrogen Doping Method for CoS_2 Electrocatalysts with Enhanced Water Oxidation Performance, *ACS Catal.*, 2017, **7**, 4214–4220.

133 N. Yao, P. Li, Z. Zhou, R. Meng, G. Cheng and W. Luo, Nitrogen Engineering on 3D Dandelion-Flower-Like CoS_2 for High-Performance Overall Water Splitting, *Small*, 2019, **15**, 1901993.

134 H. Liu, Q. He, H. Jiang, Y. Lin, Y. Zhang, M. Habib, S. Chen and L. Song, Electronic Structure Reconfiguration toward Pyrite NiS_2 via Engineered Heteroatom Defect Boosting Overall Water Splitting, *ACS Nano*, 2017, **11**, 11574–11583.

135 P. Chen, T. Zhou, M. Zhang, Y. Tong, C. Zhong, N. Zhang, L. Zhang, C. Wu and Y. Xie, 3D Nitrogen-Anion-Decorated Nickel Sulfides for Highly Efficient Overall Water Splitting, *Adv. Mater.*, 2017, **29**, 1701584.

136 X. Y. Y. Lou and X. W. Lou, Mixed Metal Sulfides for Electrochemical Energy Storage and Conversion, *Adv. Energy Mater.*, 2018, **8**, 1701592.

137 A. Sivanantham, P. Ganesan and S. Shanmugam, Hierarchical $NiCo_2S_4$ Nanowire Arrays Supported on Ni Foam: An Efficient and Durable Bifunctional Electrocatalyst for Oxygen and Hydrogen Evolution Reactions, *Adv. Funct. Mater.*, 2016, **26**, 4661–4672.

138 Y. Gong, H. Pan, Z. Xu, Z. Yang, Y. Lin and J. Wang, Crossed $FeCo_2S_4$ nanosheet arrays grown on 3D nickel foam as high-efficient electrocatalyst for overall water splitting, *Int. J. Hydrogen Energy*, 2018, **43**, 17259–17264.

139 J. Yu, G. Cheng and W. Luo, Ternary nickel-iron sulfide microflowers as a robust electrocatalyst for bifunctional water splitting, *J. Mater. Chem. A*, 2017, **5**, 15838–15844.

140 D. Li, Z. Liu, J. Wang, B. Liu, Y. Qin, W. Yang and J. Liu, Hierarchical trimetallic sulfide $FeCo_2S_4$-$NiCo_2S_4$ nanosheet arrays supported on a Ti mesh: An efficient 3D bifunctional electrocatalyst for full water splitting, *Electrochim. Acta*, 2020, **340**, 135957.

141 L. Wang, X. Duan, X. Liu, J. Gu, R. Si, Y. Qiu, Y. M. Qiu, D. Shi, F. Chen, X. Sun, J. Lin and J. Sun, Atomically Dispersed Mo Supported on Metallic Co_9S_8 Nanoflakes as an Advanced Noble-Metal-Free Bifunctional Water Splitting Catalyst Working in Universal pH Conditions, *Adv. Energy Mater.*, 2020, **10**, 1903137.

142 L. L. Feng, G. Yu, Y. Wu, G. D. Li, H. Li, Y. Sun, T. Asefa, W. Chen and X. Zou, High-index faceted Ni_3S_2 nanosheet arrays as highly active and ultrastable electrocatalysts for water splitting, *J. Am. Chem. Soc.*, 2015, **137**, 14023–14026.

143 Y. Li, Y. Wang, B. Pattengale, J. Yin, L. An, F. Cheng, Y. Li, J. Huang and P. Xi, High-index faceted $CuFeS_2$ nanosheets with enhanced behavior for boosting hydrogen evolution reaction, *Nanoscale*, 2017, **9**, 9230–9237.

144 N. Zhang, J. Lei, J. Xie, H. Huang and Y. Yu, MoS_2/Ni_3S_2 nanorod arrays well-aligned on Ni foam: a 3D hierarchical

efficient bifunctional catalytic electrode for overall water splitting, *RSC Adv.*, 2017, **7**, 46286–46296.

145 C. Guan, X. Liu, A. M. Elshahawy, H. Zhang, H. Wu, S. J. Pennycook and J. Wang, Metal-organic framework derived hollow CoS_2 nanotube arrays: an efficient bifunctional electrocatalyst for overall water splitting, *Nanoscale Horiz.*, 2017, **2**, 342–348.

146 C. Yan, J. Huang, C. Wu, Y. Li, Y. Tan, L. Zhang, Y. Sun, X. Huang and J. Xiong, In-situ formed NiS/Ni coupled interface for efficient oxygen evolution and hydrogen evolution, *J. Mater. Sci. Technol.*, 2020, **42**, 10–16.

147 B. You, M. T. Tang, C. Tsai, F. A. Pedersen, X. Zheng and H. Li, Enhancing Electrocatalytic Water Splitting by Strain Engineering, *Adv. Mater.*, 2019, **31**, 1807001.

148 X. Chen and G. Wang, Tuning the hydrogen evolution activity of MS_2 (M = Mo or Nb) monolayers by strain engineering, *Phys. Chem. Chem. Phys.*, 2016, **18**, 9388–9395.

149 Y. Shan and T. Li, Strain-regulated electronic structure for hydrogen evolution reaction in Fe_3S_4 monolayer, *Phys. Lett. A*, 2020, **384**, 126368.

150 J. Zhang, W. Xiao, P. Xi, S. Xi, Y. Du, D. Gao and J. Ding, Activating and Optimizing Activity of CoS_2 for Hydrogen Evolution Reaction through the Synergic Effect of N Dopants and S Vacancies, *ACS Energy Lett.*, 2017, **2**, 1022–1028.

151 J. Lin, P. Wang, H. Wang, C. Li, X. Si, J. Qi, J. Cao, Z. Zhong, W. Fei and J. Feng, Defect-Rich Heterogeneous MoS_2/NiS_2 Nanosheets Electrocatalysts for Efficient Overall Water Splitting, *Adv. Sci.*, 2019, **6**, 1900246.

152 X. Zhu, J. Dai, L. Li, D. Zhao, Z. Wu, Z. Tang, L. J. Ma and S. Chen, Hierarchical carbon microflowers supported defect-rich Co_3S_4 nanoparticles: an efficient electrocatalyst for water splitting, *Carbon*, 2020, **160**, 133–144.

153 Z. Cui, Y. Ge, H. Chu, R. Baines, P. Dong, J. Tang, Y. Yang, P. M. Ajayan, M. Ye and J. Shen, Controlled synthesis of Mo-doped Ni_3S_2 nanorods: an efficient and stable electrocatalyst for water splitting, *J. Mater. Chem. A*, 2017, **5**, 1595–1602.

154 G. Huang, Z. Xiao, R. Chen and S. Wang, Defect Engineering of Cobalt-Based Materials for Electrocatalytic Water Splitting, *ACS Sustainable Chem. Eng.*, 2018, **6**, 15954–15969.

155 S. Li, Y. Zhang and X. Niu, Defects and impurities induced structural and electronic changes in pyrite CoS_2: first principles studies, *Phys. Chem. Chem. Phys.*, 2018, **20**, 11649–11655.

156 W. Yang, J. Zeng, Y. Hua, C. Xu, S. S. Siwal and Q. Zhang, Defect engineering of cobalt microspheres by S doping and electrochemical oxidation as efficient bifunctional and durable electrocatalysts for water splitting at high current densities, *J. Power Sources*, 2019, **436**, 226887.

157 X. Zhao, H. Liu, Y. Rao, X. Li, J. Wang, G. Xia and M. Wu, Carbon Dots Decorated Hierarchical $NiCo_2S_4/Ni_3S_2$ Composite for Efficient Water Splitting, *ACS Sustainable Chem. Eng.*, 2019, **7**, 2610–2618.

158 P. Hu, Z. Jia, H. Che, W. Zhou, N. Liu, F. Li and J. Wang, Engineering hybrid $CoMoS_4/Ni_3S_2$ nanostructures as efficient bifunctional electrocatalyst for overall water splitting, *J. Power Sources*, 2019, **416**, 95–103.

159 Y. Tan, M. Luo, P. Liu, C. Cheng, J. Han, K. Watanabe and M. Chen, Three-Dimensional Nanoporous $Co_9S_4P_4$ Pentlandite as a Bifunctional Electrocatalyst for Overall Neutral Water Splitting, *ACS Appl. Mater. Interfaces*, 2019, **11**, 3880–3888.

160 M. He, C. Feng, T. Liao, S. Hu, H. Wu and Z. Sun, Low-Cost $Ni_2P/Ni_{0.96}S$ Heterostructured Bifunctional Electrocatalyst toward Highly Efficient Overall Urea-Water Electrolysis, *ACS Appl. Mater. Interfaces*, 2019, **12**, 2225–2233.

161 Y. Yang, K. Zhang, H. Lin, X. Li, H. C. Chan, L. Yang and Q. Gao, MoS_2-Ni_3S_2 Heteronanorods as Efficient and Stable Bifunctional Electrocatalysts for Overall Water Splitting, *ACS Catal.*, 2017, **7**, 2357–2366.

162 F. Li, D. Zhang, R. C. Xu, W. F. Fu and X. J. Lv, Superhydrophilic Heteroporous MoS_2/Ni_3S_2 for Highly Efficient Electrocatalytic Overall Water Splitting, *ACS Appl. Energy Mater.*, 2018, **1**, 3929–3936.

163 Q. Qin, L. Chen, T. Wei and X. Liu, MoS_2/NiS Yolk-Shell Microsphere-Based Electrodes for Overall Water Splitting and Asymmetric Supercapacitor, *Small*, 2019, **15**, 1803639.

164 D. Zhang, L. Jiang, Y. Liu, L. Qiu, J. Zhang and D. Yuan, Ni_3S_2-MoS_x nanorods grown on Ni foam as high-efficient electrocatalysts for overall water splitting, *Int. J. Hydrogen Energy*, 2019, **44**, 17900–17908.

165 N. Huang, S. Yan, M. Zhang, Y. Ding, L. Yang, P. Sun and X. Sun, A MoS_2-Co_9S_8-NC heterostructure as an efficient bifunctional electrocatalyst towards hydrogen and oxygen evolution reaction, *Electrochim. Acta*, 2019, **327**, 134942.

166 S. Shit, S. Chhetri, S. Bolar, N. C. Murmu, W. Jang, H. Koo and T. Kuila, Hierarchical Cobalt Sulfide/Molybdenum Sulfide Heterostructure as Bifunctional Electrocatalyst towards Overall Water Splitting, *ChemElectroChem*, 2019, **6**, 430–438.

167 M. S. Islam, M. Kim, X. Jin, S. M. Oh, N. S. Lee, H. Kim and S. J. Hwang, Bifunctional 2D Superlattice Electrocatalysts of Layered Double Hydroxide-Transition Metal Dichalcogenide Active for Overall Water Splitting, *ACS Energy Lett.*, 2018, **3**, 952–960.

168 Y. Liu, S. Jiang, S. Li, L. Zhou, Z. Li, J. Li and M. Shao, Interface engineering of (Ni, Fe)S_2@MoS_2 heterostructures for synergetic electrochemical water splitting, *Appl. Catal. B Environ.*, 2019, **247**, 107–114.

169 P. Kuang, M. He, H. Zou, J. Yu and K. Fan, 0D/3D MoS_2-NiS_2/N-doped graphene foam composite for efficient overall water splitting, *Appl. Catal. B Environ.*, 2019, **254**, 15–25.

170 T. Yoon and K. S. Kim, One-Step Synthesis of CoS-Doped β-$Co(OH)_2$@Amorphous MoS_{2+x} Hybrid Catalyst Grown on Nickel Foam for High-Performance Electrochemical Overall Water Splitting, *Adv. Funct. Mater.*, 2016, **26**, 7386–7393.

171 Y. Zhu, L. Song, N. Song, M. Li, C. Wang and X. Lu, Bifunctional and Efficient CoS_2-C@MoS_2 Core-Shell

Nanofiber Electrocatalyst for Water Splitting, *ACS Sustainable Chem. Eng.*, 2019, **7**, 2899–2905.

172 V. Ganesan and J. Kim, Multi-shelled CoS_2-MoS_2 hollow spheres as efficient bifunctional electrocatalysts for overall water splitting, *Int. J. Hydrogen Energy*, 2020, **45**, 13290–13299.

173 Y. Guo, J. Tang, Z. Wang, Y. M. Kang, Y. Bando and Y. Yamauchi, Elaborately assembled core-shell structured metal sulfides as a bifunctional catalyst for highly efficient electrochemical overall water splitting, *Nano Energy*, 2018, **47**, 494–502.

174 A. Muthurasu, V. Maruthapandian and H. Y. Kim, Metal-organic framework derived Co_3O_4/MoS_2 heterostructure for efficient bifunctional electrocatalysts for oxygen evolution reaction and hydrogen evolution reaction, *Appl. Catal. B Environ.*, 2019, **248**, 202–210.

175 Y. Wang, T. Williams, T. Gengenbach, B. Kong, D. Zhao, H. Wang and C. Selomulya, Unique hybrid Ni_2P/MoO_2@MoS_2 nanomaterials as bifunctional non-noble-metal electro-catalysts for water splitting, *Nanoscale*, 2017, **9**, 17349–17356.

176 R. Prasannachandran, T. V. Vineesh, M. B. Lithin, R. Nandakishore and M. M. Shaijumon, Phosphorene-quantum-dot-interspersed few-layered MoS_2 hybrids as efficient bifunctional electrocatalysts for hydrogen and oxygen evolution, *Chem. Commun.*, 2020, **56**, 8623–8626.

177 Y. Xu, X. Chai, T. Ren, H. Yu, S. Yin, Z. Wang, X. Li, L. Wang and H. Wang, Synergism of Interface and Electronic Effects: Bifunctional N-Doped Ni_3S_2/N-Doped MoS_2 Hetero-Nanowires for Efficient Electrocatalytic Overall Water Splitting, *Chem.–Eur J.*, 2019, **25**, 16074–16080.

178 Z. Zhai, C. Li, L. Zhang, H. C. Wu, L. Zhang, N. Tang, W. Wang and J. Gong, Dimensional construction and morphological tuning of heterogeneous MoS_2/NiS electrocatalysts for efficient overall water splitting, *J. Mater. Chem. A*, 2018, **6**, 9833–9838.

179 A. Muthurasu, G. P. Ojha, M. Lee and H. Y. Kim, Zeolitic imidazolate framework derived Co_3S_4 hybridized MoS_2-Ni_3S_2 heterointerface for electrochemical overall water splitting reactions, *Electrochim. Acta*, 2020, **334**, 135537.

180 C. Qin, A. Fan, X. Zhang, S. Wang, X. Yuan and X. Dai, Interface engineering: few-layer MoS_2 coupled to a NiCo-sulfide nanosheet heterostructure as a bifunctional electrocatalyst for overall water splitting, *J. Mater. Chem. A*, 2019, **7**, 27594–27602.

181 Y. Wu, F. Li, W. Chen, Q. Xiang, Y. Ma, H. Zhu, P. Tao, C. Song, W. Shang, T. Deng and J. Wu, Coupling Interface Constructions of MoS_2/$Fe_5Ni_4S_8$ Heterostructures for Efficient Electrochemical Water Splitting, *Adv. Mater.*, 2018, **30**, 1803151.

182 H. Li, S. Chen, X. Jia, B. Xu, H. Lin, H. Yang, L. Song and X. Wang, Amorphous nickel-cobalt complexes hybridized with 1T-phase molybdenum disulfide via hydrazine-induced phase transformation for water splitting, *Nat. Commun.*, 2017, **8**, 15377.

183 T. Yang, L. Yin, M. He, W. Wei, G. Cao, X. Ding, Y. Wang, Z. Zhao, T. Yu, H. Zhao and D. Zhang, Yolk-shell hierarchical catalyst with tremella-like molybdenum sulfide on transition metal (Co, Ni and Fe) sulfide for electrochemical water splitting, *Chem. Commun.*, 2019, **55**, 14343–14346.

184 J. Y. Xue, F. L. Li, Z. Y. Zhao, C. Li, C. Y. Ni, H. W. Gu, P. Braunstein, X. Q. Huang and J. P. Lang, A hierarchically-assembled Fe-MoS_2/Ni_3S_2/nickel foam electrocatalyst for efficient water splitting, *Dalton Trans.*, 2019, **48**, 12186–12192.

185 X. Zou, Y. Wu, Y. Liu, D. Liu, W. Li, L. Gu, H. Liu, P. Wang, L. Sun and Y. Zhang, In Situ Generation of Bifunctional, Efficient Fe-Based Catalysts from Mackinawite Iron Sulfide for Water Splitting, *Chem*, 2018, **4**, 1139–1152.

186 S. Shit, S. Bolar, N. C. Murmu and T. Kuila, Binder-Free Growth of Nickel-Doped Iron Sulfide on Nickel Foam via Electrochemical Deposition for Electrocatalytic Water Splitting, *ACS Sustainable Chem. Eng.*, 2019, **7**, 18015–18026.

187 L. Gao, C. Guo, X. Liu, X. Ma, M. Zhao, X. Kuang, H. Yang, X. Zhu, X. Sun and Q. Wei, Co-Doped FeS_2 with a porous structure for efficient electrocatalytic overall water splitting, *New J. Chem.*, 2020, **44**, 1711–1718.

188 S. Wang, P. Ning, S. Huang, W. Wang, S. Fei, Q. He, J. Zai, Y. Jiang, Z. Hu, X. Qian and Z. Chen, Multi-functional NiS_2/FeS_2/N-doped carbon nanorods derived from metal-organic frameworks with fast reaction kinetics for high performance overall water splitting and lithium-ion batteries, *J. Power Sources*, 2019, **436**, 226857.

189 R. Zhang, Z. Zhu, J. Lin, K. Zhang, N. Li and C. Zhao, Hydrolysis assisted in situ growth of 3D hierarchical FeS/NiS/nickel foam electrode for overall water splitting, *Electrochim. Acta*, 2020, **332**, 135534.

190 N. Yao, T. Tan, F. Yang, G. Cheng and W. Luo, Well-aligned metal-organic framework array-derived CoS_2 nanosheets toward robust electrochemical water splitting, *Mater. Chem. Front.*, 2018, **2**, 1732–1738.

191 R. Souleymen, Z. T. Wang, C. Qiao, M. Naveed and C. B. Cao, Microwave-assisted synthesis of graphene-like cobalt sulfide freestanding sheets as an efficient bifunctional electrocatalyst for overall water splitting, *J. Mater. Chem. A*, 2018, **6**, 7592–7607.

192 Y. Li, X. Fu, W. Zhu, J. Gong, J. Sun, D. Zhang and J. Wang, Self-ZIF template-directed synthesis of a CoS nanoflake array as a Janus electrocatalyst for overall water splitting, *Inorg. Chem. Front.*, 2019, **6**, 2090–2095.

193 Y. Yang, M. Yuan, H. Li, G. Sun and S. Ma, Controllable synthesis of ultrathin Co_9S_8 nanosheets as a highly efficient electrocatalyst for overall water splitting, *Electrochim. Acta*, 2018, **281**, 198–207.

194 M. Zhu, Z. Zhang, H. Zhang, H. Zhang, X. Zhang, L. Zhang and S. Wang, Hydrophilic cobalt sulfide nanosheets as a bifunctional catalyst for oxygen and hydrogen evolution in electrolysis of alkaline aqueous solution, *J. Colloid Interface Sci.*, 2018, **509**, 522–528.

195 X. Du, G. Ma and X. Zhang, Mo-doped Co_9S_8 nanorod array as a high performance electrochemical water splitting

catalyst in alkaline solution, *Int. J. Hydrogen Energy*, 2019, **44**, 27765–27771.

196 X. Du, H. Su and X. Zhang, Metal-Organic Framework-Derived Cu-Doped Co_9S_8 Nanorod Array with Less Low-Valence Co Sites as Highly Efficient Bifunctional Electrodes for Overall Water Splitting, *ACS Sustainable Chem. Eng.*, 2019, **7**, 16917–16926.

197 X. Du, H. Su and X. Zhang, Cr doped-Co_9S_8 nanoarrays as high-efficiency electrocatalysts for water splitting, *J. Alloys Compd.*, 2020, **824**, 153965.

198 X. Du, H. Su and X. Zhang, Metal-organic framework-derived M (M = Fe, Ni, Zn and Mo) doped Co_9S_8 nanoarrays as efficient electrocatalyst for water splitting: The combination of theoretical calculation and experiment, *J. Catal.*, 2020, **383**, 103–116.

199 S. Tang, X. Wang, Y. Zhang, M. Courte, H. J. Fan and D. Fichou, Combining Co_3S_4 and Ni:Co_3S_4 nanowires as efficient catalysts for overall water splitting: an experimental and theoretical study, *Nanoscale*, 2019, **11**, 2202–2210.

200 L. Lei, D. Huang, C. Zhang, R. Deng, S. Chen and Z. Li, F dopants triggered active sites in bifunctional cobalt sulfide@nickel foam toward electrocatalytic overall water splitting in neutral and alkaline media: Experiments and theoretical calculations, *J. Catal.*, 2020, **385**, 129–139.

201 Y. Li, Z. Mao, Q. Wang, D. Li, R. Wang, B. He, Y. Gong and H. Wang, Hollow nanosheet array of phosphorus-anion-decorated cobalt disulfide as an efficient electrocatalyst for overall water splitting, *Chem. Eng. J.*, 2020, **390**, 124556.

202 Z. Dai, H. Geng, J. Wang, Y. Luo, B. Li, Y. Zong, J. Yang, Y. Guo, Y. Zheng, X. Wang and Q. Yan, Hexagonal-Phase Cobalt Monophosphosulfide for Highly Efficient Overall Water Splitting, *ACS Nano*, 2017, **11**, 11031–11040.

203 S. Deng, Y. Zhong, Y. Zeng, Y. Wang, X. Wang, X. Lu, X. Xia and J. Tu, Hollow TiO_2@Co_9S_8 Core-Branch Arrays as Bifunctional Electrocatalysts for Efficient Oxygen/Hdrogen Production, *Adv. Sci.*, 2018, **5**, 1700772.

204 C. Ray, S. C. Lee, K. V. Sankar, B. Jin, J. Lee, J. H. Park and S. C. Jun, Amorphous Phosphorus-Incorporated Cobalt Molybdenum Sulfide on Carbon Cloth: An Efficient and Stable Electrocatalyst for Enhanced Overall Water Splitting over Entire pH Values, *ACS Appl. Mater. Interfaces*, 2017, **9**, 37739–37749.

205 Y. Chen, S. Xu, S. Zhu, R. J. Jacob, G. Pastel, Y. Wang, Y. Li, J. Dai, F. Chen, H. Xie, B. Liu, Y. Yao, L. G. S. Riba, M. R. Zachariah, T. Li and L. Hu, Millisecond synthesis of CoS nanoparticles for highly efficient overall water splitting, *Nano Res.*, 2019, **12**, 2259–2267.

206 W. Zhang, X. Ma, C. Zhong, T. Ma, Y. Deng, W. Hu and X. Han, Pyrite-Type CoS_2 Nanoparticles Supported on Nitrogen-Doped Graphene for Enhanced Water Splitting, *Front. Chem.*, 2018, **6**, 569.

207 S. Huang, Y. Meng, S. He, A. Goswami, Q. Wu, J. Li, S. Tong, T. Asefa and M. Wu, N-, O-, and S-Tridoped Carbon-Encapsulated Co_9S_8 Nanomaterials: Efficient Bifunctional Electrocatalysts for Overall Water Splitting, *Adv. Funct. Mater.*, 2017, **27**, 1606585.

208 J. Y. Wang, T. Ouyang, N. Li, T. Y. Ma and Z. Q. Liu, S, N co-doped carbon nanotube-encapsulated core-shelled CoS_2@Co nanoparticles: efficient and stable bifunctional catalysts for overall water splitting, *Sci. Bull.*, 2018, **63**, 1130–1140.

209 J. Li, W. Xu, J. Luo, D. Zhou, D. Zhang, L. Wei, P. Xu and D. Yuan, Synthesis of 3D Hexagram-Like Cobalt-Manganese Sulfides Nanosheets Grown on Nickel Foam: A Bifunctional Electrocatalyst for Overall Water Splitting, *Nanomicro Lett.*, 2018, **10**, 6.

210 R. Huang, W. Chen, Y. Zhang, Z. Huang, H. Dai, Y. Zhou, Y. Wu and X. Lv, Well-designed cobalt-nickel sulfide microspheres with unique peapod-like structure for overall water splitting, *J. Colloid Interface Sci.*, 2019, **556**, 401–410.

211 Z. Liang, Z. Yang, J. Dang, J. Qi, H. Yuan, J. Gao, W. Zhang, H. Zheng and R. Cao, Hollow Bimetallic Zinc Cobalt Phosphosulfides for Efficient Overall Water Splitting, *Chemistry*, 2019, **25**, 621–626.

212 S. Czioska, J. Wang, X. Teng and Z. Chen, Hierarchically Structured $CuCo_2S_4$ Nanowire Arrays as Efficient Bifunctional Electrocatalyst for Overall Water Splitting, *ACS Sustainable Chem. Eng.*, 2018, **6**, 11877–11883.

213 C. Zequine, S. Bhoyate, F. Wang, X. Li, K. Siam, P. K. Kahol and R. K. Gupta, Effect of solvent for tailoring the nanomorphology of multinary $CuCo_2S_4$ for overall water splitting and energy storage, *J. Alloys Compd.*, 2019, **784**, 1–7.

214 X. Du, J. Fu and X. Zhang, Controlled Synthesis of $CuCo_2S_4$@$Ni(OH)_2$ Hybrid Nanorod Arrays for Water Splitting at an Ultralow Cell Voltage of 1.47 V, *Chem. Asian J.*, 2019, **14**, 3386–3396.

215 J. Hu, Y. Ou, Y. Li, D. Gao, Y. Zhang and P. Xiao, $FeCo_2S_4$ Nanosheet Arrays Supported on Ni Foam: An Efficient and Durable Bifunctional Electrocatalyst for Overall Water-Splitting, *ACS Sustainable Chem. Eng.*, 2018, **6**, 11724–11733.

216 L. Hui, Y. Xue, D. Jia, Z. Zuo, Y. Li, H. Liu, Y. Zhao and Y. Li, Controlled Synthesis of a Three-Segment Heterostructure for High-Performance Overall Water Splitting, *ACS Appl. Mater. Interfaces*, 2018, **10**, 1771–1780.

217 W. Zhu, M. Ren, N. Hu, W. Zhang, Z. Luo, R. Wang, J. Wang, L. Huang, Y. Suo and J. Wang, Traditional $NiCo_2S_4$ Phase with Porous Nanosheets Array Topology on Carbon Cloth: A Flexible, Versatile and Fabulous Electrocatalyst for Overall Water and Urea Electrolysis, *ACS Sustainable Chem. Eng.*, 2018, **6**, 5011–5020.

218 J. Yu, C. Lv, L. Zhao, L. Zhang, Z. Wang and Q. Liu, Reverse Microemulsion-Assisted Synthesis of $NiCo_2S_4$ Nanoflakes Supported on Nickel Foam for Electrochemical Overall Water Splitting, *Adv. Mater. Interfaces*, 2018, **5**, 701396.

219 Y. Gong, Y. Lin, Z. Yang, J. Wang, H. Pan, Z. Xu and Y. Liu, Crossed $NiCo_2S_4$ Nanowires Supported on Nickel Foam as a Bifunctional Catalyst for Efficient Overall Water Splitting, *ChemistrySelect*, 2019, **4**, 1180–1187.

220 Y. Tang, H. Yang, J. Sun, M. Xia, W. Guo, L. Yu, J. Yan, J. Zheng, L. Chang and F. Gao, Phase-pure pentlandite

$Ni_{4.3}Co_{4.7}S_8$ binary sulfide as an efficient bifunctional electrocatalyst for oxygen evolution and hydrogen evolution, *Nanoscale*, 2018, **10**, 10459–10466.

221 Q. Zhang, C. Ye, X. L. Li, Y. H. Deng, B. X. Tao, W. Xiao, L. J. Li, N. B. Li and H. Q. Luo, Self-Interconnected Porous Networks of NiCo Disulfide as Efficient Bifunctional Electrocatalysts for Overall Water Splitting, *ACS Appl. Mater. Interfaces*, 2018, **10**, 27723–27733.

222 Z. Ma, H. Meng, M. Wang, B. Tang, J. Li and X. Wang, Porous Ni-Mo-S Nanowire Network Film Electrode as a High-Efficiency Bifunctional Electrocatalyst for Overall Water Splitting, *ChemElectroChem*, 2018, **5**, 335–342.

223 K. L. Yan, J. F. Qin, Z. Z. Liu, B. Dong, J. Q. Chi, W. K. Gao, J. H. Lin, Y. M. Chai and C. G. Liu, Organic-inorganic hybrids-directed ternary NiFeMoS anemone-like nanorods with scaly surface supported on nickel foam for efficient overall water splitting, *Chem. Eng. J.*, 2018, **334**, 922–931.

224 H. Fan, J. Huang, G. Chen, W. Chen, R. Zhang, S. Chu, X. Wang, C. Li and K. K. Ostrikov, Hollow Ni-V-Mo Chalcogenide Nanopetals as Bifunctional Electrocatalyst for Overall Water Splitting, *ACS Sustainable Chem. Eng.*, 2019, **7**, 1622–1632.

225 Y. Ning, D. Ma, Y. Shen, F. Wang and X. Zhang, Constructing hierarchical mushroom-like bifunctional NiCo/$NiCo_2S_4$@NiCo/Ni foam electrocatalysts for efficient overall water splitting in alkaline media, *Electrochim. Acta*, 2018, **265**, 19–31.

226 Y. Liu, Q. Li, R. Si, G. D. Li, W. Li, D. P. Liu, D. Wang, L. Sun, Y. Zhang and X. Zou, Coupling Sub-Nanometric Copper Clusters with Quasi-Amorphous Cobalt Sulfide Yields Efficient and Robust Electrocatalysts for Water Splitting Reaction, *Adv. Mater.*, 2017, **29**, 1606200.

227 G. B. Darband, M. Aliofkhazraei, S. Hyun, A. S. Rouhaghdam and S. Shanmugam, Electrodeposition of Ni-Co-Fe mixed sulfide ultrathin nanosheets on Ni nanocones: a low-cost, durable and high performance catalyst for electrochemical water splitting, *Nanoscale*, 2019, **11**, 16621–16634.

228 W. Chen, Y. Zhang, G. Chen, R. Huang, Y. Wu, Y. Zhou, Y. Hu and K. K. Ostrikov, Hierarchical porous bimetal-sulfide bi-functional nanocatalysts for hydrogen production by overall water electrolysis, *J. Colloid Interface Sci.*, 2020, **560**, 426–435.

229 C. Liu, D. Jia, Q. Hao, X. Zheng, Y. Li, C. Tang, H. Liu, J. Zhang and X. Zheng, P-Doped Iron-Nickel Sulfide Nanosheet Arrays for Highly Efficient Overall Water Splitting, *ACS Appl. Mater. Interfaces*, 2019, **11**, 27667–27676.

230 Q. Che, Q. Li, Y. Tan, X. Chen, X. Xu and Y. Chen, One-step controllable synthesis of amorphous (Ni-Fe)S/NiFe(OH) hollow microtube/sphere films as superior bifunctional electrocatalysts for quasi-industrial water splitting at large-current-density, *Appl. Catal. B Environ.*, 2019, **246**, 337–348.

231 F. Wu, X. Guo, G. Hao, Y. Hu and W. Jiang, Self-supported hollow $Co(OH)_2$/NiCo sulfide hybrid nanotube arrays as efficient electrocatalysts for overall water splitting, *J. Solid State Electrochem.*, 2019, **23**, 2627–2637.

232 Y. Hou, M. Qiu, G. Nam, M. G. Kim, T. Zhang, K. Liu, X. Zhuang, J. Cho, C. Yuan and X. Feng, Integrated Hierarchical Cobalt Sulfide/Nickel Selenide Hybrid Nanosheets as an Efficient Three-dimensional Electrode for Electrochemical and Photoelectrochemical Water Splitting, *Nano Lett.*, 2017, **17**, 4202–4209.

233 T. Xiong, G. Li, D. J. Young, Z. Tan, X. H. Yin, Y. Mi and F. Hu, In-situ surface-derivation of Ni-Mo bimetal sulfides nanosheets on Co_3O_4 nanoarrays as an advanced overall water splitting electrocatalyst in alkaline solution, *J. Alloys Compd.*, 2019, **791**, 328–335.

234 F. Li, R. Xu, Y. Li, F. Liang, D. Zhang, W. F. Fu and X. J. Lv, N-doped carbon coated $NiCo_2S_4$ hollow nanotube as bifunctional electrocatalyst for overall water splitting, *Carbon*, 2019, **145**, 521–528.

235 R. Miao, J. He, S. Sahoo, Z. Luo, W. Zhong, S. Y. Chen, C. Guild, T. Jafari, B. Dutta, S. A. Cetegen, M. Wang, S. P. Alpay and S. L. Suib, Reduced Graphene Oxide Supported Nickel-Manganese-Cobalt Spinel Ternary Oxide Nanocomposites and Their Chemically Converted Sulfide Nanocomposites as Efficient Electrocatalysts for Alkaline Water Splitting, *ACS Catal.*, 2017, **7**, 819–832.

236 B. Wu, H. Qian, Z. Nie, Z. Luo, Z. Wu, P. Liu, H. He, J. Wu, S. Chen and F. Zhang, Ni_3S_2 nanorods growing directly on Ni foam for all-solid-state asymmetric supercapacitor and efficient overall water splitting, *J. Energy Chem.*, 2020, **46**, 178–186.

237 T. Zhu, L. Zhu, J. Wang and G. W. Ho, In situ chemical etching of tunable 3D Ni_3S_2 superstructures for bifunctional electrocatalysts for overall water splitting, *J. Mater. Chem. A*, 2016, **4**, 13916–13922.

238 G. Ren, Q. Hao, J. Mao, L. Liang, H. Liu, C. Liu and J. Zhang, Ultrafast fabrication of nickel sulfide film on Ni foam for efficient overall water splitting, *Nanoscale*, 2018, **10**, 17347–17353.

239 H. Ren, Z. H. Huang, Z. Yang, S. Tang, F. Kang and R. Lv, Facile synthesis of free-standing nickel chalcogenide electrodes for overall water splitting, *J. Energy Chem.*, 2017, **26**, 1217–1222.

240 Y. Guo, D. Guo, F. Ye, K. Wang and Z. Shi, Synthesis of lawn-like NiS_2 nanowires on carbon fiber paper as bifunctional electrode for water splitting, *Int. J. Hydrogen Energy*, 2017, **42**, 17038–17048.

241 A. P. Tiwari, Y. Yoon, T. G. Novak, K. S. An and S. Jeon, Continuous Network of Phase-Tuned Nickel Sulfide Nanostructures for Electrocatalytic Water Splitting, *ACS Appl. Nano Mater.*, 2019, **2**, 5061–5070.

242 J. Ding, S. Ji, H. Wang, H. Gai, F. Liu, V. Linkov and R. Wang, Mesoporous nickel-sulfide/nickel/N-doped carbon as HER and OER bifunctional electrocatalyst for water electrolysis, *Int. J. Hydrogen Energy*, 2019, **44**, 2832–2840.

243 L. Zeng, K. Sun, Y. Chen, Z. Liu, Y. Chen, Y. Pan, R. Zhao, Y. Liu and C. Liu, Neutral-pH overall water splitting catalyzed efficiently by a hollow and porous structured

ternary nickel sulfoselenide electrocatalyst, *J. Mater. Chem. A*, 2019, **7**, 16793–16802.

244 J. Jian, L. Yuan, H. Qi, X. Sun, L. Zhang, H. Li, H. Yuan and S. Feng, Sn-Ni_3S_2 Ultrathin Nanosheets as Efficient Bifunctional Water-Splitting Catalysts with a Large Current Density and Low Overpotential, *ACS Appl. Mater. Interfaces*, 2018, **10**, 40568–40576.

245 C. Wu, B. Liu, J. Wang, Y. Su, H. Yan, C. Ng, C. Li and J. Wei, 3D structured Mo-doped Ni_3S_2 nanosheets as efficient dual-electrocatalyst for overall water splitting, *Appl. Surf. Sci.*, 2018, **441**, 1024–1033.

246 Q. Jia, X. Wang, S. Wei, C. Zhou, J. Wang and J. Liu, Porous flower-like Mo-doped NiS heterostructure as highly efficient and robust electrocatalyst for overall water splitting, *Appl. Surf. Sci.*, 2019, **484**, 1052–1060.

247 Y. Gong, Z. Yang, Y. Zhi, Y. Lin, T. Zhou, J. Li, F. Jiao and W. Wang, Controlled synthesis of bifunctional particle-like Mo/Mn-Ni_xS_y/NF electrocatalyst for highly efficient overall water splitting, *Dalton Trans.*, 2019, **48**, 6718–6729.

248 X. Wang, W. Zhang, J. Zhang and Z. Wu, Fe-Doped Ni_3S_2 Nanowires with Surface-Restricted Oxidation Toward High-Current-Density Overall Water Splitting, *ChemElectroChem*, 2019, **6**, 4550–4559.

249 W. Zhu, Z. Yue, W. Zhang, N. Hu, Z. Luo, M. Ren, Z. Xu, Z. Wei, Y. Suo and J. Wang, Wet-chemistry topotactic synthesis of bimetallic iron-nickel sulfide nanoarrays: an advanced and versatile catalyst for energy efficient overall water and urea electrolysis, *J. Mater. Chem. A*, 2018, **6**, 4346–4353.

250 S. Song, Y. Wang, W. Li, P. Tian, S. Zhou, H. Gao, X. Tian and J. Zang, Co-doped Ni_3S_2 hierarchical nanoarrays derived from zeolitic imidazolate frameworks as bifunctional electrocatalysts for highly enhanced overall-water-splitting activity, *J. Alloys Compd.*, 2020, **827**, 154299.

251 J. Guo, K. Zhang, Y. Sun, Q. Liu, L. Tang and X. Zhang, Efficient bifunctional vanadium-doped Ni_3S_2 nanorod array for overall water splitting, *Inorg. Chem. Front.*, 2019, **6**, 443–450.

252 Q. Liu, J. Huang, L. Cao, K. Kajiyoshi, K. Li, Y. Feng, C. Fu, L. Kou and L. Feng, V-Doping Triggered Formation and Structural Evolution of Dendritic Ni_3S_2@NiO Core-Shell Nanoarrays for Accelerating Alkaline Water Splitting, *ACS Sustainable Chem. Eng.*, 2020, **8**, 6222–6233.

253 S. Deng, K. Zhang, D. Xie, Y. Zhang, Y. Zhang, Y. Wang, J. Wu, X. Wang, H. J. Fan, X. Xia and J. Tu, High-Index-Faceted Ni_3S_2 Branch Arrays as Bifunctional Electrocatalysts for Efficient Water Splitting, *Nanomicro Lett.*, 2019, **11**, 12.

254 Q. Lv, L. Yang, W. Wang, S. Lu, T. Wang, L. Cao and B. Dong, One-step construction of core/shell nanoarrays with a holey shell and exposed interfaces for overall water splitting, *J. Mater. Chem. A*, 2019, **7**, 1196–1205.

255 Y. Zhao, B. Jin, A. Vasileff, Y. Jiao and S. Z. Qiao, Interfacial nickel nitride/sulfide as a bifunctional electrode for highly efficient overall water/seawater electrolysis, *J. Mater. Chem. A*, 2019, **7**, 8117–8121.

256 Y. Zhang, J. Fu, H. Zhao, R. Jiang, F. Tian and R. Zhang, Tremella-like Ni_3S_2/MnS with ultrathin nanosheets and abundant oxygen vacancies directly used for high speed overall water splitting, *Appl. Catal. B Environ.*, 2019, **257**, 117899.

257 J. Zhu, M. Sun, S. Liu, X. Liu, K. Hu and L. Wang, Study of active sites on Se-MnS/NiS heterojunctions as highly efficient bifunctional electrocatalysts for overall water splitting, *J. Mater. Chem. A*, 2019, **7**, 26975–26983.

258 S. Qu, J. Huang, J. Yu, G. Chen, W. Hu, M. Yin, R. Zhang, S. Chu and C. Li, Ni_3S_2 Nanosheet Flowers Decorated with CdS Quantum Dots as a Highly Active Electrocatalysis Electrode for Synergistic Water Splitting, *ACS Appl. Mater. Interfaces*, 2017, **9**, 29660–29668.

259 Y. Wu, Y. Liu, G. D. Li, X. Zou, X. Lian, D. Wang, L. Sun, T. Asefa and X. Zou, Efficient electrocatalysis of overall water splitting by ultrasmall $Ni_xCo_{3-x}S_4$ coupled Ni_3S_2 nanosheet arrays, *Nano Energy*, 2017, **35**, 161–170.

260 L. An, J. Feng, Y. Zhang, R. Wang, H. Liu, G. C. Wang, F. Cheng and P. Xi, Epitaxial Heterogeneous Interfaces on N-$NiMoO_4$/NiS_2 Nanowires/Nanosheets to Boost Hydrogen and Oxygen Production for Overall Water Splitting, *Adv. Funct. Mater.*, 2019, **29**, 1805298.

261 M. Zheng, J. Du, B. Hou and C. L. Xu, Few-Layered $Mo_{(1-x)}W_xS_2$ Hollow Nanospheres on Ni_3S_2 Nanorod Heterostructure as Robust Electrocatalysts for Overall Water Splitting, *ACS Appl. Mater. Interfaces*, 2017, **9**, 26066–26076.

262 Z. Ma, Q. Zhao, J. Li, B. Tang, Z. Zhang and X. Wang, Three-dimensional well-mixed/highly-densed NiS-CoS nanorod arrays: an efficient and stable bifunctional electrocatalyst for hydrogen and oxygen evolution reactions, *Electrochim. Acta*, 2018, **260**, 82–91.

263 F. Du, L. Shi, Y. Zhang, T. Li, J. Wang, G. Wen, A. Alsaedi, T. Hayat, Y. Zhou and Z. Zou, Foam-like Co_9S_8/Ni_3S_2 heterostructure nanowire arrays for efficient bifunctional overall water-splitting, *Appl. Catal. B Environ.*, 2019, **253**, 246–252.

264 X. Du, C. Huang and X. Zhang, Surface modification of a Co_9S_8 nanorods with $Ni(OH)_2$ on nickel foam for high water splitting performance, *Int. J. Hydrogen Energy*, 2019, **44**, 19953–19966.

265 S. Shit, S. Chhetri, W. Jang, N. C. Murmu, H. Koo, P. Samanta and T. Kuila, Cobalt Sulfide/Nickel Sulfide Heterostructure Directly Grown on Nickel Foam: An Efficient and Durable Electrocatalyst for Overall Water Splitting Application, *ACS Appl. Mater. Interfaces*, 2018, **10**, 27712–27722.

266 S. Q. Qua, W. Chen, J. S. Yu, G. L. Chen, R. Zhang, S. J. Chu, J. Huang, X. Q. Wang, C. R. Li and K. Ostrikovd, Cross-linked trimetallic nanopetals for electrocatalytic water splitting, *J. Power Sources*, 2018, **390**, 224–230.

267 K. S. Bhat and H. S. Nagaraja, In Situ Synthesis of Copper Sulfide-Nickel Sulfide Arrays on Three-Dimensional Nickel Foam for Overall Water Splitting, *ChemistrySelect*, 2020, **5**, 2455–2464.

268 D. Yang, L. Cao, L. Feng, J. Huang, K. Kajiyoshi, Y. Feng, Q. Liu, W. Li, L. Feng and G. Hai, Formation of hierarchical Ni_3S_2 nanohorn arrays driven by in situ generation of VS_4 nanocrystals for boosting alkaline water splitting, *Appl. Catal. B Environ.*, 2019, **257**, 117911.

269 Y. Q. Gong, Y. Lin, Z. Yang, F. X. Jiao, J. H. Li and W. F. Wang, High-performance bifunctional flower-like Mn-doped $Cu_{7.2}S_4$@NiS_2@NiS/NF catalyst for overall water splitting, *Appl. Surf. Sci.*, 2019, **476**, 840–849.

270 X. Luo, P. Ji, P. Wang, R. Cheng, D. Chen, C. Lin, J. Zhang, J. He, Z. Shi, N. Li, S. Xiao and S. Mu, Interface Engineering of Hierarchical Branched Mo-Doped Ni_3S_2/Ni_xP_y Hollow Heterostructure Nanorods for Efficient Overall Water Splitting, *Adv. Energy Mater.*, 2020, **10**, 1903891.

271 L. Zeng, K. Sun, X. Wang, Y. Liu, Y. Pan, Z. Liu, D. Cao, Y. Song, S. Liu and C. Liu, Three-dimensional-networked Ni_2P/Ni_3S_2 heteronanoflake arrays for highly enhanced electrochemical overall-water-splitting activity, *Nano Energy*, 2018, **51**, 26–36.

272 X. Xiao, D. K. Huang, Y. Q. Fu, M. Wen, X. X. Jiang, X. W. Lv, M. Li, L. Gao, S. S. Liu, M. K. Wang, C. Zhao and Y. Shen, Engineering NiS/Ni_2P Heterostructures for Efficient Electrocatalytic Water Splitting, *ACS Appl. Mater. Interfaces*, 2018, **10**, 4689–4696.

273 X. W. Zhong, J. Tang, J. W. Wang, M. M. Shao, J. W. Chai, S. P. Wang, M. Yang, Y. Yang, N. Wang, S. J. Wang, B. M. Xu and H. Pan, 3D heterostructured pure and N-Doped Ni_3S_2/VS_2 nanosheets for high efficient overall water splitting, *Electrochim. Acta*, 2018, **269**, 55–61.

274 X. Q. Du, Z. Yang, Y. Li, Y. Q. Gong and M. Zhao, Controlled synthesis of $Ni(OH)_2/Ni_3S_2$ hybrid nanosheet arrays as highly active and stable electrocatalysts for water splitting, *J. Mater. Chem. A*, 2018, **6**, 6938–6946.

275 Q. Xu, W. Gao, M. Wang, G. Yuan, X. Ren, R. Zhao, S. Zhao and Q. Wang, Electrodeposition of NiS/Ni_2P nanoparticles embedded in amorphous $Ni(OH)_2$ nanosheets as an efficient and durable dual-functional electrocatalyst for overall water splitting, *Int. J. Hydrogen Energy*, 2020, **45**, 2546–2556.

276 L. M. Ren, C. Wang, W. Li, R. H. Dong, H. X. Sun, N. Liu and B. Y. Geng, Heterostructural NiFe-LDH@Ni_3S_2 nanosheet arrays as an efficient electrocatalyst for overall water splitting, *Electrochim. Acta*, 2019, **318**, 42–50.

277 C. Hu, L. Zhang, Z. J. Zhao, A. Li, X. Chang and J. Gong, Synergism of Geometric Construction and Electronic Regulation: 3D Se-$(NiCo)S_x/(OH)_x$ Nanosheets for Highly Efficient Overall Water Splitting, *Adv. Mater.*, 2018, **30**, 1705538.

278 B. Ma, X. Guo, X. Zhang, Y. Chen, X. Fan, Y. Li, F. Zhang, G. Zhang and W. Peng, Intercalated Graphite between Ni Foam and Ni_3S_2 Nanocrystals for the Activity Promotion in Overall Water Splitting, *Energy Technol.*, 2019, **7**, 1900063.

279 H. C. Tsai, B. Vedhanarayanan and T. W. Lin, Freestanding and Hierarchically Structured Au-Dendrites/3D-Graphene Scaffold Supports Highly Active and Stable Ni_3S_2 Electrocatalyst toward Overall Water Splitting, *ACS Appl. Energy Mater.*, 2019, **2**, 3708–3716.